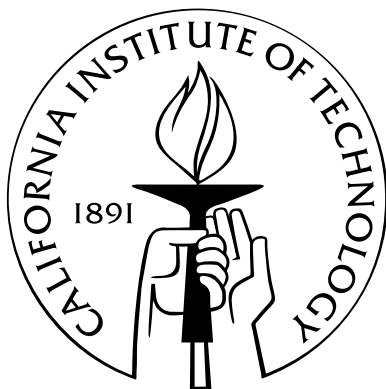# Algorithms for Reaction Mechanism Reduction and Numerical Simulation of Detonations Initiated by Projectiles

Thesis by

Patrick Hung

In Partial Fulfillment of the Requirements

for the Degree of

Doctor of Philosophy

California Institute of Technology

Pasadena, California

2003

(Submitted 5 May 2003)

To Ruth

Acknowledgements

I am indebted to many for playing a role in my graduate career. Some helped me get started, some helped me finish, and many helped me along the way; Michael Aivazis, Marco Arienti, Tony Chao, Chris Eckett, Dan Meiron, Bjarne Bergheim[*], Steve Bresanello, Gustavo Joseph[†], Cinyoung Lee, Guillaume Lessard, Al Preston, Prashant Purohit[‡], Michel Tanguay[§] and Dan Zimmerman[¶] are but a few among them.

I would like to thank my parents, my brother and Flora for their love, trust, patience and support. Finally, I am extremely grateful to my advisor, Joseph Shepherd, for everything. Thank you, it has truly been a privilege.

---

[*]Bjarne artfully combines pleasant road manners and skiing expertise by treating carpool lanes as slalom courses.

[†]Gustavo knows where his towel is, with one particularly disastrous exception. His "I wouldn't go that far" comeback during candidacy exams is worthy of the archives.

[‡]Prashant is known for his projectile incident (1998), his quickness in stating the obvious (1975 – present) and his intention to be married within 2 years (1997 – present).

[§]Michel, thanks for the drinks, the poutine, and the correlation.

[¶]Dan, thanks for TV and E3.

Abstract

The evolution of a homogeneous, chemically reactive system with n_s species forms a dynamical system in chemical state-space. Under suitable constraints, unique and stable equilibrium exists and can be interpreted as zeroth-dimensional (point like) attractors in this n_s-dimensional space. At these equilibrium compositions, the rates of all reversible reactions vanish and can, in fact, be determined from thermodynamics independent of chemical kinetics.

Generalizing this concept, an m-dimensional Intrinsic Low Dimensional Manifold (ILDM) represents an m-dimensional subspace in chemical state-space where all but the m-slowest *aggregate* reactions are in equilibrium, and these aggregate reactions are determined by eigenvalue considerations of the chemical kinetics. In this context, a certain composition is said to be m-dimensional if it is on an m-, but not an $(m-1)$-, dimensional ILDM.

Two new algorithms are proposed that allow the dimensionality of chemical compositions be determined simply. The first method is based on recasting the Maas and Pope algorithm. The second, and more efficient, method is inspired by the mathematical structure of the Maas and Pope algorithm and makes use of the technique known as *arc-length reparameterization*. In addition, a new algorithm for the construction of ILDM, and the application of these ideas to detonation simulations, is discussed.

In the second part of the thesis, numerical simulations of detonation waves initiated by hypervelocity projectiles are presented. Using detailed kinetics, only the shock-induced combustion regime is realized as simulating the conditions required for a stabilized detonation is beyond the reach of our current computational resources. Resorting to a one-step irreversible reaction model, the transition from shock-induced combustion to stabilized oblique detonation is observed, and an analysis of this transition based on the critical decay-rate model of Kaneshige (1999) is presented.

Contents

List of Figures

List of Tables

Nomenclature

Latin characters

A	projector taking J to $\mathsf{J}^{\star}$ [see eq. (4.30)]	
$\mathsf{A_k}$	matrix used for in constructing the Grammian. [see eq. (3.18)]	
$\boldsymbol{c}$	vector of molar concentrations	$\mathrm{mol/m^3}$
c_p	mixture-averaged specific heat at constant pressure	$\mathrm{J/kg \cdot K}$
c_v	mixture-averaged specific heat at constant volume	$\mathrm{J/kg \cdot K}$
D	normal shock or detonation velocity	$\mathrm{m/s}$
E_a	activation energy for the one-step model	
e	specific internal energy	$\mathrm{J/kg}$
$\boldsymbol{f}$	the right-hand-side of a system of ODE	
f	the overdrive factor [see eq. (6.4)]	
f_i	components of $\boldsymbol{f}$	
$\boldsymbol{g}$	normalized (unit-norm) form of $\boldsymbol{f}$	
$\boldsymbol{g}^{\flat}$	$\boldsymbol{g}$ projected onto the element-conserved subspace	
I	the identity matrix	
J	Jacobian matrix	

[†]SI units are listed here, although CGS units are often used in the text.

$\mathsf{J}^\flat$	Jacobian in element-conserved subspace [see eq. (3.8)]	
$\mathsf{J}^\star$	arc-length normalized Jacobian	
K	equilibrium constant	(varies)
k_{f_i}	forward rate constant of reaction i [see eq. (1.4)]	(varies)
k_{r_i}	reverse rate constant of reaction i	(varies)
$\mathcal{M}^k$	a k-dimensional ILDM [see eq. (3.5)]	
M	$n_e \times n_s$ matrix with coefficients μ_{ij}	
$M_{m,n}$	matrix with m rows and n columns	
M_n	square $n \times n$ matrix	
n_e	the number of elements in a reaction mechanism	
n_r	the number of reactions in a reaction mechanism	
n_s	the number of species in a reaction mechanism	
P	pressure	Pa
q	heat of reaction for the one-step model	
q_i	progress rate for reaction i [see eq. (1.5)]	mol/m^3·s
$\mathbf{R}$	the real numbers	
$\mathbf{R}^n$	an n-dimensional space over $\mathbf{R}$	
R_p	projectile radius	
$\mathcal{R}$	universal gas constant	J/mol·K
s	specific entropy	J/kg·K
T	temperature	K
t_k	time of arrival to $\mathcal{M}^k$ [see eq. (3.25)]	

T_{vN} temperature at the von Neumann point

u_i velocity components in Cartesian coordinates   m/s

u_{CJ} CJ detonation velocity   m/s

u_{ZND} steady ZND detonation velocity   m/s

V matrix of right-eigenvectors

V^{-1} matrix of left-eigenvectors

$\mathcal{W}$ mixture-averaged (mean) molecular weight   kg/mol

$\mathcal{W}_i$ molecular weight of species i kg/mol

$\boldsymbol{x}$ vector of mole fractions

$\boldsymbol{y}$ vector of mass fractions

Greek characters

γ ratio of specific heats

Γ^k Grammian [see eq. (3.17)]

$\Delta_{1/2}$ half-reaction zone length

Λ diagonal matrix of eigenvalues [see eq. (3.1)]

λ_d detonation cell width

μ_{ij} coefficients of M, the number of the i-th element in species j

ν'_{ki} forward stoichiometric coefficient for species k
    in reaction i [see eq. (1.3)]

ν''_{ki} backward stoichiometric coefficient for species k
    in reaction i [see eq. (1.3)]

ρ density   kg/m^3

$\sigma(\mathsf{J})$ the set of eigenvalues for (spectrum of) J

σ_f	the set of fast eigenvalues [see eq. (3.3)]	
σ_s	the set of slow eigenvalues [see eq. (3.3)]	
τ	induction time (from Frank-Kamenetskii's model)	
ϕ	vector of specific mole numbers	mol/kg
$\dot{\omega}_k$	net molar production rate of species k [see eq. (1.6)]	mol/m^3·s

Acronyms

AMR	adaptive mesh refinement
ASCI	accelerated strategic computing initiative
CFD	computational fluid dynamics
CFL	Courant-Friedrichs-Lewy
CJ	Chapman–Jouguet
CSP	computational singular-value perturbation
CV	constant volume
DAE	differential-algebraic equations
GEL	ghost-fluid Eulerian Lagrangian
HE	high explosives
IC	initial condition
ILDM	intrinsic low dimensional manifold
ISAT	in-situ adaptive tabulation
ODE	ordinary differential equations
QSSA	quasi steady state approximation
SVD	singular value decompositions

vN   von Neumann

VTF   virtual test facility

ZND   Zel'dovich-von Neumann-Doering

Operators

$[\cdot]$ molar concentrations   mol/m^3

$\langle \cdot, \cdot \rangle$ inner product

$\mathcal{L}_S$ reaction source operator [see eq. (2.6)]

$\mathcal{L}_{F_x}$ convective operator in x [see eq. (2.6)]

$\mathcal{L}_{F_y}$ convective operator in y [see eq. (2.6)]

Subscripts

o   free-stream value

vN   evaluated at the von Neumann point

Superscripts

-1 inverse

*   post-shock value

T   matrix or vector transpose

Accents

$\cdot$ time derivative

Chapter 1

Introduction

1.1 Overview

The Department of Energy's Accelerated Strategic Computing Initiative (ASCI) made available to the researchers of five ASCI Centers[*] an immense amount of computational power through the use of *commodity clusters*. These machines (LANL's ASCI Blue-Mountain, LLNL's ASCI Blue-Pacific, Sandia's ASCI Red) provide on average over a thousand times the raw performance of any contemporary desktop. The goal of the Caltech center is to explore the issues in software development through a virtual test facility (VTF) for simulating the response of solid materials to detonation loading by explosives. Summaries of the goals and accomplishments can be found in the ASCI annual reports, the most recent of which is Aivazis et al. (2001).

The focus of the High Explosives group is on the development of computational tools to simulate phenomena relevant to reactive flows and detonation experiments. Examples of research on explosive and material properties include studies on the Mie-Grüneisen equation of state molecular dynamics described in Arienti et al. (1999) and Cohen et al. (1999) and reaction mechanisms for HMX (see Chakroborty et al., 2001) and RDX (see Chakroborty et al., 2000). The application of detailed reaction mechanisms to computational fluid dynamics (CFD) calculations has motivated the development of advanced techniques in mechanism reduction for detonation first studied by Eckett (2001). These ideas are further developed in this thesis.

The simulation of high explosives (HE) detonation experiments requires an interaction of

---

[*]University of Chicago, University of Illinois at Urbana/Champaign, Stanford University, University of Utah, and California Institute of Technology
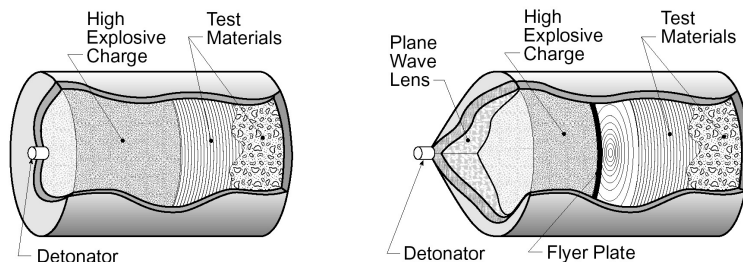
Figure 1.1: Illustrations of the proposed capability of the VTF. Simulations of these high-explosives-driven shock tubes motivate advances in many fields of scientific research.

detonating flows with deformable boundaries. For example, many applications of energetic materials involve accelerating metals with large deformations. In order to treat the detonation using standard Eulerian methods and the material deformation with Lagrangian techniques, Fedkiw and Aslam's ideas (see Fedkiw et al., 1999) were developed into the Ghost-fluid Eulerian-Lagrangian (GEL) coupling algorithm (Arienti, 2003). Applications of these numerical methods include the corner-turning (detonation diffraction) experiment performed by Schultz (2000), with detailed simulations performed and documented in Arienti (2003), and experiments in detonation initiation by projectiles of Kaneshige (1999), with the numerical simulations described in this thesis.

The complementary development of the computational infrastructure (led by Aivazis), driven by the Python[†] scripting language, provides the keystone for the Caltech ASCI project and greatly facilitates the coexistence and coupling of independently designed and disparate software packages.

An illustration of the proposed *overarching application* for the Virtual Test Facility, taken from (Meiron, 1999), is shown in Figure 1.1. Detailed simulation of high-explosives-driven shock tubes necessitates and motivates scientific research in many areas: initiation and detonation of the HE charge; modeling of compressible turbulence and mixing; and the dynamic response of the target material which may ultimately fracture. For us, the motivation comes from our inability, despite the power provided by ASCI class supercomputers, to incorporate detailed reaction mechanisms of even simple hydrocarbon fuels for fully resolved two and three dimensional simulations of detonations.

[†]`http://www.python.org`

1.2 Computational cost of detailed reaction kinetics

The basic problem can be summarized as follows. Consider the third reaction of the well documented GRIMech-3.0 (Smith et al., 2003) mechanism. The reaction is

$$O + H_2 \rightleftharpoons H + OH \ . \tag{1.1}$$

The rate of change of the concentration of O, denoted by [O], can be written as

$$\frac{d[O]}{dt} = k_f[O][H_2] - k_r[H][OH] \ , \tag{1.2}$$

where k_f and k_r are the forward and reverse rate coefficients. The forward rate for the above reaction is

$$k_f = 38700 \ T^{2.7} \exp\left(-6260/\mathcal{R}T\right) \ ,$$

where k_f has units mol/cm^3, T is the temperature and $\mathcal{R}$ is the universal gas constant in units of cal/mol·K. The reverse rate $k_r = K/k_f$ is derived from the equilibrium constant K obtained from the Gibbs free energy of the species involved. The contribution of reaction (1.1) to the production rate of O is given by (1.2). The net rate of change of [O] is obtained by summing the contributions from all the reactions involving the species O, of which the reaction described is just one.

In general, for a given detailed reaction mechanism, the i-th chemical reaction, involving K participating species, can be written in the form

$$\sum_{k=1}^{K} \nu'_{ki}\chi_k \rightleftharpoons \sum_{k=1}^{K} \nu''_{ki}\chi_k \ , \tag{1.3}$$

where the ν_{ki} are the stoichiometric coefficients of species k in the i-th reaction. The (forward) rate coefficients for the i-th reaction are assumed to take on the Arrhenius form, for the i-th reaction,

$$k_{f_i} = A_i T^{\beta_i} \exp\left(\frac{-E_i}{RT}\right) \ , \tag{1.4}$$

with the reverse rate coefficients k_{r_i} computed using the equilibrium constants K_i. The

progress rate for such a reaction has the general form

$$q_i = k_{f_i} \prod_{k=1}^{K} [X_k]^{\nu'_{ki}} - k_{r_i} \prod_{k=1}^{K} [X_k]^{\nu''_{ki}} \; , \tag{1.5}$$

where $[X_k]$ is the molar concentration of species k. The production rate of species k is then assembled from the progress rates q_i for all reactions involving that species,

$$\dot{\omega}_k = \sum_{i=1}^{I} \nu_{ki} q_i \; , \tag{1.6}$$

where $\nu_{ki} = \nu''_{ki} - \nu'_{ki}$. See Williams (1985) for an in depth discussion on the theory of chemical kinetics, and Kee et al. (1987) for details on the CHEMKIN mechanism format, the *de facto* standard of the combustion community.

In each chemistry substep of an operator-split solution to the reactive Euler equations, a set of Ordinary Differential Equations (ODE), representing the evolution of the composition of a constant volume combustion process, needs to be numerically integrated. Let the composition of the system involving n_s species be represented by the n_s-dimensional vector

$$\boldsymbol{z} = [z_1, z_2, \ldots, z_{n_s}] \in \mathbf{R}^{n_s} \; , \tag{1.7}$$

where the components $z_1, \ldots, z_{n_s}$ are some representation of the *amount* of each of the involved species present. The governing equation that describes the evolution of the composition $\boldsymbol{z}$ can be written in the form

$$\frac{d}{dt} \begin{pmatrix} z_1 \\ z_2 \\ \vdots \\ z_{n_s} \end{pmatrix} = \begin{pmatrix} f_1(z_1, z_2, \ldots, z_{n_s}) \\ f_2(z_1, z_2, \ldots, z_{n_s}) \\ \vdots \\ f_{n_s}(z_1, z_2, \ldots, z_{n_s}) \end{pmatrix} \quad \text{or} \quad \dot{\boldsymbol{z}} = \boldsymbol{f}(\boldsymbol{z}) \; , \tag{1.8}$$

where $\boldsymbol{f}$ is related[‡] to the production rate $\dot{\omega}$ of the species involved. The *computational cost*[§] of evaluating $\boldsymbol{f}$ is roughly proportional to the number of reactions n_r. Because the

---

[‡]It is the production rate $\dot{\omega}$ if the components of $\boldsymbol{z}$ are species concentration. However, other representations such as species mass-fractions are typically used.

[§]*Computational cost* is usually measured in terms of the number of floating-point operations (flop). Practically, the amount of wall-clock time is another good indication. The word *computational* will be omitted when the context is clear.

Reaction Mechanism	Species	Reactions
Maas-Warnatz (H_2–O_2) (Maas and Warnatz, 1988)	9	37
Hydrogen-Oxygen (Miller and Bowman, 1989)	12	24
Nitrogen-Chemistry (Miller and Bowman, 1989)	20	73
GRIMech-3.0 (Smith et al., 2003)	53	325
HMX/RDX (Chakroborty et al., 1999)	89	457

Table 1.1: Detailed reaction mechanisms used in this thesis.

Reaction Mechanism	CFD	Chemistry
Hydrogen-Oxygen:	0.3 ms	1.2 ms
GRIMech-3.0:	1.0 ms	35 ms

Table 1.2: Computational cost (time per cell per timestep) comparison on a 750 MHz Intel Pentium III processor.

ODE is stiff (see Hairer (1996) for an introduction), an implicit solver is required.

The cost of the implicit solver scales as $n_s{}^3$, as it requires the solution of a system of linear equations. On the other hand, the computation of the Jacobian matrix needed for the implicit solver requires n_s evaluations of $\boldsymbol{f}$ using finite-difference, so the cost scales to $n_s \times n_r$. Thus, the cost of detailed chemistry scales between the product of the number of species and the number of reactions, and the cube of the number of species, per control volume. A summary of the sizes of four reaction mechanisms is shown in Table 1.1. The simplest of the mechanisms (Hydrogen-Oxygen) is a subset of the mechanism labeled "Nitrogen Chemistry", from Miller and Bowman (1989).

The cost of the Euler (nonreactive flux) substep is compared to the cost of chemistry in Table 1.2. The terminology used below will be clarified later in the text. For a domain that is 100 times the size of the nominal (Chapman-Jouguet) induction zone, 10 cells per induction-zone length require a 1000^3 domain in three-dimensions. Assuming a CFL number of 0.3, at least 2000 steps are required to propagate the detonation across the domain (in the case of a detonation-frame calculation, many more are usually desired depending on the application). Using the simplest of the reaction mechanisms requires 95 CPU-years. With ASCI class computers, assuming a realistic thousand-fold increase in performance, such a simulation will take a month to complete. This time balloons to over 3 years for the GRIMech-3.0 mechanism.

It gets worse. For sensitive mixtures such as the N_2 diluted stoichiometric H_2–N_2O mixture described in Shepherd et al. (2002), small perturbations of the leading shock strength

(and hence the post-shock temperature) can dramatically alter the reaction rate. Resolving such detonations absolutely requires the use of Adaptive Mesh Refinement, and scalable distributed AMR is still very much an active area of research. It is for this reason that strongly unstable mixture conditions are avoided in this work. The problem is difficult enough as it stands.

1.3   Background for mechanism reduction

Computational fluid dynamics simulations of compressible gas dynamical systems are computationally expensive. With the addition of chemistry, such as in the modeling of detonation waves in gaseous explosives, the current state of the art in computational power is still incapable of simulating detonation experiments using the reactive Euler equations in three dimensions for even simple (nitrous oxide and air detonation) reaction networks.

While chemists and material scientists strive to obtain ever more accurate (and elaborate) descriptions of such chemical reaction networks, engineers and numerical analysts face a different challenge: to reduce such detailed knowledge by throwing away the comparatively negligible in order to make computations practical with the technology available today.

The goal for mechanism reduction is, simply speaking, to accelerate the integration of the ODE (1.8) governing the evolution of the species composition in a chemically reactive system. Widely disparate progress rates q_i makes the ODE extremely stiff. A few methods for attaining such speed-up are:

1. Reducing the size of the system n_s.

2. Increasing the speed at which the right-hand-side $\boldsymbol{f}$ is computed.

3. Using non-implicit solvers.

The first strategy is the most popular and has many variants. It is also one of the most effective, since the cost of the implicit solver scales as $n_s{}^m$ where $2 \leq m \leq 3$ (assuming that the amount of random-access memory is sufficient). For example, elemental constraints mean that the amount of the n_s-species cannot vary independently, limiting the accessible chemical state-space to an $(n_s - n_e)$-dimensional submanifold (see §2.2.2). In addition, the classic technique of Quasi-Steady-State-Approximations (QSSA) recognizes that additional

constraints exist due to quasi-steady-state (where the production rate of a subset of species is zero) and quasi-equilibrium (where the forward and reverse rates of a subset of reactions are in balance). An overview of this technique can be found in Warnatz et al. (1999), and it is applied to detonation simulations in Eckett (2001).

Application of the QSSA technique depends on *chemist's intuition*. Each (independent) algebraic constraint identified will lower the dimensionality of the system by one. The resulting "reduced mechanism" will then be a system of differential-algebraic equations (DAE), and practical reduction is not possible until the algebraic constraints are solved. These constraints are equivalent to limiting the system's behavior to low-dimensional subspaces. To illustrate, suppose that the j-th species is in quasi-steady-state. Then from (1.6),

$$\dot{\omega}_j = \sum_{i=1}^{I} \nu_{ji} q_i = 0 \ . \tag{1.9}$$

Because the progress rates q_i in (1.9) involve products of species concentration (see (1.5)), the quasi-steady-state approximation leads to complicated nonlinear algebraic constraints of the form

$$f_j(\boldsymbol{z}) = 0 \ . \tag{1.10}$$

Similarly, assuming the l-th reaction is in partial-equilibrium, from (1.5) we get a similar nonlinear algebraic constraint,

$$q_l(\boldsymbol{z}) = 0 \ . \tag{1.11}$$

Assuming that a total of $(n_s - m)$ quasi-steady-state and partial-equilibrium constraints are identified, we get the following algebraic system:

$$
\begin{aligned}
g_{m+1}(z_1, z_2, \ldots, z_{n_s}) &= 0 \\
g_{m+2}(z_1, z_2, \ldots, z_{n_s}) &= 0 \\
&\vdots \\
g_{n_s}(z_1, z_2, \ldots, z_{n_s}) &= 0
\end{aligned}
\tag{1.12}
$$

(1.12) is a system of $(n_s - m)$ equations with n_s unknowns. Assuming that the constraints are independent, the solution of the algebraic system will be an m-dimensional surface in $\mathbf{R}^{n_s}$. To illustrate, we will assume that the surface can be parameterized by $(z_1, z_2, \ldots, z_m)$

as follows:

$$z_{m+1} = h_{m+1}(z_1, z_2, \ldots, z_m)$$

$$z_{m+2} = h_{m+2}(z_1, z_2, \ldots, z_m)$$

$$\vdots$$

$$z_{n_s} = h_{n_s}(z_1, z_2, \ldots, z_m)$$

(1.13)

Using (1.12), (1.8) can be written as the following set of DAE:

$$
\begin{pmatrix}
\dot{x}_1 \\
\vdots \\
\dot{x}_m \\
0 \\
\vdots \\
0
\end{pmatrix}
=
\begin{pmatrix}
f_1(z_1, z_2, \ldots, z_{n_s}) \\
\vdots \\
f_m(z_1, z_2, \ldots, z_{n_s}) \\
g_{m+1}(z_1, z_2, \ldots, z_{n_s}) \\
\vdots \\
g_{n_s}(z_1, z_2, \ldots, z_{n_s})
\end{pmatrix}
$$

(1.14)

Solving (1.14) is generally not practical, as it takes a lot of effort to obtain the algebraic constraints g and their solution is no easier than that of the differential equations they replaced. Assuming that the low-dimensional surface can be obtained, substituting (1.13) into (1.8) leads to true reduction. The original n_s-dimensional system is reduced to the m-dimensional system

$$\dot{x}_1 = f_1(z_1, \ldots, z_m, h_{m+1}, \ldots, h_{n_s})$$

$$\dot{x}_2 = f_2(z_1, \ldots, z_m, h_{m+1}, \ldots, h_{n_s})$$

$$\vdots$$

$$\dot{x}_m = f_m(z_1, \ldots, z_m, h_{m+1}, \ldots, h_{n_s}) \ .$$

(1.15)

While (1.15) accomplishes the goal of dimension reduction, attaining exactly this form is not possible because the constraints in (1.12) cannot be analytically inverted to find (1.13). While solving (1.12) numerically is possible, and the resulting lower-dimensional surface will be a tabulation instead of an analytical expression, this approach has never been taken. One reason is that the algebraic constraints are only approximate, and are applicable in a very limited range of compositions. It is for this reason that QSSA has fallen out of favor in recent years compared to techniques like the Intrinsic Low Dimensional Manifolds
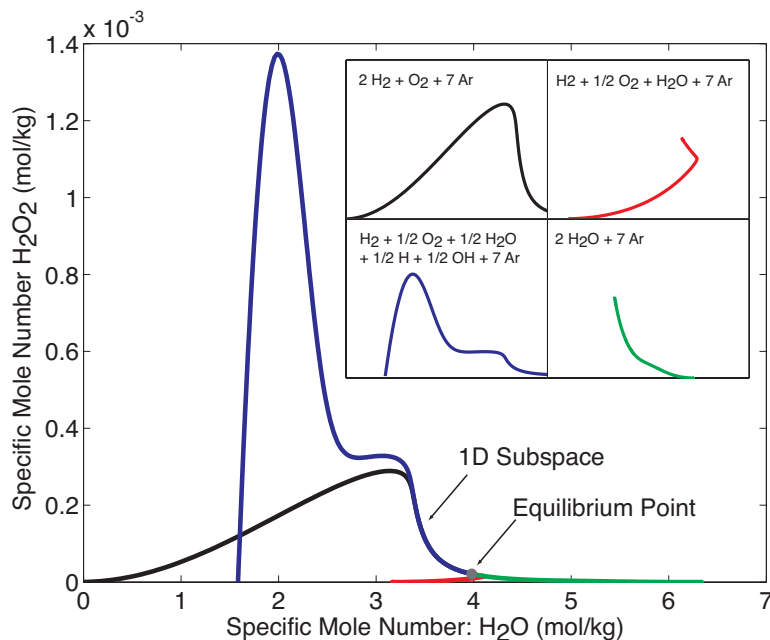
Figure 1.2: Illustration of the ILDM method.

(ILDMs) of Maas and Pope (1992b), which *systematically* and *automatically* identify these lower-dimensional constraints.

The ILDM technique analytically defines a reduced manifold based on eigenvalue considerations, and the resulting manifold is typically computed *a priori* and stored as a lookup table. For a given closed chemically reactive system, the thermodynamic equilibrium is a zeroth-dimensional attractor to which all trajectories starting from different (but consistent) initial conditions are ultimately attracted. The ILDM method extends this idea based on the observation that there are higher-dimensional attractors, arising not only from thermodynamic but also from chemical kinetics, that attract these trajectories. In Figure 1.2, adiabatic constant-volume trajectories from four different initial conditions having the same atomic mole numbers, internal energies and densities (see Table 5.1) are plotted. It can be seen from the figure that there is a one-dimensional subspace (line) onto which the four trajectories coalesce before finally reaching the equilibrium position.

Unlike reduction techniques such as one-step or multistep reaction models, whose goals are to match the detailed mechanism in terms of detonation velocities and detonation cell sizes, or combustion modeling techniques yielding reduced mechanisms whose figure-of-merit is based on correctly predicting a number of valuable quantities such as flame temperature

and exhaust emissions, the driving force behind ILDM reduction is different. By limiting the dynamics to lower-dimensional subspaces, the initial transient is lost. However, when conditions are appropriate, the composition of all species will be available and theoretically close to the original reaction mechanism from which ILDM is applied.

A lot of recent work has concentrated on improving the efficiency (Maas, 1998, Nafe and Maas, 2002) and storage (Blasenbrey et al., 1999, Niemann et al., 1997) of the ILDM computation. Theoretical justifications of the method based on asymptotic analyses can be found in Rhodes et al. (1999) and Kaper and Kaper (2002). It should be noted that if the word *manifold* appears intimidating, the word *subspace* or even *surface* can be substituted. The usage of the word *manifold* comes from the fact that when a function of m equations with n unknowns can be "inverted", with $m < n$, its *preimage* is a manifold of dimensions $(n - m)$ (see Guillemin and Pollack, 1974). By virtue of being a manifold, this preimage is theoretically *nice* and *parameterizable*. Of course, without knowing anything about this function except that it originates from chemical kinetics, nothing can be said *a priori* of its smoothness, connectivity, or parameterization.

The method of computational singular-value perturbation (CSP), like ILDM, also seeks to reduce the dimensionality through analyses of local eigenvalues (Lam, 1993). The CSP method identifies computational basis vectors and classifies them into exhausted modes, active modes, and dormant modes. In other words, it systematically mimics the actual reaction pathway of the detailed reaction mechanism. For example, during the main heat-release stage of the combustion of hydrocarbons, reactions involving CO_2 are active, the initial radical pool is exhausted, and reactions related to NOx productions are still dormant. An overview can be found in Lam (1993).

As mentioned above, an alternative to speeding up the ODE integration is to make the calculation of f more efficient. Cantera, by Goodwin (2003), is a C++-based software package that obtains significant speedup over the CHEMKIN Fortran subroutine library through caching of thermodynamic properties. *Fuego*, by Michael Aivazis, converts reaction mechanisms into optimized, inlined C functions, increasing efficiency by minimizing conditional statements, parameter passing, temporary storage, and variable dereferencing.

Alternatively, non-implicit solvers can be used if stability can be maintained. Mason et al. (2002), for example, describes the usage of an explicit solver, in conjunction with error control techniques, for computations with moderately stiff chemistry. Another strategy is

to replace the integration of the ODE with a functional mapping. In the "in situ adaptive tabulation" (ISAT) technique of Pope (1997), the integration of the composition $\boldsymbol{z}$ from time t to $t + \Delta t$ is viewed as a time-advance mapping. In this sense, the ODE is replaced by an *input-output* system that takes $\boldsymbol{z}(t)$ as input and outputs $\boldsymbol{z}(t + \Delta t)$. In the case of ISAT, the mapping comes from a table obtained by solving the full (or reduced) kinetics system. Another way to obtain this mapping is through the use of a suitable polynomial *surrogate* obtained from the detailed reaction mechanism (Bell et al., 2000).

Much work has been done in applying the ILDM technique to combustion systems. The research presented in this thesis expands and elaborates on the work of Eckett (2001), who was among the first to apply the method to numerical simulations of gaseous detonations. The only other group currently active in the same area is led by Joseph Powers at Notre Dame (Singh et al., 2001b, Singh and Powers, 1999, Paolucci et al., 2000). Eckett (2001) made the following conclusions:

1. While QSSA was shown to be a viable technique in reducing the H_2–O_2–diluent mechanism of Maas and Warnatz (1988) (9 species, 19 reversible reactions) into a three-step reduced model, significant quantitative errors (in terms of the ZND induction lengths and unsteady shock pressure history) resulted. Additionally, implementation complexities limit its applicability to all but very small detailed reaction systems.

2. A new two-stage methodology was presented whereby an *induction manifold* was used to capture the early transients prior to the slow dynamics on the ILDM. Alternatively, the full reaction mechanism can be employed in regions where ILDMs are not applicable. This approach is investigated by Singh et al. (2001b).

3. It was shown that the above two-stage technique with a two-dimensional ILDM produced much better quantitative agreements than the QSSA reduced model for the same H_2–O_2–diluent system for one-dimensional unsteady simulations.

4. A two-dimensional cellular detonation of stoichiometric hydrogen-oxygen in 70% argon dilution ($2H_2 + O_2 + 7Ar$) with the above technique (and also with a two-dimensional ILDM) reproduced the results of Oran et al. (1998) qualitatively.

(a) Shock-induced combustion

(b) Stabilized detonation
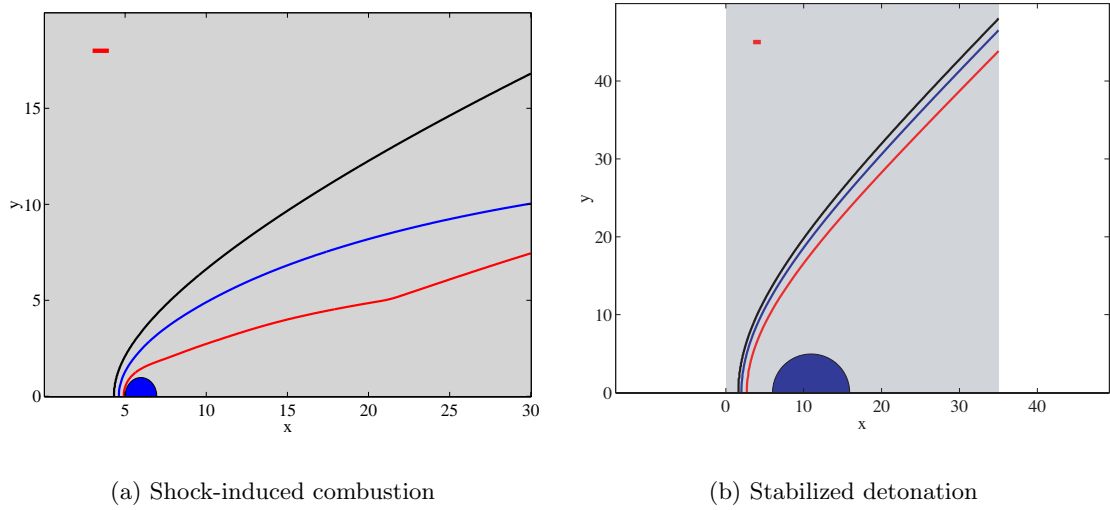
Figure 1.3: Illustrations of steady, reactive flows over projectiles. The two contour lines behind the leading shock are the 50% and 90% reaction locus. (a) is an example of reactive, but non-detonating flow, as can be seen by the decoupled reaction zone from the leading shock. (b) exhibits successful detonation initiation.

1.4 Background for detonation initiation by hypersonic projectiles

When a projectile is shot into a tube filled with a detonable mixture, many different steady and unsteady flow configurations are possible, depending on the speed of the projectile, mixture conditions, wall (confinement) effects, and projectile shapes. Many experiments have been done and a detailed review can be found in Kaneshige (1999).

When the speed of the projectile exceeds the Chapman-Jouguet (CJ) speed, an oblique-stabilized detonation configuration becomes *possible*. There are two contrasting steady-flow regimes: *supersonic shock-induced combustion* and *stabilized detonation*. For shock-induced combustion, an uncoupled reaction zone follows the leading bow shock. The reaction occurs near the nose due to shock heating, and gradually quenches away from the stagnation streamline as the shock decays to the Mach angle. This is shown in Figure 1.3(a).

When conditions are suitable, the reaction zone can become coupled to the leading shock, resulting in an oblique detonation that stabilizes in front of the projectile obliquely at the CJ angle (Figure 1.3(b)). An analysis of this transition from shock-induced combustion to detonation initiation will be presented.

Experiments involving spherical projectiles with observed stabilized detonations have been performed by the group at Nagoya University led by Fujiwara, and in the recent

work done at Caltech by Kaneshige (1999). More recent work includes investigation on the oblique detonation structure around projectiles with wedge-shaped fronts using H_2–O_2 and H_2–air mixtures (Kasahara et al., 2001), and around spherical projectiles using H_2–O_2–Ar and C_2H_2–O_2–air mixtures (Kasahara et al., 2001). One of their observations is that, for projectiles traveling at super-CJ speeds, there is a critical initial pressure for the mixture above which detonation initiation will occur. In Kasahara et al. (2002), the authors argued for the use of a "mean-curvature coefficient," a ratio between detonation cell width and shock curvatures, as the critical initiation criterion.

On the computational front, wedge-induced detonations have been studied by various authors, including Matsuo and Fujiwara (1993), Grismer and Powers (1996) and, more recently, Papalexandris (2000). The recent work by Ju and Sasoh (1997) numerically studies detonation initiation for flows over supersonic spheres using detailed chemistry, though they did not obtain a stabilized oblique detonation wave in that work.

1.5 Presentation outline

In Chapter 2, the numerical methods employed for the simulation of gaseous detonations are presented, and particular attention is focused on the linear-algebraic structure of the adiabatic constant-volume combustor.

In Chapter 3, the Intrinsic Low Dimensional Manifold algorithm of Maas and Pope (1992b) is presented. It will be shown that when the equation defining the ILDM is re-cast, an "embarrassingly parallel" form of the Maas and Pope algorithm becomes possible. Illustration of the technique is given in Chapter 5. Based on the Gram determinant, a new numerical procedure is presented that allows the dimensionality (in the the context of ILDMs) of any point in chemical state-space to be computed.

The ILDM algorithm was formulated based on physical arguments, and was designed to solve for a particular attractor in chemical state-space. This is discussed in the first section of Chapter 4. While the ILDM algorithm actually locates this attractor only approximately, it is shown to identify another manifold (with interesting properties) accurately. This identification inspires the development of a second, and more efficient, method for the computation of ILDM dimensionality. The ILDM is in fact non-intrinsic, in the sense that its definition depends on the coordinate system chosen. By appropriately modifying the

defining equations, coordinate independence can be restored. This result admittedly is only of theoretical interest.

In Chapter 5, a new numerical recipe for the solution of ILDMs, based on the idea of generating a manifold by space-filling trajectories, is presented. In addition to being embarrassingly parallel, it also facilitates (through increased robustness) and speeds up the computation of high-dimensional manifolds in comparison to continuation methods. It turns out, through personal communication with Professor Pope during his visit to Caltech in February 2002, that he had attempted a similar approach a decade ago without much success. The difference in this work is that the initial conditions for the space-filling trajectories are more artfully chosen.

Chapter 6 contains an introduction to the Zel'dovich-von Neumann-Döring (ZND) model for steady detonations, and illustrates the computation of ILDM dimensionality along steady ZND solutions. The effect of the missing initial transients introduced by ILDM reduction is examined based on steady flow and thermodynamic arguments.

With all these newfound tools and understanding, one would expect to find comparisons between simulations performed with detailed chemistry and its reduced chemistry sibling. The conclusion, however, is that with the current set of tools we are still unable to simulate flows of interest, such as the cellular detonation of highly sensitive mixtures (Shepherd et al., 2002), or detonating flows over projectiles (Kaneshige, 1999).

In Chapter 7, numerical simulations of detonation waves initiated by hypervelocity projectiles are presented. Using detailed kinetics, only the shock-induced combustion regime is realized, as simulating the conditions required for a stabilized detonation is beyond the reach of our current computational resources. By resorting to a one-step irreversible reaction model, the transition from shock-induced combustion to stabilized oblique detonation is observed, and an analysis of this transition based on the critical decay-rate model (see Kaneshige (1999)) is presented.

The new results presented in this thesis are summarized below.

- Two new algorithms that allow us to answer quantitatively the question: How many dimensions does the ILDM need to have?

- A description of the consequence of using an ILDM of insufficient dimensions.

- An embarrassingly parallel algorithm for the computation of ILDMs.

- Numerical simulations of projectile-initiated stabilized oblique detonations.

- Verification of the critical decay-rate criterion for projectile-stabilized detonations proposed by Kaneshige (1999), using two-dimensional simulations with one-step irreversible chemistry.

Chapter 2

Problem Formulation

In this chapter, the numerical setup and the governing equations are described. The formulation of the reactive Roe solver comes directly from Appendix B of Eckett (2001) and will not be discussed. Attention is focused on linear-algebraic preliminaries related to the chemical kinetics and mechanism reduction that will be needed in subsequent chapters.

2.1 Outline of numerical method

With transport phenomena assumed negligible, the numerical simulation of detonations is the solution of the reactive Euler equations. In the absence of volumetric or body forces, the equations for the conservation of mass, momentum and energy for the (primitive) quantities (ρ, P, u_i), written in Cartesian coordinates, are

$$\frac{\partial \rho}{\partial t} + \frac{\partial}{\partial x_j}(\rho u_j) = 0 \ ,$$

$$\frac{\partial}{\partial t}(\rho u_i) + \frac{\partial}{\partial x_j}\left(\rho u_i u_j + P\delta_{ij}\right) = 0 \ , \qquad (2.1)$$

$$\frac{\partial}{\partial t}\left(\frac{1}{2}\rho u_i u_i + \rho e\right) + \frac{\partial}{\partial x_j}\left[\left(\frac{1}{2}\rho u_i u_i + \rho e + P\right) u_j\right] = 0 \ .$$

In addition, assume that the chemical composition is specified by some state vector $\boldsymbol{z}$, which could be anything from a scalar progress variable to a vector of species mass-fractions. The evolutionary equation for the chemical composition is

$$\frac{\partial}{\partial t}(\rho z_i) + \frac{\partial}{\partial x_j}\left(\rho z_i u_j\right) = \rho \Omega_i \ , \qquad (2.2)$$

where Ω_i is the rate of change of the i-th component of the state vector $\boldsymbol{z}$. The equation

is closed with a suitable equation of state. Combining (2.1) and (2.2), the reactive Euler equations can be written in the form

$$\frac{\partial \boldsymbol{W}}{\partial t} + \frac{\partial \boldsymbol{F}_i}{\partial x_i} = \boldsymbol{S} \ , \tag{2.3}$$

where $\boldsymbol{W}$ is the vector of conserved variables, $\boldsymbol{F}_i$ are the convective fluxes, and $\boldsymbol{S}$ is the reaction source terms (see §3.2.1 of Eckett, 2001).

The reactive Euler equations are to be solved numerically using the timestep splitting technique described by Eckett (2001). The convective operator $\mathcal{L}_{F_i}$ is defined as the integration of the homogeneous part of (2.3), which can be rewritten as

$$\frac{\partial \boldsymbol{W}}{\partial t} + \frac{\partial \boldsymbol{F}_i}{\partial x_i} = \boldsymbol{0} \ . \tag{2.4}$$

Similarly, the reaction source operator $\mathcal{L}_S$ is the integration of

$$\frac{d\boldsymbol{W}}{dt} = \boldsymbol{S} \ . \tag{2.5}$$

In two dimensions, the CFD solver uses the following second-order accurate algorithm to integrate the state $\boldsymbol{W}$ by a timestep Δt (Strang, 1968):

$$\boldsymbol{W}^{t+\Delta t} = \frac{1}{2}\mathcal{L}_{F_x}\frac{1}{2}\mathcal{L}_{F_y}\mathcal{L}_S\frac{1}{2}\mathcal{L}_{F_y}\frac{1}{2}\mathcal{L}_{F_x}\boldsymbol{W}^t \ , \tag{2.6}$$

$1/2\mathcal{L}$ is the operator applied for a half-timestep $(1/2)\Delta t$. To apply the technique of mechanism reduction to detonation (using an operator-split solver as described above) is to reduce the cost of the operator $\mathcal{L}_S$, whose action is the time advancement of chemical composition for each control volume due to chemical reaction.

2.2 The adiabatic constant volume combustor

In this section, the basic mathematical structure of the evolutionary equation governing a chemically reactive system, which forms the basis of the operator $\mathcal{L}_S$ in (2.6), is presented. The linear algebraic results to be presented are fundamental to the implementation of the ILDM algorithm.

2.2.1 Problem setup

Consider a chemically reactive system and assume it to be *simple* (see Callen, 1985): macroscopically homogeneous, isotropic and uncharged. no surface effects, uninfluenced by electric, magnetic, or gravitational fields. Its evolution is governed by an ODE of the form

$$\frac{d\boldsymbol{\psi}}{dt} = \boldsymbol{f}\left(\boldsymbol{\psi}\right) \ , \tag{2.7}$$

where $\boldsymbol{\psi}$ is any set of coordinates, or parameterizations, that completely characterizes the thermo-mechanical and chemical composition of the system. A particular choice of parameterization may be

$$\boldsymbol{\psi} = [U, V, N_1, \ldots, N_{n_s}]^T \ , \tag{2.8}$$

where U is the internal energy, V is the volume, and $N_i \ldots N_{n_s}$ are the mole numbers of each of the n_s chemical species present. The symbol $\boldsymbol{N}$ will be used to denote the vector whose components are the mole numbers N_i.

Using the operator-split procedure described in the previous section, each control volume under the operator $\mathcal{L}_S$ behaves as independent, adiabatic constant volume combustors. Using the parameterization of (2.8), the governing ODE (2.7) becomes

$$\frac{d\boldsymbol{\psi}}{dt} = \boldsymbol{f}(\boldsymbol{\psi}) = \begin{pmatrix} 0 \\ 0 \\ \Omega_1(\boldsymbol{\psi}) \\ \vdots \\ \Omega_{n_s}(\boldsymbol{\psi}) \end{pmatrix} \ , \tag{2.9}$$

where Ω_i is the molar production rate for species i. The extensivity of the variable $\boldsymbol{\psi}$ (under the parameterization of (2.8)) means that its rate of change, given by $\boldsymbol{f}$ in (2.9) is a first order homogeneous function. As such, we generally prefer to use normalized forms of the mole numbers $\boldsymbol{N}$. Three common ones are the mole fractions $\boldsymbol{x}$, the mass fractions $\boldsymbol{y}$, and the molar concentrations $\boldsymbol{c}$. The first two fractions $\boldsymbol{x}$ and $\boldsymbol{y}$ are nondimensional whereas $\boldsymbol{c}$ has units of moles per unit volume. See Kee et al. (1989) for formulae that convert between these representations. For constant volume systems, the specific mole numbers $\boldsymbol{\phi}$ will be a convenient replacement for the mole fractions $\boldsymbol{x}$.

2.2.2 Representations (parameterizations) of chemical composition

In this section, the merits of the various parameterizations described in the previous section, and their effects on the function $\boldsymbol{f}$, are discussed.

The adiabatic constant volume constraint allows (2.9) to be written as

$$\frac{dN_i}{dt} = \boldsymbol{f}(\boldsymbol{N}; U, V) = \begin{pmatrix} \Omega_1(\boldsymbol{N}, U, V) \\ \vdots \\ \Omega_n(\boldsymbol{N}; U, V) \end{pmatrix}. \tag{2.10}$$

Using one of the normalized forms of the mole numbers (for example, $\boldsymbol{y}$), (2.10) can be written as

$$\frac{d\boldsymbol{y}}{dt} = \boldsymbol{f}(\boldsymbol{y}; \rho, e) = \begin{pmatrix} \omega_1(\boldsymbol{y}, \rho, e) \\ \vdots \\ \omega_n(\boldsymbol{y}; \rho, e) \end{pmatrix}, \tag{2.11}$$

where the two conserved parameters are the (mixture-averaged) density ρ and the specific internal energy e. The components of the function f in (2.11), $\omega_i(\boldsymbol{y})$, are related to the molar production rates $\Omega_i(\boldsymbol{N})$ of (2.10) in the same manner as their arguments. We therefore obtain

$$\begin{array}{ccc} \boldsymbol{N} & \xrightarrow{\ \mathbf{N2y}\ } & \boldsymbol{y} \\ \Omega \downarrow & & \downarrow \omega \\ f(\boldsymbol{N}) & \xrightarrow[\mathbf{N2y}]{} & f(\boldsymbol{y}) \end{array}, \tag{2.12}$$

where

$$y_i = \mathbf{N2y}(N_i) = N_i \frac{\mathcal{W}_i}{\mathcal{W}}. \tag{2.13}$$

$\mathcal{W}$ is the (mixture-averaged) mean molecular weight, and $\mathcal{W}_i$ are the molecular weights of the species i. The function $\mathbf{N2y}$ in (2.13) converts mole numbers to mass fractions. Its importance comes from the fact that even though the total number of moles may not be conserved in a constant-volume combustor, the total mass is. Consider the conversion function between mole numbers $\boldsymbol{N}$ and mole fractions $\boldsymbol{x}$:

$$x_i = \mathbf{N2x}(N_i) = \frac{N_i}{\sum_i Ni} \tag{2.14}$$

Because the total number of moles is not an invariant in our system, the function (2.14)

is likewise nonconstant and a commutative diagram like that of (2.12) is impossible, thus making the use of mole fractions awkward. However, It is sometimes more convenient to work with moles instead of weights. Since the conversion function between $\boldsymbol{y}$ and $\boldsymbol{\phi}$ is in fact constant for our system, we can use the specific mole numbers $\boldsymbol{\phi}$ instead of mole fractions

$$\phi_i = \mathbf{y2\phi}(y_i) = \frac{y_i}{\mathcal{W}_i} \tag{2.15}$$

The mapping from $\boldsymbol{N}$ to $\boldsymbol{\phi}$ is the composition of (2.13) with (2.15),

$$\phi_i = \mathbf{N2\phi}(N_i) = \frac{N_i}{\mathcal{W}} \ . \tag{2.16}$$

Thus, it is possible to write

$$\frac{d\boldsymbol{\phi}}{dt} = f(\boldsymbol{\phi}; \rho, e) = \begin{pmatrix} \hat{\omega}_1(\boldsymbol{\phi}, \rho, e) \\ \vdots \\ \hat{\omega}_n(\boldsymbol{\phi}; \rho, e) \end{pmatrix} , \text{ and} \tag{2.17a}$$

$$\begin{array}{ccccc} \boldsymbol{N} & \xrightarrow{\mathbf{N2y}} & \boldsymbol{y} & \xrightarrow{\mathbf{y2\phi}} & \boldsymbol{\phi} \\ \Omega \downarrow & & \downarrow \omega & & \downarrow \hat{\omega} \\ f(\boldsymbol{N}) & \xrightarrow[\mathbf{N2y}]{} & f(\boldsymbol{y}) & \xrightarrow[\mathbf{y2\phi}]{} & f(\boldsymbol{\phi}) \end{array} \ . \tag{2.17b}$$

In the next section, we will explore the structure and properties of $f(\boldsymbol{y})$ and $f(\boldsymbol{\phi})$.

2.3   Treating the elemental constraints

In a chemical mechanism with n_s species, all representations of the chemical composition are members of a linear (vector) space of dimension n_s: $\mathbf{R}^{n_s}$. Restricting our attention once again to the mass fractions $\boldsymbol{y}$ and the specific mole numbers $\boldsymbol{\phi}$, we have the following two ordinary differential equations

$$\frac{d\boldsymbol{y}}{dt} = \boldsymbol{f}(\boldsymbol{y}; \rho, e), \quad \boldsymbol{y} \in \mathbf{R}^{n_s} \tag{2.18a}$$

$$\frac{d\boldsymbol{\phi}}{dt} = \boldsymbol{f}(\boldsymbol{\phi}; \rho, e), \quad \boldsymbol{\phi} \in \mathbf{R}^{n_s} \tag{2.18b}$$

Element conservation (from not having nuclear reactions) limits the allowable forms

of $\boldsymbol{f}(\boldsymbol{y})$ and $\boldsymbol{f}(\boldsymbol{\phi})$ as follows. Consider the $n_e \times n_s$ matrix M where coefficient μ_{ij} is the number of atoms of the i-th chemical element in species j. This matrix maps the species mole numbers $\boldsymbol{N}$ to the atom mole numbers $\boldsymbol{N^e} \in \mathbf{R}^{n_e}$:

$$\mathsf{M}\boldsymbol{N} = \boldsymbol{N^e} = \text{constant} \tag{2.19}$$

Applying (2.16) to (2.19) yields

$$\mathsf{M}\boldsymbol{\phi} = \frac{\boldsymbol{N^e}}{\mathcal{W}} = \text{constant} . \tag{2.20}$$

Similarly, applying (2.13) to (2.19),

$$\mathsf{N}\boldsymbol{y} = \frac{\boldsymbol{N^e}}{\mathcal{W}} = \text{constant} , \tag{2.21}$$

where the matrix N is the mass-weighed form of M. The entries ν_{ij} of N are related to those of M by

$$\nu_{ij} = \frac{\mu_{ij}}{\mathbf{wt_j}} . \tag{2.22}$$

Given an initial composition $\boldsymbol{y}_o$, conservation then limits all admissible evolution to an $(n_s - n_e)$-dimensional affine subspace of $\mathbf{R}^{n_s}$, denoted by

$$\mathcal{E} = \{\boldsymbol{y} : \mathsf{N}\boldsymbol{y} = \mathsf{N}\boldsymbol{y}_o\} . \tag{2.23}$$

Taking the time derivative of (2.20) and (2.21) yields

$$\mathsf{M}\boldsymbol{f}(\boldsymbol{\phi}) = \mathbf{0} \longrightarrow \boldsymbol{f}(\boldsymbol{\phi}) \in \ker \mathsf{M} \text{ and} \tag{2.24a}$$

$$\mathsf{N}\boldsymbol{f}(\boldsymbol{y}) = \mathbf{0} \longrightarrow \boldsymbol{f}(\boldsymbol{y}) \in \ker \mathsf{N} . \tag{2.24b}$$

Since M and N are $n_e \times n_s$ matrices, their kernels (assuming the matrices in question have full rank) are $(n_s - n_e)$-dimensional. An equivalent definition for the affine subspace $\mathcal{E}$ in (2.23) is

$$\mathcal{E} = \boldsymbol{y}_o + \ker \mathsf{N} . \tag{2.25}$$

Within the n_s-dimensional chemical state-space, all admissible $\boldsymbol{y}$ (i.e., those that satisfy

elemental conservation) lie on an $(n_s - n_e)$-dimensional affine space with basepoint at some initial conditions $\boldsymbol{y}_o$. An affine space with basepoint at ϕ_o can be defined in exactly the same way using ker M.

Since the mass fractions $\boldsymbol{y}$ always sum to unity, there is evidently an additional constraint on $\boldsymbol{f}(\boldsymbol{y})$:

$$\sum_i^{n_s} f_i(\boldsymbol{y}) = 0 \implies \boldsymbol{f}(\boldsymbol{y}) \in \ker(\overbrace{[1, 1, \ldots, 1]}^{n_s}) \tag{2.26}$$

That (2.26) is consistent with (2.24b) or, in other words, that (2.26) does not in fact impose an additional constraint, is guaranteed by

$$\mathrm{span}([1, 1, \ldots, 1]) \subset \mathrm{span}(\mathsf{N}) . \tag{2.27}$$

(2.27) can be verified by computation: If $\mathbf{W^e}$ is the row vector of atomic weights arranged in the same order as the rows of N, then

$$\mathbf{W^e}\mathsf{N} = \overbrace{[1, 1, \ldots, 1]}^{n_s} . \tag{2.28}$$

2.3.1 Projectors for the element-conserved subspace

The singular value decompositions (SVD) of matrices M and N give us projectors that greatly simplify the computations of reduced manifolds. Let $\mathsf{M} = \mathsf{U}\Sigma\mathsf{V}^T$ be the SVD (Golub and van Loan, 1996) of the matrix M. Assuming that $n_e = \mathrm{rank}(\mathsf{M})$, the column partitioning of U and V are as follows:

$$\mathsf{U} = [\ \underset{n_e}{\mathsf{U}_r}\ ] \qquad\qquad \mathsf{V} = [\ \underset{n_e}{\mathsf{V}_r} \qquad \underset{n_s - n_e}{\tilde{\mathsf{V}}_r}\ ] \tag{2.29}$$

Denoting the matrix transpose of $\tilde{\mathsf{V}}_r$ by P_M,

$$\mathsf{P}_M\mathsf{P}^\mathsf{T}_M = \mathsf{I} \in M_{n_s - n_e} \text{ and}$$
$$\mathsf{P}^\mathsf{T}_M\mathsf{P}_M = \text{orthogonal projection onto } \ker(\mathsf{M}) \quad \mathsf{P}^\mathsf{T}_M\mathsf{P}_M \in M_{n_s} . \tag{2.30}$$

The notation M_n denotes a square matrix of size n. The matrix P_N is defined exactly as above with the SVD on the matrix N. Using (2.24a) and (2.24b),

$$\mathsf{P^T}_M \mathsf{P}_M \cdot \boldsymbol{f}(\boldsymbol{\phi}) = \boldsymbol{f}(\boldsymbol{\phi}) \text{ and}$$
$$\mathsf{P^T}_N \mathsf{P}_N \cdot \boldsymbol{f}(\boldsymbol{y}) = \boldsymbol{f}(\boldsymbol{y}) \ . \tag{2.31}$$

To simplify the notation, the subscripts M and N will be dropped when there is no danger of confusion, giving

$$\mathsf{P^T P} \cdot \boldsymbol{f} = \boldsymbol{f}, \text{ and } \mathsf{PP^T} = \mathsf{I} \ . \tag{2.32}$$

The matrix P and its properties in (2.32) will allow significant simplifications in the implementation of the ILDM algorithm.

2.4 An alternate formulation: the temperature-extended phase space

While (2.18a) and (2.18b) rely on the two conserved quantities ρ and e as parameters, the molar production rates of species are more naturally expressed as functions of ρ and T. The disadvantage of the formulation as stated is that the temperature T is needed to calculate the reaction rates. For an ideal gas, this means that the implicit solution of T in $e = e(\boldsymbol{y}, T)$ is required for each functional evaluation of $\boldsymbol{f}$.

For an ideal mixture, an alternative formulation circumvents this implicit solution by carrying the temperature T as an additional variable. Assuming that mass fractions $\boldsymbol{y}$ are being used (the application to $\boldsymbol{\phi}$ is exactly analogous), introduce the new vector $\bar{\boldsymbol{y}}$ by

$$\bar{\boldsymbol{y}} = [T, \boldsymbol{y}]^T \in \mathbf{R}^{n_s+1} \ . \tag{2.33}$$

This $(n_s + 1)$-dimensional space will be labeled the *temperature-extended* phase space. The evolutionary equation for $\bar{\boldsymbol{y}}$ is

$$\frac{d\bar{\boldsymbol{y}}}{dt} = \bar{\boldsymbol{f}}(\bar{\boldsymbol{y}}; \rho) = \begin{pmatrix} dT/dt \\ \boldsymbol{f}(\boldsymbol{y}) \end{pmatrix} . \tag{2.34}$$

An evolution equation for the temperature is needed to complete (2.34). The mixture-

averaged internal energy e for an ideal mixture (part of the Gibbs-Dalton Law) is

$$e(T, y_i) = \sum_{i=1}^{n} e_i(T) y_i \ , \tag{2.35}$$

where e_i is the specific internal energy of species i. The differential de in coordinates $\bar{\boldsymbol{y}}$ is

$$\mathsf{de}(T, y_1, \ldots, y_{n_s}) = \left. \frac{\partial e}{\partial T} \right|_{\boldsymbol{y}} dT + \left. \frac{\partial e}{\partial y_1} \right|_{T, y_{j \neq 1}} dy_1 + \ldots + \left. \frac{\partial e}{\partial y_{n_s}} \right|_{T, y_{j \neq \_ns}} dy_{n_s} \ . \tag{2.36}$$

Substituting in the (mixture-averaged) specific heat at constant volume c_v for the first partial derivative in (2.36) and using (2.35), the differential form de in the (dual) coordinates of $\bar{\boldsymbol{y}}$ is

$$\mathsf{de} = [c_v, e_1, \ldots, e_{n_s}] \ . \tag{2.37}$$

Setting $\mathsf{de} = 0$ (for the adiabatic constant volume system), the temperature derivative needed for (2.34) is

$$\frac{dT}{dt} = -c_v(T, \boldsymbol{y})^{-1} \sum_{i=1}^{n} e_i(T) \frac{dy_i}{dt} \ . \tag{2.38}$$

By construction ((2.37) and (2.38)),

$$\langle \mathsf{de}, \bar{\boldsymbol{f}}(\bar{\boldsymbol{y}}) \rangle = 0 \longrightarrow \bar{\boldsymbol{f}}(\bar{\boldsymbol{y}}) \in \ker(\mathsf{de}) \ , \tag{2.39}$$

which is a statement of the conservation of energy that constrains the possible form of $\bar{\boldsymbol{f}}$.

A disadvantage of this formulation is that errors from integrating (2.34) will lead to a drift in the internal energy, and hence the equilibrium point, of the system. In contrast to the system in (2.18a), however, this formulation allows the Jacobian matrix to be computed very efficiently. This Jacobian, and various useful identities related to this matrix, is the subject of the next section.

2.5 The Jacobian matrix

The Jacobian matrix $\mathsf{J}(\boldsymbol{y})$ of $f(\boldsymbol{y}; \rho, e)$ in (2.18a) is

$$\mathsf{J}(\boldsymbol{y}) = \begin{pmatrix} \frac{\partial f_1}{\partial y_1}, & \cdots, & \frac{\partial f_1}{\partial y_{n_s}} \\ \vdots & \ddots & \vdots \\ \frac{\partial f_{n_s}}{\partial y_1}, & \cdots, & \frac{\partial f_{n_s}}{\partial y_{n_s}} \end{pmatrix}, \quad \mathsf{J}(\boldsymbol{y}) \in M_{n_s} , \tag{2.40}$$

The components J_{ij} of J evaluated at $\boldsymbol{y}$ are, more verbosely,

$$J_{ij}(\boldsymbol{y}) = \left. \frac{\partial f_i(\boldsymbol{y})}{\partial y_j} \right|_{\rho, e, y_{i \neq j}} . \tag{2.41}$$

Because the Jacobian matrix in (2.40) consists of partial derivatives computed with ρ and e fixed, it will be called an *adiabatic constant-volume* Jacobian. The Jacobian for the extended system $\bar{\boldsymbol{f}}(\bar{\boldsymbol{y}}; \rho)$ (2.34), writing dT/dt of (2.34) as $\dot{T}$, is

$$\mathsf{J}^+(\bar{\boldsymbol{y}}) = \begin{pmatrix} \frac{\partial \dot{T}}{\partial T} & \frac{\partial \dot{T}}{\partial y_1}, & \cdots, & \frac{\partial \dot{T}}{\partial y_{n_s}} \\ \frac{\partial f_1}{\partial T} & \frac{\partial f_1}{\partial y_1} & \cdots, & \frac{\partial f_1}{\partial y_{n_s}} \\ \vdots & \vdots & \ddots & \vdots \\ \frac{\partial f_{n_s}}{\partial T} & \frac{\partial f_{n_s}}{\partial y_1}, & \cdots, & \frac{\partial f_{n_s}}{\partial y_{n_s}} \end{pmatrix}, \quad \mathsf{J}^+(\bar{\boldsymbol{y}}) \in M_{n_s+1} . \tag{2.42}$$

Unlike J, the (numerical) Jacobian matrix J^+ can be computed economically because the internal energy e is no longer held fixed.

If $\mathsf{J}^\diamond$ is the $n_s \times n_s$-submatrix and $\boldsymbol{\beta}$ is the $n_s \times 1$-submatrix of J^+ in (2.42), then

$$J_{ij}^\diamond = \left. \frac{\partial f_i}{\partial y_j} \right|_{\rho, T, y_{i \neq j}} \quad \text{and} \quad \beta_i = \left. \frac{\partial f_i}{\partial T} \right|_{\boldsymbol{y}} . \tag{2.43}$$

The two matrices J and $\mathsf{J}^\diamond$ are related by

$$J_{ij} = J_{ij}^\diamond - \left. \frac{\partial e}{\partial T} \right|_{\boldsymbol{y}}^{-1} \left. \frac{\partial f_i}{\partial T} \right|_{\boldsymbol{y}} \left. \frac{\partial e}{\partial y_j} \right|_{T, y_{i \neq j}} = J_{ij}^\diamond - \frac{\beta_i e_j}{c_v} . \tag{2.44}$$

If an implicit ODE solver is used to integrate (2.34), then the full Jacobian of (2.42) is needed. However, when an adiabatic constant-volume Jacobian of (2.40) is sought, whether for the numerical integration of (2.18a) or for use in the implementation of the Maas and

Mixture J	
Composition	CH_4–$2O_2$–$7.52N_2$
Initial Temperature	1500 K
Initial Pressure	10 atm
Reaction Mechanism	GRIMech-3.0

Table 2.1: Properties and reaction mechanism for mixture J used for Jacobian illustrations.

Pope algorithm, it is much more efficient (and often more accurate) to compute J^+ first and then obtain J using (2.44).

2.5.1 Sparsity of the Jacobian matrix

The constant-volume trajectory for the mixture indicated in Table 2.1, together with sparsity plots of the Jacobian matrix at the initial composition, equilibrium point, and two intermediate compositions are computed and plotted in Figure 2.1. The Jacobian is sparse at the initial composition because only 3 of the 53 species of the GRIMech-3.0 mechanism (see Smith et al., 2003) are present. The 49th row is zero for all four matrices because the 49th species, argon, is non-reactive.
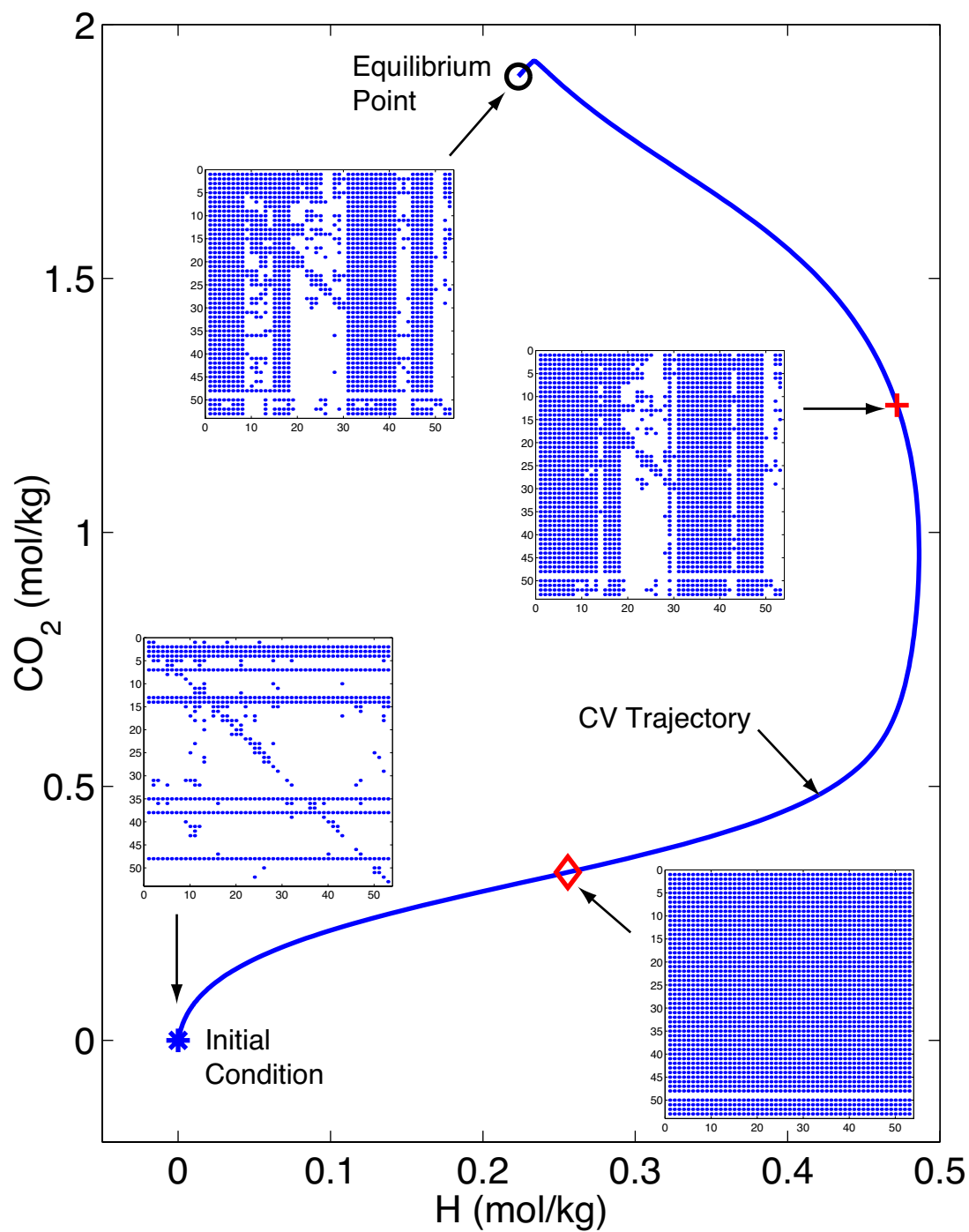
Figure 2.1: Constant volume trajectory and Jacobian for the mixture indicated in Table 2.1.

Chapter 3

Intrinsic Low Dimensional Manifolds

Intrinsic Low Dimensional Manifold (ILDM) is a technique for systematically identifying low-dimensional submanifolds of the original state space of chemically reactive systems (Maas and Pope, 1992b). The method, originally developed for low-speed combustion systems, has been successfully extended and applied to two dimensional gaseous detonation simulations with the hydrogen-oxygen reaction mechanism by Eckett (2001) and Singh et al. (2001b), and to gas phase RDX combustion by Singh and Powers (1999). While detailed reaction mechanisms are now mature for many hydrocarbon fuels, and in a developmental stage for nitramine explosives such as RDX and HMX, a number of issues remain to be addressed before they can be used in conjunction with the ILDM method for detonation simulations.

First, the ILDM algorithm is computationally expensive to apply, and the computed manifold presents difficult tabulation, storage, and interpolation problems. While a one-dimensional ILDM can be computed reasonably easily and has been shown to work well for simple reaction systems such as the Hydrogen-Oxygen reaction mechanism, it is not reasonable to expect such a drastic reduction to be faithful to even moderately complex hydrocarbon mechanisms.

The motivation for using ILDMs is simple: we want to extract as much information from the detailed mechanism as we can afford, and using the minimum that we can get away with. The ILDM technique allows us to approach, if not reach, this goal systematically. Unfortunately, the choice of the reduced manifold's dimension, in addition to being largely ad-hoc, is usually limited by what we can afford. In this chapter, a new algorithm is presented that quantitatively tells us if what we can afford is sufficient. Algorithms that solve for the ILDMs directly, the most popular being continuation methods, are far from

robust. In this chapter, a new indirect algorithm for the computation of ILDMs that is more efficient, embarrassingly parallel, and far more robust than continuation methods, is presented.

3.1 Defining the ILDM: The Maas and Pope Algorithm

The presentation in this section uses only the mass fractions $\boldsymbol{y}$. The algorithm is exactly the same for $\boldsymbol{\phi}$ because the Maas and Pope algorithm is invariant under linear changes of coordinates.

The ILDM is defined by the Maas and Pope algorithm (Maas and Pope, 1992a), the essence of which is summarized here. Consider a vector field (or equivalently, a dynamical system) such as

$$\frac{d\boldsymbol{y}}{dt} = \boldsymbol{f}(\boldsymbol{y}), \quad \boldsymbol{y} \in \mathbf{R}^{n_s} . \tag{2.18a}$$

(reproduced with the parametric dependence on (ρ, e) removed). Assume that the Jacobian J is nondefective (i.e., diagonalizable) (see Horn and Johnson, 1985, for an introduction). Then at each point $\boldsymbol{y}$ it admits the decomposition

$$\mathsf{J} = \mathsf{V}\Lambda\mathsf{V}^{-1} , \tag{3.1}$$

where $\Lambda = \mathrm{diag}\{\lambda_1, \ldots, \lambda_{n_s}\}$ is the diagonal eigenvalue matrix. Denoting the set of eigenvalues by $\sigma(\mathsf{J})$, the spectrum of J can be written as

$$\sigma(\mathsf{J}) = \{\lambda_1, \lambda_2, \ldots, \lambda_{n_s}\} . \tag{3.2}$$

Assume that all the eigenvalues are real and, without loss of generality, sorted in descending order ($\lambda_i >= \lambda_j$ if $i > j$). Assume further that the eigenvalues are partitionable into two (slow and fast) sets,

$$
\begin{aligned}
\sigma_s &= \{\lambda_1, \lambda_2, \ldots, \lambda_k\} & \Lambda_s &= \mathrm{diag}\{\sigma_s\} \ \ \text{and} \\
\sigma_f &= \{\lambda_{k+1}, \lambda_{k+1}, \ldots, \lambda_{n_s}\} & \Lambda_f &= \mathrm{diag}\{\sigma_f\} .
\end{aligned}
\tag{3.3}
$$

The decomposition in (3.1) becomes

$$J = \begin{pmatrix} | & | \\ V_s & V_f \\ | & | \end{pmatrix} \begin{pmatrix} \Lambda_s & 0 \\ 0 & \Lambda_f \end{pmatrix} \begin{pmatrix} - \hat{V}_s - \\ - \hat{V}_f - \end{pmatrix}, \tag{3.4}$$

where $\hat{V}_s$ is a column partitioning of (eigen)-vectors spanning the slow subspace, defined to be the invariant eigenspace of J associated with the largest (least negative) eigenvalues. A different basis, in particular an orthonormal one from Schur decomposition, can be used instead. An k-dimensional ILDM, denoted by $\mathcal{M}^k$ is defined by

$$\mathcal{M}^k = \{ \boldsymbol{y} : \hat{V}_f \boldsymbol{f}(\boldsymbol{y}) = \boldsymbol{0} \} , \tag{3.5}$$

where

$$\hat{V}_f \boldsymbol{f}(\boldsymbol{y}) : \mathbf{R}^{n_s} \to \mathbf{R}^{n_s - k} . \tag{3.6}$$

The definition in (3.5) is numerically awkward for the following reasons. The ILDM, like the QSSA constraint of (1.12), is defined as the zero level-set of a complicated nonlinear function (3.6). One-dimensional level-sets are not difficult to find by continuation methods, but higher-dimensional level-surfaces are tricky. Conservation of mass poses an additional complication: each (independent) elemental constraint increases the multiplicity of the zero eigenvalue by one. This comes from the fact that all admissible $\boldsymbol{y}$ live in the affine subspace $\mathcal{E}$ (defined by (2.23)) which is an n_e-codimensional subspace of the original state space. Thus, to obtain a k-dimensional manifold *on* $\mathcal{E}$, it has to be "cut" from $\mathcal{M}^{n_e + k}$. This procedure is described in almost all literature that concerns the practical implementation of the method, for example, in §3.4.2 of Eckett (2001).

Finally, and most importantly, the definition depends on the function $\hat{V}_f \boldsymbol{f}$, which is highly nonlinear. Being a composite function where $\hat{V}_f$ comes, for example, from matrix inversion or Schur decomposition (which does not give unique basis vectors), the null space of $d(\hat{V}_f \boldsymbol{f})$ needed for continuation procedures cannot be accurately computed and must be approximated.

3.2 Recasting the ILDM algorithm

The disadvantages in the previous section notwithstanding, the ILDM as formulated by the Maas and Pope algorithm does have its advantages. Unlike the QSSA method, it provides the functional constraint explicitly. It also suggests a direct method of solving for $\mathcal{M}^k$, as long as level-surfaces can be computed.

By examining (3.5), a point $\boldsymbol{y}$ in chemical state-space $\mathbf{R}^{n_s}$ is in $\mathcal{M}^k$ when $\boldsymbol{f}(\boldsymbol{y})$, transformed to the new basis spanned by the slow and fast eigenvectors $(\mathsf{V}_s, \mathsf{V}_f)$, has no components in the fast subspace. In other words,

$$\boldsymbol{y} \in \mathcal{M}^k \iff \boldsymbol{f}(\boldsymbol{y}) \in \operatorname{span} \mathsf{V}_s \ . \tag{3.7}$$

This definition of $\mathcal{M}^k$ has a very desirable property: only *right* eigenvectors are needed to compute a basis for V_s. In addition, elemental conservation can be easily accounted for by excluding the n_e eigenvectors associated with element conservation from V_s. In fact, using the matrix P of (2.32), define $\mathsf{J}^\flat$ by

$$\mathsf{J}^\flat = \mathsf{P}\mathsf{J}\mathsf{P}^\mathsf{T}, \quad \mathsf{J}^\flat \in M_{n_s - n_e} \ . \tag{3.8}$$

Partition the eigenvalues of J into two sets, where the set σ_1 consists of eigenvalues that correspond to the conserved eigenvectors (this does not exclude the possibility of having zero eigenvalues in σ_2). Then

$$\sigma(\mathsf{J}) = \sigma_1(\mathsf{J}) \cup \sigma_2(\mathsf{J}) \ , \tag{3.9}$$

where

$$\begin{aligned} \sigma_1(\mathsf{J}) &= \{\overbrace{0, 0, \dots, 0}^{n_e \text{ elements}}\} \quad \text{and} \\ \sigma_2(\mathsf{J}) &= \{\lambda_1, \lambda_2, \dots, \lambda_{n_s - n_e}\} \ . \end{aligned} \tag{3.10}$$

Using the properties of (2.32), it can be shown that

$$\sigma(\mathsf{J}^\flat) = \sigma_2(\mathsf{J}) \ . \tag{3.11}$$

Thus an eigenvalue λ_i of J that is not associated with a conserved eigenvector is also an

eigenvalue of the matrix $\mathsf{J}^\flat$. In fact,

$$\mathsf{J}v_i = \lambda_i v_i \iff \mathsf{J}^\flat v_i^\flat = \lambda_i v_i^\flat \ . \tag{3.12}$$

The eigenvectors of J are isometrically isomorphic to those of $\mathsf{J}^\flat$:

$$v_i = \mathsf{P}^\mathsf{T} v_i^\flat$$
$$v_i^\flat = \mathsf{P} v_i \tag{3.13}$$
$$\|v_i^\flat\| = \|v_i\|$$

By using (3.12) and (3.13), element conservation can be automatically accounted for. More importantly, this prevents the numerical algorithms from mistaking a very small (or even zero) eigenvalue in σ_2 (that does not come from elemental conservation) for a conserved eigenvalue.

Although (3.7) does not provide a *constructive* definition for $\mathcal{M}^k$, it poses and answers an important inverse question: What is the ILDM dimensionality of $\boldsymbol{y}$? Define the ILDM dimension of $\boldsymbol{y}$ by

$$\text{ILDM-dim}(\boldsymbol{y}) = \min(k) : \boldsymbol{y} \in \mathcal{M}^k \ . \tag{3.14}$$

The ILDM dimension is well-defined (so the use of min above makes sense) when the following inclusion property holds

$$\mathcal{M}^i \subseteq \mathcal{M}^j \ \forall \ i < j \tag{3.15}$$

In the next section, one simple technique for calculating this ILDM dimension will be discussed. Meanwhile, it is worth noting that the inclusion property (3.15) will fail when the multiplicity of a certain eigenvalue becomes larger than two. This is a pathological condition and is true, in general, only for the zero eigenvalue. For example, if elemental conservation is not taken into account then $\mathcal{M}^i \subseteq \mathcal{M}^{n_e}$ for $i < n_e$, but it is not necessarily true that $\mathcal{M}^i \subseteq \mathcal{M}^j$ for $i < j \leq n_e$. This isn't a problem when conservation is accounted for.

A much more serious, but subtle, problem occurs when (3.5) fails to be well defined. This is because a spectral gap condition is hidden between the definition of the ILDM in
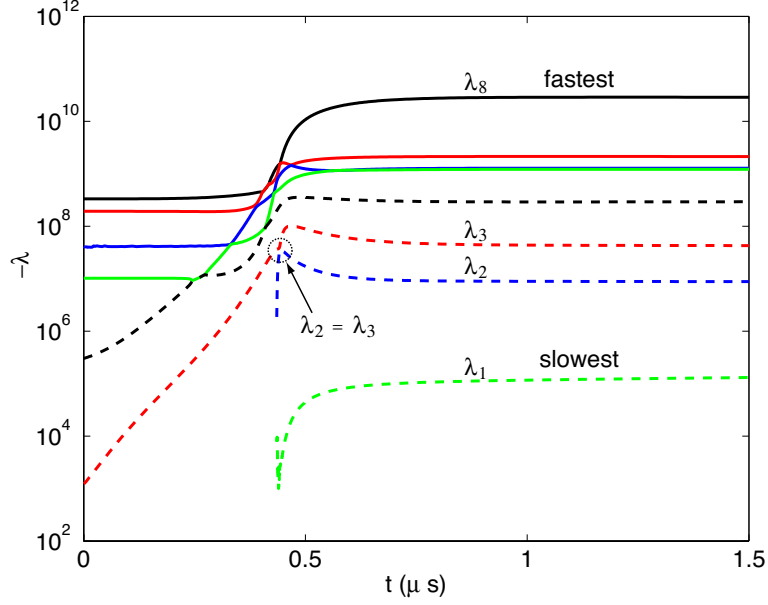
Figure 3.1: Eigenvalue evolution of Mixture A (Table 3.1).

(3.5) and the partition defined in (3.3), reproduced below.

$$\sigma_s = \{\lambda_1, \lambda_2, \ldots, \lambda_r\} \qquad \Lambda_s = \text{diag}\{\sigma_s\}$$
$$\sigma_f = \{\lambda_{r+1}, \lambda_{r+1}, \ldots, \lambda_{n_s}\} \qquad \Lambda_f = \text{diag}\{\sigma_f\} \tag{3.3}$$

The function $\hat{V}_f \boldsymbol{f}(\boldsymbol{y})$ in (3.5) used in the Maas and Pope algorithm is unambiguously defined only when the strict inequality $\lambda_r < \lambda_{r+1}$ holds or, in other words, when there is a gap between σ_s and σ_f in (3.3), i.e.,

$$\min \sigma_s > \max \sigma_f \ . \tag{3.16}$$

While it is unlikely that at any given point $\boldsymbol{y}$ the spectral gap becomes zero (and closes), the likelihood increases when the eigenvalues along an entire trajectory are taken into account. For example, consider the constant-volume explosion of Mixture A in Table 3.1 (to be discussed in detail in the next section). The eigenvalue evolution as a function of time is plotted in Figure 3.1.

From the figure, it can be seen that, after the initial transients, the eigenvalues become steady and gaps exist between all eigenvalues. However, just before t = 0.5 μs, many eigenvalues pair-up and "cross". One such pair is labeled on the figure.

3.3 ILDM dimensionality and the Grammian procedure

The definition of the ILDM can be used to compute ILDM-dim $(\boldsymbol{y})$ by writing $\boldsymbol{f}(\boldsymbol{y})$ in a sorted eigenbasis and counting the number of zeros in $\mathsf{V}^{-1}\boldsymbol{f}(\boldsymbol{y})$. However, this is numerically ill-posed, in part because of numerical imprecision and round-off errors, but more importantly because $\mathcal{M}^k$ is, in general, not an invariant manifold. Nevertheless, (3.14) does provide a viable and direct algorithm for estimating ILDM-dim $(\boldsymbol{y})$. Define the k-dimensional Gram determinant or Grammian (see Courant and Hilbert, 1989) at $\boldsymbol{y}$, denoted $\Gamma^k(\boldsymbol{y})$, by

$$\Gamma^k(\boldsymbol{y}) = \det(\mathsf{A_k}^T\mathsf{A_k}) , \tag{3.17}$$

where the matrix $\mathsf{A_k}$ is an $n_s \times (k+1)$ matrix consisting of a column partitioning of the k slowest eigenvectors, augmented by an arc-length normalized $\boldsymbol{f}(\boldsymbol{y})$:

$$\mathsf{A_k} = \begin{pmatrix} | & | & & | & | \\ v_1 & v_2 & \ldots & v_k & \boldsymbol{g}(\boldsymbol{y}) \\ | & | & & | & | \end{pmatrix} , \quad \text{and} \quad \boldsymbol{g}(\boldsymbol{y}) = \frac{\boldsymbol{f}(\boldsymbol{y})}{\|\boldsymbol{f}(\boldsymbol{y})\|} . \tag{3.18}$$

To take care of element conservation, the eigenvectors $v^\flat$ of $\mathsf{J}^\flat$ can be used instead, and the arc-length normalized version of $g^\flat = \mathsf{P}g$ will be needed. The resulting matrix $\mathsf{A_k}^\flat \in M_{n_s-n_e,k+1}$ satisfies

$$\mathsf{A_k}^\flat = \mathsf{PA_k} \quad \text{and}$$
$$\mathsf{A_k} = \mathsf{P^T A_k}^\flat . \tag{3.19}$$

The Gram determinant is therefore invariant with respect to the isometrically isomorphic mapping between the $(n_s - n_e)$-dimensional subspace of n_s-dimensional configuration space and the reduced $(n_s - n_e)$-dimensional conserved configuration space. That is,

$$\Gamma^k(\boldsymbol{y}) = \det(\mathsf{A_k}^T\mathsf{A_k}) = \det(\mathsf{A_k}^{\flat T}\mathsf{A_k}^\flat) . \tag{3.20}$$

The definition of Γ^k satisfies the inclusion relation of (3.15),

$$\Gamma^i(\boldsymbol{y}) < \Gamma^j(\boldsymbol{y}), \qquad \forall \, i > j . \tag{3.21}$$

Mixture ID:	*Mixture A*
Composition	$2H_2$–O_2–$3.76N_2$
Density (kg/m^3)	4.58
Internal Energy (MJ/kg)	1.27
Reaction Mechanism	Hydrogen-Oxygen

Table 3.1: Properties and reaction mechanism for Mixture A.

Additionally, the Gram determinant is non-negative and bounded above by one:

$$1 \geq \Gamma^i(\boldsymbol{y}) \geq 0 \ \forall \ i \qquad (3.22)$$

Furthermore, $\Gamma^k(\boldsymbol{y})$, viewed as a scalar valued function on $(k+1)$ vectors, is continuous, so small perturbations on these vectors lead to small perturbations on $\Gamma^k(\boldsymbol{y})$. These properties allow the ILDM dimension to be computed by

$$\text{ILDM-dim}\,(\boldsymbol{y}) = \min(k) : \Gamma^k(\boldsymbol{y}) < \epsilon \ . \qquad (3.23)$$

The definition of ILDM-dim $(\boldsymbol{y})$ in (3.23) depends on a parameter ϵ, exactly analogous to the concept of numerical rank (or ϵ-rank) for matrices (see Golub and van Loan, 1996).

This technique can be illustrated by computing the ILDM dimension along a constant volume reaction trajectory. Given an ODE of the form (2.18a), with initial conditions $\boldsymbol{y}_o$, the trajectory $\boldsymbol{y}(t)$ satisfies

$$\begin{aligned} \boldsymbol{y}(0) &= \boldsymbol{y}_o \ \text{ and} \\ \dot{\boldsymbol{y}}(t) &= \boldsymbol{f}\,(\boldsymbol{y}(t); \rho, e) \ , \end{aligned} \qquad (3.24)$$

where $\dot{\boldsymbol{y}}(t) = d/dt \ \boldsymbol{y}(t)$ is the velocity of the trajectory at time t.

Figure 3.2 shows a constant-volume reaction trajectory for the stoichiometric combustion of hydrogen-air. Initial conditions, and the reaction mechanism employed, are described in Table 3.1. These conditions correspond to an initial temperature of 1543.4 K and an initial pressure of 2.8104 MPa, approximately the von Neumann state of a CJ detonation of the mixture (see §3.4.4 of Eckett, 2001).

The first three Gram determinants along the trajectory, i.e., $\Gamma^i\,(\boldsymbol{y}(t))$, $i = 1, 2, 3$ are shown in Figure 3.3. This figure has two interesting interpretations. It can be seen, for example at around 1 μs, that the only non-zero Gram determinant is Γ^1. It follows from (3.7) that the ILDM dimensionality of the trajectory at that instant is 2. Since $\Gamma^2 \leq \epsilon$,
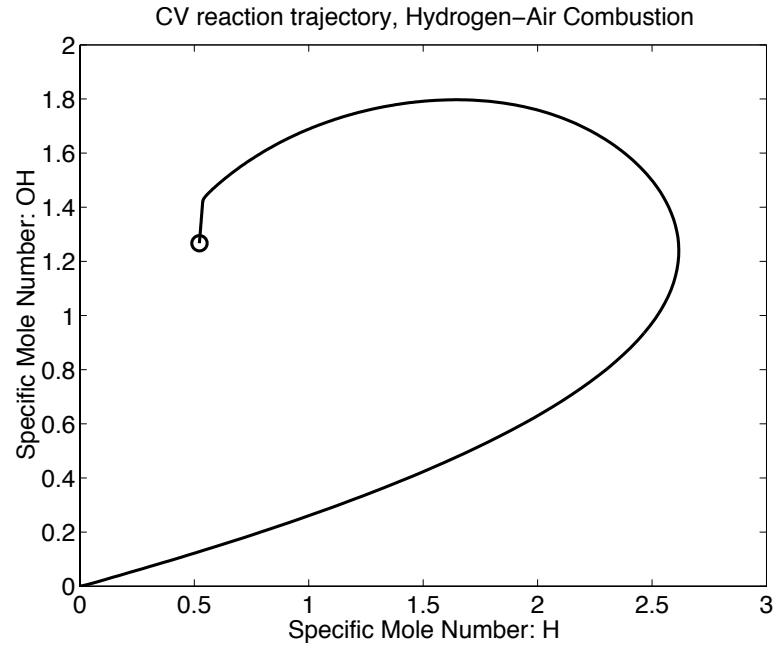
Figure 3.2: Constant-volume trajectory for hydrogen-air combustion (Mixture A, Table 3.1).
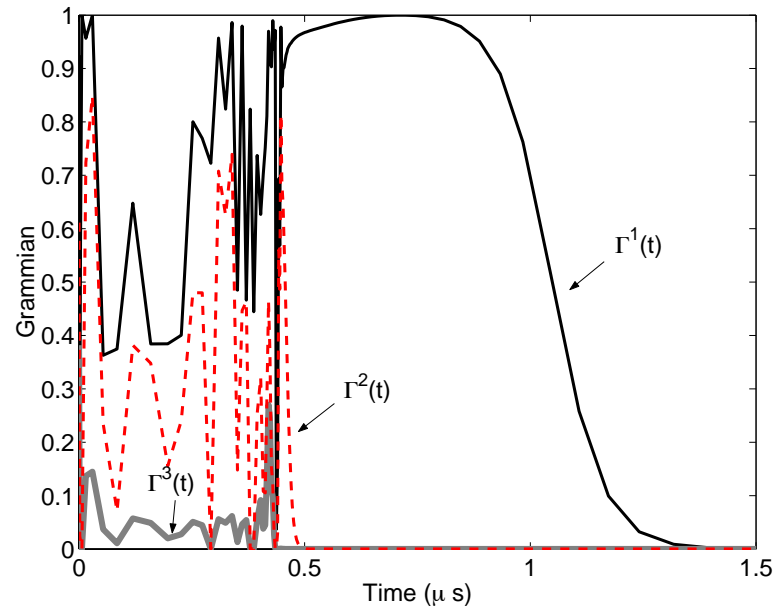
Figure 3.3: The first three Gram determinants along the CV trajectory of Figure 3.2 are plotted as a function of time.
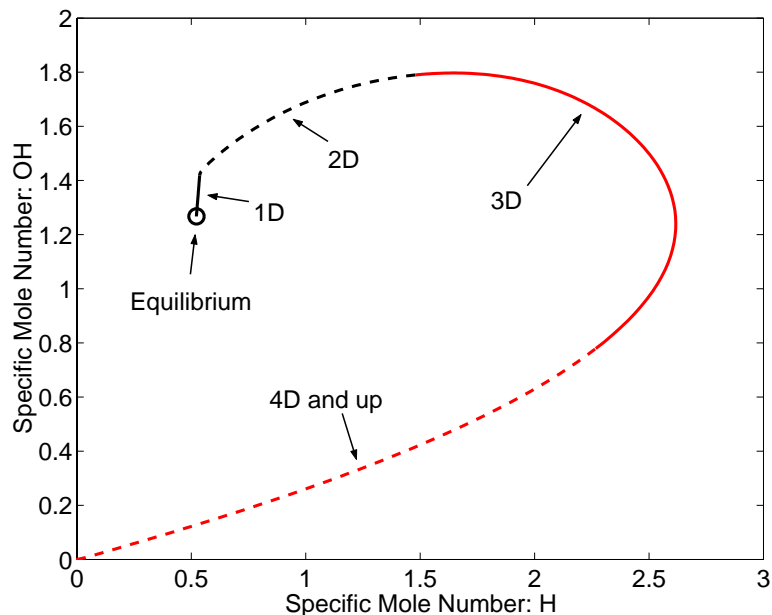
Figure 3.4: The ILDM dimension is shown along the CV trajectory of Figure 3.2.

two eigenvectors are sufficient to span $\boldsymbol{f}(\boldsymbol{y})$, and since $\Gamma^1 > \epsilon$, at least two eigenvectors are necessary. Define the *time of arrival* t_k of a trajectory $\boldsymbol{y}(t)$ to $\mathcal{M}^k$ by

$$t_k = \min \tau : \Gamma^k(\boldsymbol{y}(t)) \leq \epsilon \ \forall \ t > \tau \ . \tag{3.25}$$

Using this concept, it can be seen from Figure 3.3 that the time of arrival to $\mathcal{M}^3$, $\mathcal{M}^2$, and $\mathcal{M}^1$ are, approximately, 0.4, 0.5 and 1.5 microseconds respectively.

In Figure 3.4, the trajectory in Figure 3.2 is decorated with the ILDM dimension estimated by the Grammian procedure. This ability to compute the ILDM dimension of any point $\boldsymbol{y}$ in chemical state-space forms the basis of the proposed embarrassingly parallel algorithm for ILDM computations, to be described in Chapter 5. Another procedure that is more computationally efficient than the Grammian technique, based on arc-length normalization, will be described in §4.4.

Chapter 4

Interpretations of the Maas and Pope Algorithm

In this chapter, multiple interpretations of the intrinsic low dimensional manifold reduction technique are discussed, and the algorithm is analyzed by studying the mathematical structure of the ILDM equation (3.5). An example of the classical interpretation of fast processes vs. slow processes is given. Finally, somewhat more mathematical constructs are explored, including an arc-length reparameterization technique that leads to a very efficient procedure for computing ILDM dimensions.

4.1 The classical interpretation

The ILDM method of Maas and Pope (1992b) is an algorithmic extension of the well-known concepts of quasi-steady-state and partial-equilibrium (QSSA). The idea is that each species that is in quasi-steady state, and each reaction that is in partial-equilibrium, will incrementally constrain the possible kinetics of the system and reduce its complexity. Unfortunately, a global application of this concept is destined to be inaccurate and non-robust, because the set of reactions and species that is in QSSA depends in general on the composition and the thermodynamic state. Furthermore, for immature chemical mechanisms that are not yet fully understood, picking this set of species and reactions relies completely on chemists' intuition, and the path to reduction is taken by a leap of faith.

By linearizing the reaction rates at any thermodynamic state, linear combinations of species corresponding to eigenvectors in chemical state-space can be formed, and by using the eigenvalues as indicators, a locally optimized reduced system can be computed.

The classical interpretation is that eigenvectors of the Jacobian matrix represent *aggregate reaction pathways*, and their associated values determine the rates of these pathways. It is to be expected that during a chemically reactive process, the fastest reactions will equilibrate before the slower ones. As such, in the vicinity of the equilibrium point, only the slowest reaction remains active. Furthermore, the slowest reaction (the eigenvector corresponding to the slowest, or least negative, eigenvalue) is not assumed constant, which is the reason why the ILDM is often called *locally optimized.*

To illustrate, consider again the CV system of Mixture A (Table 3.1). The slowest eigenvectors at the equilibrium point, and the two slowest at the point marked "2D" in Figure 3.4, are tabulated in Table 4.1. In the table, the slowest eigenvalue-eigenvector pair, $(\lambda_1, \boldsymbol{v}_1)$, for the Jacobian matrix at the equilibrium point appears in the first column. The pairs $(\lambda_1, \boldsymbol{v}_1)$ (slowest) and $(\lambda_2, \boldsymbol{v}_2)$ (second slowest) are listed in the first and second columns, respectively, for the point indicated by "2D" in Figure 4.1.

The eigenvectors, to be interpreted as reaction vectors, are shown in Figure 4.1. These reaction vectors are indicated on the figure as reversible reactions (only components with values greater than 0.06 (mol/kg) in Table 4.1 are shown).

Consider the point marked "2D", computed in §3.3 to be on $\mathcal{M}^2$. The tangent to the reaction trajectory there is spanned by the two slowest eigenvectors $(\boldsymbol{v}_1, \boldsymbol{v}_2)$ of the Jacobian matrix. In comparison, the trajectory near the equilibrium is tangent to the slowest eigenvector $\boldsymbol{v}_1$. By viewing the eigenvectors as reactions, it can be seen that the slowest process $\boldsymbol{v}_1$ at both points is related to the species NO, although the coefficients are different.

As discussed previously, a point lies on an n-dimensional ILDM if the tangent vector at that point is spanned by the n *slowest* eigenvectors, and not just n eigenvectors. At "2D," the reaction is visually tangent to $\boldsymbol{v}_2$, meaning that the dominant process is production of water ($\boldsymbol{v}_2$), and the production of NO ($\boldsymbol{v}_1$) is still dormant.

4.2   ILDM under coordinate transformation

In this section, behavior of the ILDM algorithm (3.5) under coordinate transformations and reparameterizations is explored. As alluded to in §3.1, the ILDM is in fact invariant under linear changes of coordinates. This means that the ILDM computed using specific mole
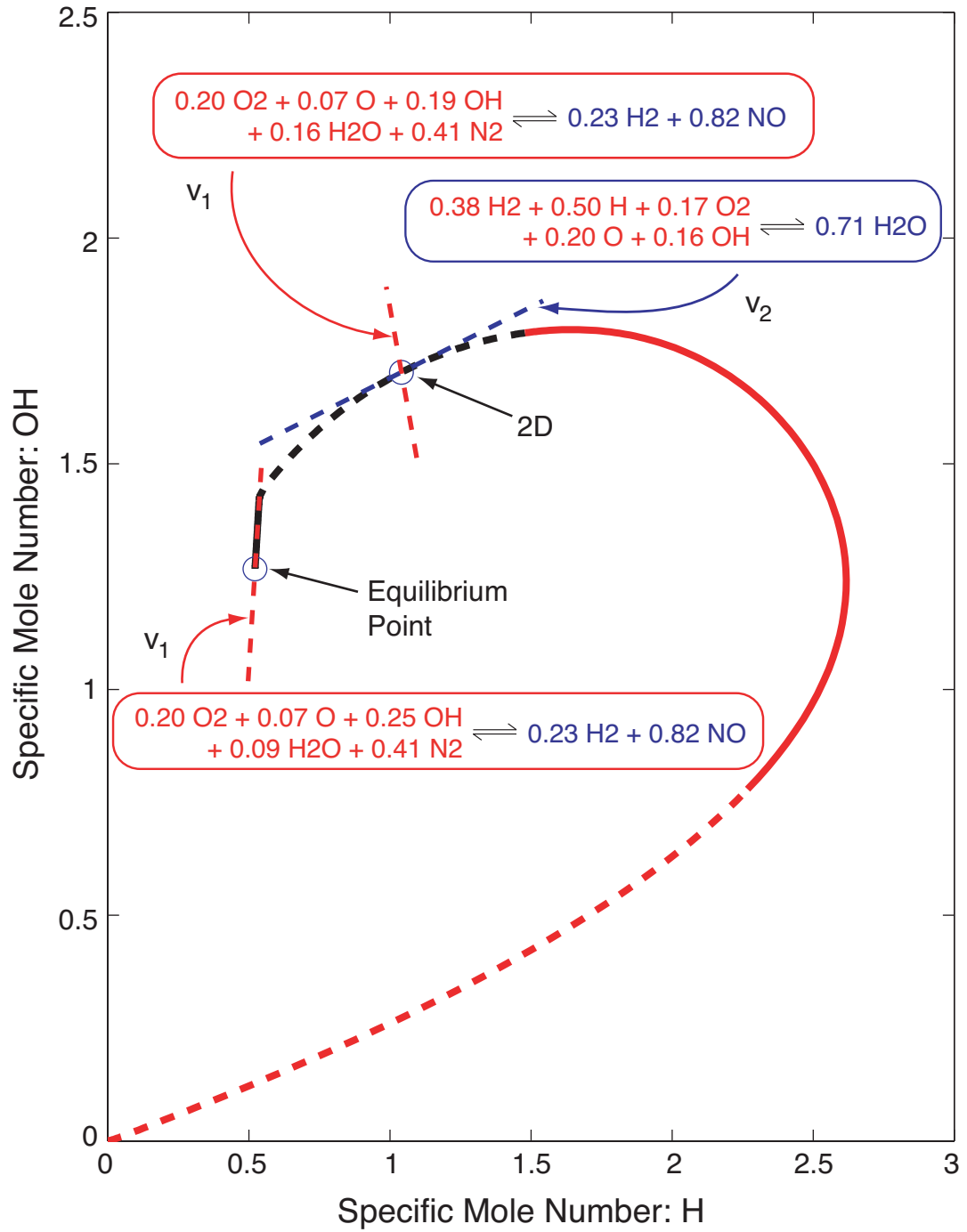
Figure 4.1: The *active modes* as determined by the ILDM. The reaction vector indicated at the equilibrium point is the slowest eigenvector of the Jacobian matrix. The two reaction vectors at the point marked "2D" are the slowest and the second slowest of the Jacobian. The full vectorial components are shown in Table 4.1.

λ	Point: EQ	Point: 2D	
	-2.2897e5	-6.8118e4	-1.2749e7
H_2	-0.2287	-0.2304	0.3808
H	0.0245	-0.0540	0.5021
O_2	0.2028	0.1994	0.1728
O	0.0677	0.0663	0.2002
OH	0.2490	0.1896	0.1582
HO_2	0.0007	0.0007	0.0024
H_2O_2	0.0001	0.0000	0.0005
H_2O	0.0916	0.1622	-0.7127
N	-0.0003	-0.0005	-0.0001
N_2	0.4078	0.4095	-0.0014
NO	-0.8153	-0.8185	0.0028
Ar	0.0000	0.0000	0.0000

Table 4.1: Eigenvalue and eigenvectors plotted in Figure 4.1.

numbers ϕ as coordinates is compatible with the ILDM computed using mass-fractions y. The mapping from ϕ to y is given in (2.15), rewritten in matrix form as

$$\phi = \mathsf{X}y , \quad \text{where}$$
$$\mathsf{X} = \text{diag}\{1/\mathcal{W}_i\}, \quad \mathsf{X} \in M_{n_s}. \tag{4.1}$$

The fact that the matrix X is constant (which makes the mapping from ϕ to y linear) means that the derivative of this mapping, needed for the push-forward operation, is also the premultiplication by the matrix X

$$f(\phi) = \mathsf{X}f(y) . \tag{4.2}$$

The Jacobian matrices $\mathsf{J}(\phi)$ and $\mathsf{J}(y)$ are related through

$$\mathsf{J}(\phi) = \mathsf{X}\mathsf{J}(y)\mathsf{X}^{-1} . \tag{4.3}$$

Because X is square and invertible (which is necessarily the case for the change of coordinates to be well-defined), the two Jacobians are said to be *similar* (see, for example Horn and Johnson, 1985). Using results from linear algebra, spectra of similar matrices are identical, hence

$$\sigma(\mathsf{J}(\phi)) = \sigma(\mathsf{J}(y)) . \tag{4.4}$$

In addition, if $\boldsymbol{v}(\boldsymbol{y})$ is an eigenvector corresponding to $\lambda \in \sigma(\mathsf{J}(\boldsymbol{y}))$ then $\mathsf{X}\boldsymbol{v}(\boldsymbol{y})$ is an eigenvector corresponding to the same eigenvalue λ: matrices satisfying (4.3), corresponding to a common eigenvalue, are related by

$$\boldsymbol{v}(\boldsymbol{\phi}) = \mathsf{X}\boldsymbol{v}(\boldsymbol{y}) \ . \tag{4.5}$$

Assume that a point $\boldsymbol{y}$ is in $\mathcal{M}^k$ computed using mass-fractions. Then, from the definition (3.7), $\boldsymbol{f}(\boldsymbol{y})$ is spanned by the k eigenvectors of $\mathsf{J}(\boldsymbol{y})$. Hence,

$$
\begin{aligned}
\boldsymbol{f}(\boldsymbol{y}) &\in \mathrm{span}\{\boldsymbol{v}_1(\boldsymbol{y}), \ldots, \boldsymbol{v}_k(\boldsymbol{y})\} \quad \text{and} \\
\mathsf{X}\boldsymbol{f}(\boldsymbol{y}) &\in \mathrm{span}\{\mathsf{X}\boldsymbol{v}_1(\boldsymbol{y}), \ldots, \mathsf{X}\boldsymbol{v}_k(\boldsymbol{y})\} \ .
\end{aligned}
\tag{4.6}
$$

It follows from the preceding linear algebra that $\boldsymbol{f}(\boldsymbol{\phi})$ is spanned by the k eigenvectors of $\mathsf{J}(\boldsymbol{\phi})$ corresponding to the same eigenvalues. Since the matrix X can be any invertible constant matrix, ILDMs are invariant under linear changes of coordinates.

However, because the ILDM is defined using the Jacobian matrix, which is non-tensorial (see, for example Frankel, 1997), it is not invariant under nonlinear, such as Cartesian to polar, coordinate transformation. An example is given below.

4.3 Example: Planar system with limit cycle

Consider the following vector field in the plane:

$$
\begin{aligned}
\dot{x} &= \quad y + kx(1 - x^2 - y^2) \\
\dot{y} &= \ -x + ky(1 - x^2 - y^2)
\end{aligned}
\tag{4.7}
$$

The system (4.7) has a limit cycle solution, which is the circle of radius one centered at the origin. The parameter k determines how rapidly trajectories approach the limit cycle. Also note that (4.7) has one (unstable) equilibrium point at the origin.

The phase portraits for $k = 5$ and $k = 20$ are shown in Figure 4.3. Initial conditions starting away from the limit cycle rapidly (depending on the parameter k) collapse onto the limit cycle. The limit cycle fits the description of the ILDM as a low-dimensional attractor.

(a) k = 5   (b) k = 20
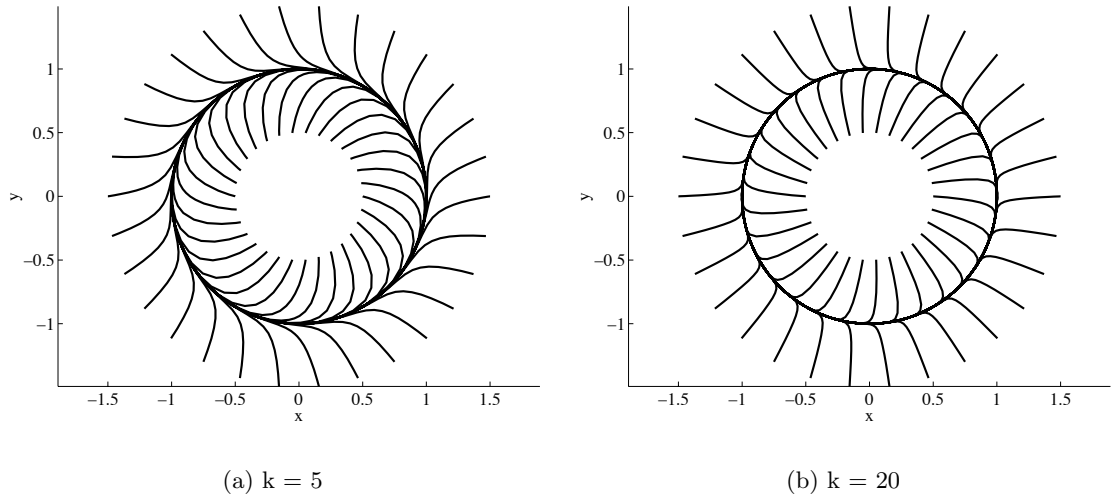
Figure 4.2: Phase portrait of (4.7).

The Jacobian matrix of the system (4.7) is

$$
\mathsf{J} = \begin{bmatrix} k(1 - x^2 - y^2) - 2kx^2 & 1 - 2kxy \\ -1 - 2kxy & k(1 - x^2 - y^2) - 2ky^2 \end{bmatrix} , \tag{4.8}
$$

and its two eigenvalues are

$$
\begin{aligned}
\lambda_1 &= -2k(x^2 + y^2) + k + \sqrt{k^2(x^2 + y^2)^2 - 1)} \quad \text{and} \\
\lambda_2 &= -2k(x^2 + y^2) + k + \sqrt{k^2(x^2 + y^2)^2 - 1)} .
\end{aligned}
\tag{4.9}
$$

These two eigenvalues are functions of the radial position only, independent of θ, when written in polar coordinates:

$$
\begin{aligned}
\lambda_1 &= -2kr^2 + k + \sqrt{k^2 r^4 - 1} \\
\lambda_2 &= -2kr^2 + k - \sqrt{k^2 r^4 - 1}
\end{aligned}
\tag{4.10}
$$

The eigenvalue λ_1 is clearly the slower (least negative) of the two eigenvalues. The two

eigenvectors are (in Cartesian and polar coordinates)

$$
\begin{aligned}
\boldsymbol{v}_1 &= [2kxy - 1, -k(x^2 - y^2) - \sqrt{k^2(x^2 + y^2)^2 - 1})] \\
&= [kr^2 \sin(2\theta) - 1, -kr^2 \cos(2\theta) - \sqrt{k^2 r^4 - 1}] \qquad \text{and} \\
\boldsymbol{v}_2 &= [2kxy - 1, -k(x^2 - y^2) + \sqrt{k^2(x^2 + y^2)^2 - 1})] \\
&= [kr^2 \sin(2\theta) - 1, -kr^2 \cos(2\theta) + \sqrt{k^2 r^4 - 1}] ,
\end{aligned}
\tag{4.11}
$$

where $\boldsymbol{v}_1$ is the slow eigenvector. Writing $\boldsymbol{v}_1 = [v_{11}, v_{12}]$, the one-dimensional ILDM is calculated by

$$
\det \begin{bmatrix} \dot{x} & \dot{y} \\ v_{11} & v_{12} \end{bmatrix} = 0 ,
\tag{4.12}
$$

which is statement of the linear dependence between the velocity vector and the slow eigenvector. Substituting (4.7) and (4.11) into the above to get

$$
\det \begin{bmatrix} y + kx(1 - x^2 - y^2) & -x + ky(1 - x^2 - y^2) \\ 2kxy - 1 & -k(x^2 - y^2) - \sqrt{k^2(x^2 + y^2)^2 - 1)} \end{bmatrix} = 0 .
\tag{4.13}
$$

Expanding the determinant and solving, the ILDM is found to be

$$
x^2 + y^2 = \frac{\sqrt{k^2 + 1}}{k} = \sqrt{1 + \frac{1}{k^2}} .
\tag{4.14}
$$

The ILDM is a circle of radius larger than 1 for all positive values of k. Since the limit cycle for this system is the circle of radius 1, the ILDM is clearly not an invariant set. However, in the limit as $k \to \infty$, the ILDM becomes the limit cycle solution.

4.3.1 Transformation to polar coordinates

Define $f : \{r : r > 0\} \times (0, 2\pi) \to \mathbf{R}^2$ by $f(r, \theta) = (r \cos(\theta), r \sin(\theta))$ (see, for example Spivak, 1965). The system (4.7) can be transformed into polar coordinates by writing

$$
P(x, y) = f^{-1} = (\theta(x, y), r(x, y)) ,
\tag{4.15}
$$

where

$$
\theta(x, y) = \begin{cases}
\arctan(y/x) & x > 0, y > 0, \\[6pt]
\pi + \arctan(y/x) & x < 0, \\[6pt]
2\pi + \arctan(y/x) & x > 0, y < 0, \\[6pt]
\pi/2 & x = 0, y > 0, \\[6pt]
3\pi/2 & x = 0, y < 0, \quad \text{and}
\end{cases}
\tag{4.16}
$$

$$
r(x, y) = \sqrt{x^2 + y^2} \ ,
$$

where the principal value of arctan is used.

The function P defined by (4.15) and (4.16) is the polar coordinate system. Vectors are then mapped according to

$$
\begin{pmatrix} \dot{\theta} \\ \dot{r} \end{pmatrix} = \begin{pmatrix} \partial\theta/\partial x & \partial\theta/\partial y \\ \partial r/\partial x & \partial r/\partial y \end{pmatrix} \begin{pmatrix} \dot{x} \\ \dot{y} \end{pmatrix} .
\tag{4.17}
$$

Carrying out the partial derivatives of (4.16),

$$
\begin{pmatrix} \dot{\theta} \\ \dot{r} \end{pmatrix} = \begin{pmatrix} -y/r^2 & x/r^2 \\ x/r & y/r \end{pmatrix} \begin{pmatrix} \dot{x} \\ \dot{y} \end{pmatrix} .
\tag{4.18}
$$

The original system (4.7) becomes, in polar coordinates:

$$
\dot{\theta} = -1
$$
$$
\dot{r} = kr(1 - r^2)
\tag{4.19}
$$

A partial phase-portrait for $k = 5$ is shown using $\theta - r$ coordinates in Figure 4.3. The figure contains trajectories using the same initial conditions as those used to produce Figure 4.2(a). The Jacobian matrix of the system (4.7) is

$$
\mathsf{J} = \begin{bmatrix} 0 & 0 \\ 0 & k(1 - r^2) - 2kr^2 \end{bmatrix} ,
\tag{4.20}
$$
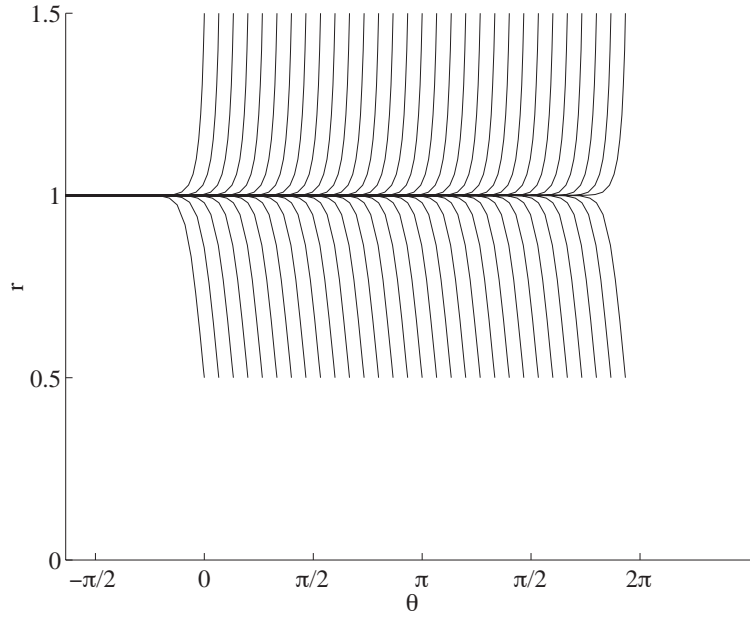
Figure 4.3: Phase portrait of (4.19), with $k = 5$

and the two eigenvalue-eigenvector pairs are

$$\begin{aligned} \lambda_1 &= 0 & \boldsymbol{v}_1 &= [1, 0] \quad \text{and} \\ \lambda_2 &= k - 3kr^2 & \boldsymbol{v}_2 &= [0, 1] \ . \end{aligned} \tag{4.21}$$

The one-dimensional ILDM for (4.19) is simply

$$r = 1 \ . \tag{4.22}$$

Thus, under this coordinate transformation, the ILDM gives the limit cycle solution for all positive values of k and this solution is invariant. The reason why the ILDM is different under this coordinate transformation is discussed next.

4.3.2 The Jacobian matrix and the covariant derivative

As was pointed out at the beginning of this chapter, the ILDM is expected to depend on the coordinate system chosen because the Jacobian matrix used in its definition is non-tensorial. When a curvilinear coordinate system is used, one must differentiate not only the components but also the non-constant basis vectors to obtain the derivatives of the components of a vector field,

Suppose V^i are the components of the vector field $\vec{V}$. Then the covariant derivative of $\vec{V}$, denoted by $\nabla\vec{V}$, has components

$$(\nabla\vec{V})^i{}_j = \frac{\partial V^i}{\partial x^j} + V^k\Gamma^i{}_{kj} \ . \tag{4.23}$$

The first term is the definition of the components of the Jacobian matrix J. The $\Gamma^i{}_{kj}$ in the second term are the Christoffel symbols. On a Cartesian basis, the basis vectors are constant and all the components of $\Gamma^i{}_{kj}$ vanish. On such a basis, the covariant derivative $\nabla\vec{V} = \mathsf{J}$.

Using (4.23), the covariant derivative of vector field in (4.19) is

$$\begin{aligned}
\nabla\vec{V}^i{}_j &= \mathsf{J} + V^k\Gamma^i{}_{kj} \\[6pt]
&= \begin{bmatrix} 0 & 0 \\ 0 & k(1-r^2)-2kr^2 \end{bmatrix} + \begin{bmatrix} k(1-r^2) & -1/r \\ r & 0 \end{bmatrix} \\[6pt]
&= \begin{bmatrix} k(1-r^2) & -1/r \\ r & k(1-r^2)-2kr^2 \end{bmatrix} \ .
\end{aligned} \tag{4.24}$$

The eigenvalues for the covariant derivative in (4.24) are

$$\begin{aligned}
\lambda_1 &= -2kr^2 + k + \sqrt{k^2r^4 - 1} \quad \text{and} \\
\lambda_2 &= -2kr^2 + k - \sqrt{k^2r^4 - 1}.
\end{aligned} \tag{4.25}$$

These are identical to the eigenvalues, shown in (4.10), of the Jacobian matrix for the original system in Cartesian coordinates. The eigenvectors (for $r > 0$) are

$$\begin{aligned}
\boldsymbol{v}_1 &= \begin{bmatrix} kr^2 + \sqrt{k^2r^4 - 1} & r \end{bmatrix} \quad \text{and} \\
\boldsymbol{v}_2 &= \begin{bmatrix} kr^2 - \sqrt{k^2r^4 - 1} & r \end{bmatrix}.
\end{aligned} \tag{4.26}$$

The ILDM for this system is identical to that of the original system in Cartesian coordinates. To be *intrinsic* in the sense of modern differential geometry is to be independent of the coordinate system. Using the covariant derivative in place of the Jacobian matrix renders the ILDM intrinsic.

However, computing the ILDM in polar coordinates using the Jacobian matrix leads not

only to a *different* solution, the reason for which was just addressed, but also to a *better* solution. The ILDM solution is the limit cycle. It will be seen from the following section that the limit cycle ($r = 1$) (see Figure 4.3) is the only trajectory that is *flat*.

A related result is discussed in Kaper and Kaper (2002), which says that the $\mathcal{O}(\epsilon^2)$ error between the asymptotic expansion of the ILDM and the true slow manifold $\mathcal{M}_\epsilon$ is proportional to the local curvature of $\mathcal{M}_0$, and that this error vanishes if and only if the curvature of $\mathcal{M}_0$ vanishes everywhere.

4.4 Curvature and arc-length reparameterization

Consider a point $\boldsymbol{y}$ that is on a one-dimensional ILDM $\mathcal{M}^1$. Then, by taking the time-derivative of the governing ODE (to get the acceleration),

$$\dot{\boldsymbol{y}} = \boldsymbol{f}(\boldsymbol{y}) \Longrightarrow \ddot{\boldsymbol{y}} = \mathsf{J}\boldsymbol{f}(\boldsymbol{y})$$
$$= \lambda_1 \boldsymbol{f}(\boldsymbol{y}), \ \ \forall \ \boldsymbol{y} \in \mathcal{M}^1 \ . \tag{4.27}$$

(4.27) shows that the velocity vector ($\dot{\boldsymbol{y}} = \boldsymbol{f}(\boldsymbol{y})$) and the acceleration vector ($\ddot{\boldsymbol{y}}$) are parallel when the velocity is spanned by an eigenvector of J. In other words, a trajectory $\boldsymbol{y}(t)$ that passes through $\boldsymbol{y} \in \mathcal{M}^1$ will be locally flat in the neighborhood of $\boldsymbol{y}$. From the theory of curves, the point at which the curvature vanishes is said to be a singular point of order 1 (do Carmo, 1976). This by no means suggests that the ILDM $\mathcal{M}^1$ is flat, but it implies that an $\mathcal{M}^1$ that is not globally flat cannot be invariant.

Because curvature is a property intrinsic to the curve and not its parameterization, one-dimensional ILDMs are expected to be invariant under arc-length reparameterization. In fact, it is possible to show that $\mathcal{M}^k$ is invariant under such a normalization. Consider the arc-length normalized system of ODE

$$\frac{d\boldsymbol{y}}{dt} = \boldsymbol{g}(\boldsymbol{y}), \quad \boldsymbol{g} = \frac{\boldsymbol{f}}{\|\boldsymbol{f}\|} \ . \tag{4.28}$$

The Jacobian matrix of $\boldsymbol{g}(\boldsymbol{y})$ is denoted by $\mathsf{J}^\star$. It is related to the Jacobian J of $\boldsymbol{f}(\boldsymbol{y})$ by

$$\mathsf{J}^\star = \frac{1}{\|\boldsymbol{f}\|} \left(\mathsf{I} - \boldsymbol{g} \otimes \boldsymbol{g} \right) \mathsf{J} \ , \tag{4.29}$$

where $\otimes$ is the dyadic product: $\boldsymbol{g} \otimes \boldsymbol{g} = \boldsymbol{g}\boldsymbol{g}^T$. The matrix $\mathsf{I} - \boldsymbol{g} \otimes \boldsymbol{g}$ in (4.29) is a *projector* from the phase space to $\boldsymbol{g}^\perp$. Denote this projector by

$$\mathsf{A} = (\mathsf{I} - \boldsymbol{g} \otimes \boldsymbol{g}) \ . \tag{4.30}$$

The matrix A is obviously symmetric, and A is idempotent (a projector), i.e.,

$$\mathsf{A}\mathsf{A} = \mathsf{A} \ . \tag{4.31}$$

The symmetry and idempotence of A and the fact that A maps the phase-space onto $\boldsymbol{g}^\perp$, mean that A is an orthogonal projector. This projector can also be computed using SVD: $\mathsf{A} = PP^T$, where $P = \text{null}\,(\boldsymbol{g}^T)$. It is interesting to note the similarity between the matrix A defined in (4.30) and a Householder matrix (Horn and Johnson, 1985). A Householder matrix, which has the form $\mathsf{I} - 2vv^T$ where the column vector v has unit 2-norm, is a reflection about the hyperplane $v^\perp$, whereas the matrix A is a projection onto $v^\perp$. Both A and the Householder matrix are known as rank-one modifications of the identity.

The properties of $\mathsf{J}^\star$ are now investigated with the ultimate goal of finding whether, and how, the ILDM $\mathcal{M}^k$ is changed by arc-length reparameterization. To simplify the analysis, redefine $\mathsf{J}^\star$ by using the condensed version of J defined in (3.8),

$$\mathsf{J}^\star = \frac{1}{\|\boldsymbol{f}\|} (\mathsf{I} - \boldsymbol{g} \otimes \boldsymbol{g}) \, \mathsf{J}^\flat \ , \tag{4.32}$$

where $\boldsymbol{g}^\flat = \mathsf{P}\boldsymbol{g}$. The vector $\boldsymbol{g}^\flat$, like $\boldsymbol{g}$ by definition, has unit two-norm because the matrix P is isometric for all admissible $\boldsymbol{f}(\boldsymbol{y})$ (and hence all admissible $\boldsymbol{g}(\boldsymbol{y})$). This change is only needed to avoid the computational difficulties concerning chemical systems. The $\flat$ superscripts in this section will be dropped when the context is clear. For systems that do not have conservation constraints, the Jacobian matrix J is invertible and the matrix P is any matrix similar to the identity (in particular, the identity itself), so all $\flat$ quantities are identical to their originals.

Consider now the matrix A, which is a projector from the full chemical state space of dimension n_s. Clearly, if A is a projector onto $\boldsymbol{g}^\perp$, then

$$\ker(\mathsf{A}) = \text{span}\{\boldsymbol{g}\} \ . \tag{4.33}$$

The kernel of $\mathsf{J}^\star$ is needed:

$$\mathsf{J}^\star \boldsymbol{y} = \boldsymbol{0}$$

$$\mathsf{A}\mathsf{J}\boldsymbol{y} = \boldsymbol{0} \tag{4.34}$$

$$\boldsymbol{y} \in \mathrm{span}\{\mathsf{J}^{-1}\boldsymbol{g}\}$$

From (4.34), the kernel of $\mathsf{J}^\star$ is the one-dimensional subspace spanned by the vector $\mathsf{J}^{-1}\boldsymbol{g}$. As mentioned above, the matrix J is, without loss of generality, assumed invertible (otherwise, the matrix $\mathsf{J}^\flat$ is substituted). In the next section, the relationship between the invariant eigenspaces of the two Jacobian matrices J and $\mathsf{J}^\star$ is discussed.

4.4.1 Invariant Subspaces of J and $\mathsf{J}^\star$

Consider an invariant eigenspace $\mathcal{S}$ of J that contains g (or equivalently, f),

$$\boldsymbol{y} \in \mathcal{S} \Longrightarrow \mathsf{J}\boldsymbol{y} \in \mathcal{S} \;\; \text{and} \;\; g \in \mathcal{S} \; . \tag{4.35}$$

The following notation will be used to emphasize the invariance of the eigenspace $\mathcal{S}$. Let

$$\mathsf{J}\mathcal{S} \subset \mathcal{S} \; , \tag{4.36}$$

where

$$\mathsf{J}\mathcal{S} \equiv \{\mathsf{J}\boldsymbol{y} : \boldsymbol{y} \in \mathcal{S}\} \; . \tag{4.37}$$

Now consider the action of $\mathsf{J}^\star$ on $\mathcal{S}$ using the notation defined in (4.36),

$$\mathsf{J}^\star \mathcal{S} = \left(\frac{1}{\|f\|}\mathsf{A}\mathsf{J}\right)\mathcal{S} \subset \mathsf{A}\mathcal{S} \; . \tag{4.38}$$

(4.38) holds because of the invariance of $\mathcal{S}$ under J. The constant multiplier $1/\|\boldsymbol{f}\|$ does not affect the eigenvalue-eigenvectors of any linear operators. Since $\mathcal{S}$ contains $\boldsymbol{g}$ by construction, an orthonormal basis can be constructed for $\mathcal{S}$ that uses $\boldsymbol{g}$ as its first basis vector. Assuming that $\mathcal{S}$ is m-dimensional,

$$\mathcal{S} = \mathrm{span}\{g, \boldsymbol{w}_2, \ldots, \boldsymbol{w}_m\} \; . \tag{4.39}$$

If a vector $\boldsymbol{y}$ in $\mathcal{S}$ is written using the basis in (4.39) then, in coordinates of this basis

$$\boldsymbol{y} = (y_1, \; y_2, \ldots, y_m)^T \quad \text{and}$$
$$\mathsf{A}\boldsymbol{y} = (0, \quad y_2, \ldots, y_m)^T.$$
$$(4.40)$$

(4.40) makes use of the fact that the second through last basis vectors $(\boldsymbol{w}_2, \ldots, \boldsymbol{w}_m)$ in (4.39) are all normal to $\boldsymbol{g}$ and hence in $\boldsymbol{g}^\perp$. As the matrix A is a projector to $\boldsymbol{g}^\perp$, the components with respect to $(\boldsymbol{w}_2, \ldots, \boldsymbol{w}_m)$ are therefore unchanged, and the first component is clearly nullified. The set $\mathsf{A}\mathcal{S}$ is therefore a hyperspace (i.e., has co-dimension 1) of $\mathcal{S}$:

$$\mathsf{A}\mathcal{S} \subset \mathcal{S} \tag{4.41}$$

Substituting (4.41) into (4.38), we obtain

$$\mathsf{J}^\star \mathcal{S} \subset \mathcal{S} . \tag{4.42}$$

In other words, the subspace $\mathcal{S}$ is invariant under the operator $\mathsf{J}^\star$. This can be summarized by the following:

> If an invariant subspace $\mathcal{S}$ of J contains g (equivalently, f), then $\mathcal{S}$ is also invariant under $\mathsf{J}^\star$.

This means that when $\boldsymbol{f}$ is spanned by k-eigenvectors of J, $\boldsymbol{g}$ will also be spanned by k-eigenvectors of $\mathsf{J}^\star$ (compare this to the definition of the ILDM given in the previous chapter). A k-dimensional ILDM is, however, spanned not by *any* k-eigenvectors, but the k-slowest eigenvectors of J. In other words, a connection between the eigenvalues of $\mathsf{J}^\star$ and those of J is needed. In particular, it is necessary to know that the k-eigenvectors of $\mathsf{J}^\star$ that spans $\mathcal{S}$ are also the slowest.

4.4.2 Spectra of J and $\mathsf{J}^\star$

Suppose V diagonalizes J and W diagonalizes $\mathsf{J}^\star$,

$$\mathsf{J} = \mathsf{V}\Lambda\mathsf{V}^{-1} \quad \text{and}$$
$$\mathsf{J}^\star = \mathsf{W}\Lambda^\star\mathsf{W}^{-1} ,$$
$$(4.43)$$

where V is a column partitioning of eigenvectors $\{v_1, \ldots, v_n\}$ of J and $W = \{w_1, \ldots, w_n\}$ is the counterpart for $J^\star$. Assume (sorting the eigenvectors if necessary) that the vector f (and hence g) is spanned by the first m eigenvectors of J. Then these m vectors form a basis for the invariant subspace $\mathcal{S}$ defined by (4.36). Since $\mathcal{S}$ is also invariant under $J^\star$ (the main result of the previous section), $\mathcal{S}$ is also spanned by $\{w_1, \ldots, w_m\}$ of W. It follows immediately that

$$w_i \in \text{span}\{v_1, \ldots, v_m\}, \quad i = 1..m \ . \tag{4.44}$$

Now consider the $m + 1$ dimensional invariant subspace spanned by the first m eigenvectors of J as before *plus* the jth-eigenvector, v_j, where $m < j \leq n$. Since this subspace is also invariant and includes g, the main result from the previous section continue to apply. This subspace will also be spanned by the first m and the $w_j = j^{\text{th}}$ (sorting if necessary) eigenvectors of $J^\star$. Thus

$$w_j \in \text{span}\{v_1, \ldots, v_m, v_j\}, \quad m < j \leq n \ . \tag{4.45}$$

Using (4.44) and (4.45), the eigenvectors of $J^\star$ written in the eigenbasis of J take the form

$$V^{-1}W = \begin{pmatrix} \overset{m}{A_{11}} & \overset{\leftarrow \ n-m \ \rightarrow}{-\quad A_{12} \quad -} \\ & a_{m+1} \\ 0 & \quad \ddots \\ & \quad\quad a_n \end{pmatrix}, \tag{4.46}$$

where the submatrices $A_{11} \in M_m$ and $A_{12} \in M_{m,n-m}$ are dense and the lower-right subblock is diagonal. The inverse of (4.46) then takes the form

$$W^{-1}V = \begin{pmatrix} B_{11} & -\quad B_{12} \quad - \\ & b_{m+1} \\ 0 & \quad \ddots \\ & \quad\quad b_n \end{pmatrix}, \tag{4.47}$$

where $B_{11} = A_{11}^{-1}$ and $b_j = a_j^{-1}$. The next step is to show that the matrix W partially

diagonalizes J.

$$
\begin{aligned}
W^{-1}JW &= W^{-1}\left(V\Lambda V^{-1}\right)W \\
&= \left(W^{-1}V\right)\Lambda\left(V^{-1}W\right)
\end{aligned}
\tag{4.48}
$$

Using the structure of the matrices $W^{-1}V$ and $V^{-1}W$ from (4.47) and (4.46), the matrix product in (4.48) will take the form

$$
W^{-1}JW = \left(\begin{array}{c|ccc}
C_{11} & - & C_{12} & - \\
\hline
| & \lambda_{m+1} & & \\
0 & & \ddots & \\
| & & & \lambda_n
\end{array}\right) ,
\tag{4.49}
$$

where $C_{11} \in M_m$ and $C_{12} \in M_{m,n-m}$ are dense and the lower-right subblock is a diagonal matrix of the eigenvalues.

It will now be shown that W also partially diagonalizes the projector A defined in (4.30). Noting that premultiplication by A (in the construction of $J^\star$) introduces one zero-eigenvalue, denote the associated eigenvector by $\boldsymbol{w}_1$. It follows from (4.34) that $\boldsymbol{w}_1 = J^{-1}\boldsymbol{g}$. Now, all eigenvectors of $J^\star$ with non-vanishing eigenvalues are necessarily on $\boldsymbol{g}^\perp$ because of the projector A:

$$
A J\boldsymbol{w}_j = \lambda_j^\star \boldsymbol{w}_j \neq \boldsymbol{0} \implies \boldsymbol{w}_j \in \boldsymbol{g}^\perp .
\tag{4.50}
$$

Because of (4.50), all eigenvectors $\boldsymbol{w}_j$ that correspond to nonvanishing eigenvalues are unchanged by A,

$$
A\boldsymbol{w}_j = \boldsymbol{w}_j ,
\tag{4.51}
$$

and from the above,

$$
W^{-1}\left(AW\right) = \left(\begin{array}{ccc} & W^{-1} & \end{array}\right)\left(\begin{array}{c|ccc} A\boldsymbol{w}_1 & \boldsymbol{w}_2, \ldots, \boldsymbol{w}_n \end{array}\right) .
\tag{4.52}
$$

Except for the first column, the matrix product in (4.52) is the identity matrix. Now, using the result from (4.41) and recalling the invariant subspace $\mathcal{S} = \text{span}\{\boldsymbol{w}_1, \ldots, \boldsymbol{w}_m\}$, $A\boldsymbol{w}_1$ is in the hypersurface of $\mathcal{S}$ spanned by $\{\boldsymbol{w}_2, \ldots, \boldsymbol{w}_m\}$. (4.52) therefore takes the very simple

form

$$
\mathsf{W}^{-1}\mathsf{A}\mathsf{W} =
\left(
\begin{array}{c|ccccc}
0 & & & & & \\
\hline
\times & 1 & & & & \\
\vdots & & 1 & & & \\
\times & & & 1 & & \\
\hline
| & & & & \ddots & \\
0 & & & & & \\
| & & & & & 1
\end{array}
\right) .
\tag{4.53}
$$

Rearranging (4.43), and using (4.49) and (4.53),

$$
\Lambda^\star = \mathsf{W}^{-1}\mathsf{J}^\star\mathsf{W} \quad \text{and}
$$

$$
\begin{aligned}
\|f\|\Lambda^\star &= \mathsf{W}^{-1}\mathsf{A}\mathsf{J}\mathsf{W} \\
&= \left(\mathsf{W}^{-1}\mathsf{A}\mathsf{W}\right)\left(\mathsf{W}^{-1}\mathsf{J}\mathsf{W}\right) \\
&= \mathrm{diag}\{0, \lambda_1^\star, \ldots, \lambda_m^\star, \lambda_{m+1}, \ldots, \lambda_n\} .
\end{aligned}
\tag{4.54}
$$

(4.54) illustrates how the spectra of $\mathsf{J}^\star$ and J are related:

> The eigenvalues of J associated with eigenvectors not needed to span f (or g) will be unchanged when J is premultiplied by A. Among the eigenvalues that are changed, one will be set to exactly zero.

With further algebraic manipulations, it can be shown that the $(m-1)$ undetermined eigenvalues of $\mathsf{J}^\star$ are linear (but non-convex) combinations of the m eigenvalues of J associated with the spanning eigenvectors of $\mathcal{S}$. Thus, given a big enough gap between λ_m and λ_{m+1}, the slowest m eigenvalues of J will continue to be the slowest for $\mathsf{J}^\star$.

4.4.3   Algorithm demonstration

The constant volume trajectory of Mixture A (Table 3.1), whose ILDM dimension is computed from §3.3, is shown in Figure 4.4. The point 1D represents a point on the trajectory that belongs to $\mathcal{M}^1$, and the points marked 2D and 3D are chosen similarly.

Taking care of the zero eigenvalues using the projector P as shown in (3.8), the sorted eigenvalues of J and $\mathsf{J}^\star$ for the three points marked in Figure 4.4 are tabulated in Table 4.2.
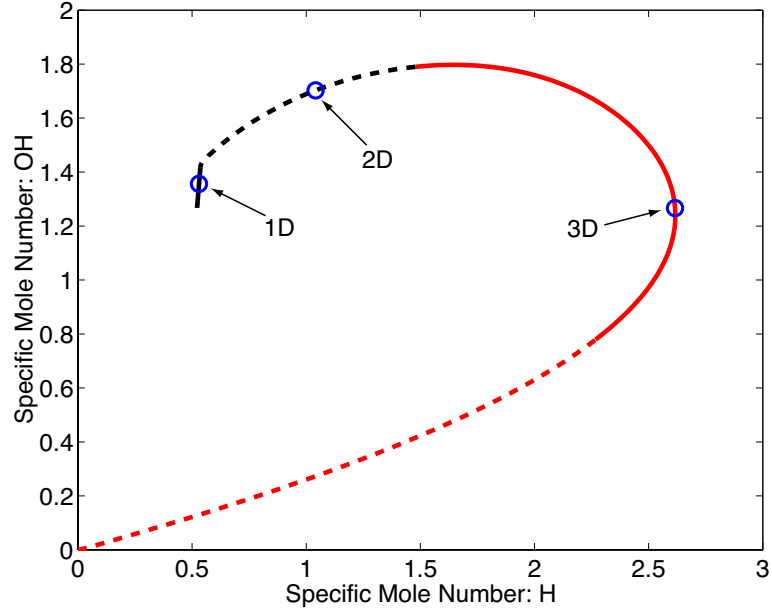
Figure 4.4: Constant volume trajectory of Mixture A (Table 3.1), with points 1D on $\mathcal{M}^1$, 2D on $\mathcal{M}^2$ and 3D on $\mathcal{M}^3$ shown.

Point: 1D		Point: 2D		Point: 3D	
$\sigma(\mathsf{J})$	$\sigma(\mathsf{J}^\star)$	$\sigma(\mathsf{J})$	$\sigma(\mathsf{J}^\star)$	$\sigma(\mathsf{J})$	$\sigma(\mathsf{J}^\star)$
-2.827e10	-2.827e10	-1.663e10	-1.663e10	-2.057e9	-2.057e9
-2.100e9	-2.100e9	-1.940e9	-1.940e9	-1.616e9	-1.616e9
-1.246e9	-1.246e9	-1.160e9	-1.160e9	-1.060e9	-1.060e9
-1.193e9	-1.193e9	-1.114e9	-1.115e9	-5.621e8	-5.542e8
-3.065e8	-3.065e8	-3.389e8	-3.389e8	-2.727e8	-2.727e8
-4.070e7	-4.070e7	-7.122e7	-7.135e7	-6.449e7	-4.054e7
-4.305e5	-4.306e5	-1.275e7	-4.829e4	-3.477e7	-9.413e2
-1.806e5	0	-6.818e4	0	-3.658e3	0

Table 4.2: The sorted eigenvalue spectra for J and $\mathsf{J}^\star$.

Comparing the eigenvalues of J and those of $\mathsf{J}^\star$ from Table 4.2, it can be seen that, for the point marked "1D", only the last (least negative) eigenvalues between the two sets are significantly different. Similarly, for the points marked "2D" (or "3D"), only the last 2 (or 3) eigenvalues are significantly different. Just as the Grammian procedure in §3.3 depends on some parameters ϵ, this algorithm requires an analogous tolerance in comparing eigenvalues for equality.

4.5 1D ILDM for 2D dynamical systems

For systems in two dimensions, a one-dimensional ILDM is easy to find using the result from the preceding sections. This is irrelevant for chemical mechanisms, but is illustrative in understanding the method.

Consider the ODE system

$$\dot{x}_1 = f_1(x_1, x_2)$$
$$\dot{x}_2 = f_2(x_1, x_2) \ . \tag{4.55}$$

Let $\boldsymbol{x} = (x_1, x_2)^T$ and let $\boldsymbol{f} = (f_1, f_2)$. The corresponding unit-speed system is

$$\dot{x}_1 = g_1(x_1, x_2)$$
$$\dot{x}_2 = g_2(x_1, x_2) \ , \tag{4.56}$$

where $\boldsymbol{g} = \boldsymbol{f}/\|\boldsymbol{f}\|$. Similarly, let $\boldsymbol{g} = (g_1, g_2)$. Denote the two Jacobian matrices as

$$\mathsf{J} = \begin{pmatrix} \frac{\partial f_1}{\partial x_1} & \frac{\partial f_1}{\partial x_2} \\ \frac{\partial f_2}{\partial x_1} & \frac{\partial f_2}{\partial x_2} \end{pmatrix} , \quad \text{and } \mathsf{J}^\star = \begin{pmatrix} \frac{\partial g_1}{\partial x_1} & \frac{\partial g_1}{\partial x_2} \\ \frac{\partial g_2}{\partial x_1} & \frac{\partial g_2}{\partial x_2} \end{pmatrix} \ . \tag{4.57}$$

Let the curve $\boldsymbol{x}(s)$ be a solution to the unit-speed system in (4.56). By definition, $\langle \dot{\boldsymbol{x}}(s), \dot{\boldsymbol{x}}(s) \rangle = \langle \boldsymbol{g}, \boldsymbol{g} \rangle = 1$, where the angle brackets denote the standard inner product. Taking the time derivative,

$$\langle \ddot{\boldsymbol{x}}(s), \dot{\boldsymbol{x}}(s) \rangle = 0 \ . \tag{4.58}$$

Using results from the previous section, $\mathsf{J}^\star$ will have one zero-eigenvalue. Writing the two eigenvalue-eigenvector pairs of $\mathsf{J}^\star$ as $(\lambda_1^\star = 0, \boldsymbol{w}_1)$ and $(\lambda_2^\star, \boldsymbol{w}_2)$, it follows (from writing $\boldsymbol{g}$ in the eigenbasis) that the acceleration vector $\ddot{\boldsymbol{x}} = \mathsf{J}^\star \boldsymbol{g}$ is parallel to $\boldsymbol{w}_2$. Since the acceleration vector is normal to the velocity vector (from (4.58)), a point $\boldsymbol{x}(s)$ can be on $\mathcal{M}^1$ if and only if the two eigenvectors $\boldsymbol{w}_1$ and $\boldsymbol{w}_2$ are orthogonal. Orthogonality of eigenvectors implies the symmetry of $\mathsf{J}^\star$,

$$\boldsymbol{x} \in \mathcal{M}^1 \iff \frac{\partial g_2(\boldsymbol{x})}{\partial x_1} = \frac{\partial g_1(\boldsymbol{x})}{\partial x_2} \ . \tag{4.59}$$
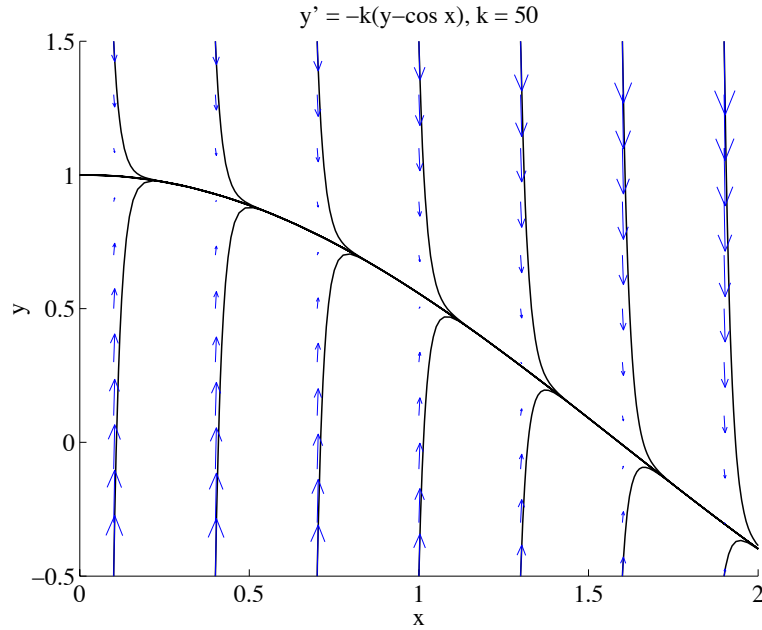
Figure 4.5: Vector field and phase portrait of (4.61), with $k = 50$.

4.6 Example: A simple planar dynamical system

Consider the following ODE, adapted slightly from Hairer (1996):

$$\frac{dy}{dx} = -k(y - \cos x) \tag{4.60}$$

(4.60) can be rewritten as the following system of homogeneous ODEs:

$$\dot{x} = 1$$
$$\dot{y} = -k(y - \cos x) \tag{4.61}$$

Figure 4.5 shows a phase portrait of (4.61) superimposed on its vector field. (4.61) can be rewritten in the standard form of the singular perturbation model[*] by writing $\epsilon = 1/k$:

$$\dot{x} = 1$$
$$\epsilon \dot{y} = -(y - \cos x) \tag{4.62}$$

---

[*] See Holmes (1995) and Sell and You (2002) for a general introduction to the singular perturbation model, and Rhodes et al. (1999) and Kaper and Kaper (2002) for its application to ILDM based reduction methodologies.

When $\epsilon \to 0$, the second equation of (4.62) becomes a constraint of the system:

$$0 = y - \cos x \tag{4.63}$$

Using the terminology of Rhodes et al. (1999), (4.61) defines the slow manifold $\mathcal{M}_0$. The exact solution of (4.60) is given by

$$y = \frac{k^2}{k^2 + 1} \cos x + \frac{k}{k^2 + 1} \sin x + C \exp(-kx) , \tag{4.64}$$

where C is determined from the initial conditions. The solution of (4.64) contains an exponential decay that depends on the given initial condition (IC) as well as a part that doesn't. The IC independent portion is our exact slow manifold onto which all trajectories evolve. Making the substitution $\epsilon = 1/k$ yields

$$\mathcal{M}_\epsilon : y = \frac{1}{1 + \epsilon^2} (\cos x + \epsilon \sin x) . \tag{4.65}$$

Using the machinery developed in §4.5, (4.59) in particular, the one-dimensional ILDM $\mathcal{M}^1$ for (4.61) is found to be

$$\mathcal{M}^1 : y = \cos x + \epsilon \sin x . \tag{4.66}$$

It is clear that as $\epsilon \to 0$, the slow manifold $\mathcal{M}_\epsilon$, the one-dimensional ILDM $\mathcal{M}^1$ and the manifold $\mathcal{M}_0$ are equivalent. When ϵ is small but non-zero, it is seen that the $\mathcal{M}^1$ given by (4.66) is a significantly better approximation of $\mathcal{M}_\epsilon$ than $\mathcal{M}_0$. This is shown graphically in Figure 4.6 for $k = 20$.

Using the curvature interpretation of the ILDM developed in this section, an estimate of how $\mathcal{M}^1$ deviates from $\mathcal{M}_\epsilon$ can be obtained without any computation. Since $\mathcal{M}^1$ represents the locus of singular points of order 1, the ILDM lies on the side where the trajectories have opposite curvature to $\mathcal{M}_\epsilon$. In other words, if $\mathcal{M}_\epsilon$ is locally concave down, then $\mathcal{M}^1$ will lie above $\mathcal{M}_\epsilon$, and vice versa. This is shown in Figure 4.7, where the error of the ILDM is magnified by 50 times.

The exact difference between $\mathcal{M}^1$ and $\mathcal{M}_\epsilon$ is

$$\mathcal{M}^1 - \mathcal{M}_\epsilon : y = \frac{\epsilon^2}{1 + \epsilon^2} (\cos x + \epsilon \sin x) . \tag{4.67}$$
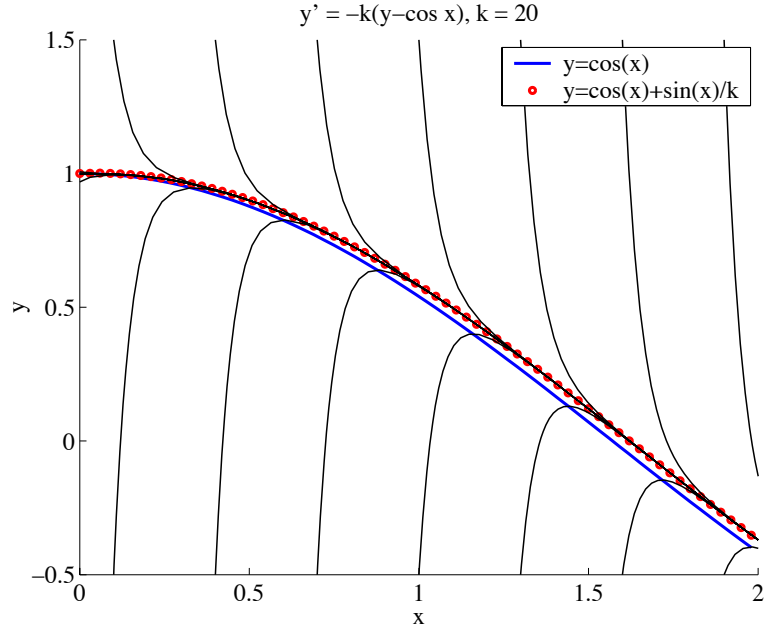
Figure 4.6: ILDM of (4.66) and $\mathcal{M}_0$ of (4.63), plotted on top of the phase portrait of (4.61).
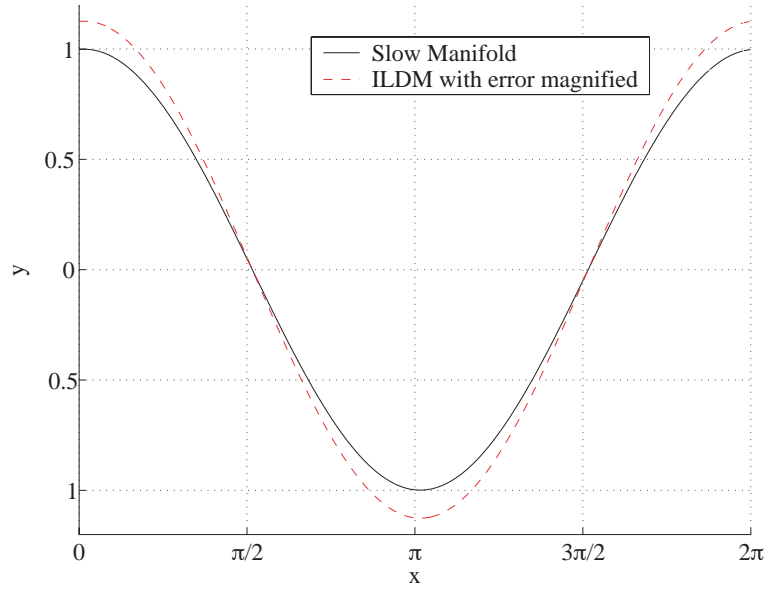

Figure 4.7: The ILDM $\mathcal{M}^1$ for (4.61), plotted with error between the ILDM and the true slow manifold magnified 50 times for $k = 20$.

Scaling the error by $\mathcal{M}_\epsilon$, (4.67) becomes

$$\frac{\mathcal{M}^1 - \mathcal{M}_\epsilon}{\mathcal{M}_\epsilon} = \epsilon^2 \ . \tag{4.68}$$

4.7   Remarks on the noninvariance of the ILDM

Since the original paper Maas and Pope (1992b) was published, much work has been done to investigate the foundations of the algorithm. For example, we now know that the ILDM only approximates the invariant manifold, in spite of the claims made in Rhodes et al. (1999). This is easily established, as almost any model dynamical systems with non-flat invariant manifolds are counter-examples.

In addition, Kaper and Kaper (2002) showed that the ILDM approximates the asymptotic expansion of the invariant manifold $\mathcal{M}_\epsilon$ to second order, and that the error is proportional to the local curvature of $\mathcal{M}_0$. An example illustrating this is given in §4.6.

In chemically reactive systems, however, we have found that this error is small because the parameter ϵ is a function of the spectral gap. It is both an observation and an assumption that we will make throughout. This assumption can be easily checked, for example, by examination of Figure 3.3. We see that the different Gram determinants reached zero (to within some very small tolerance) and remained zero.

When the invariance assumption is violated, such as for the limit-cycle systems of Figure 4.2(a) and Figure 4.2(b), the concept of ILDM dimension is no longer useful. Because the ILDM $\mathcal{M}^1$ for the system is a circle whose radius is outside the limit-cycle, we know that the Gram determinant Γ^1 along a trajectory starting from inside the circle will never reach zero. Similarly, Γ^1 along a trajectory starting from outside will reach zero and then becomes finite as it goes through the ILDM.

Chapter 5

ILDM via Congruences

The definition of the ILDM in (3.5) provides, by rewriting it in explicit form, a direct method of computing $\mathcal{M}^k$ in terms of the inverse set mapping:

$$\mathcal{M}^k = \left(\hat{\mathsf{V}}_f \boldsymbol{f}\right)^{-1}(\boldsymbol{0}) \tag{5.1}$$

It is important to state what is meant by a (numerical) solution of (5.1). Generally, a solution is comprised of a set of points S in the original n_s-dimensional chemical state space, each of which satisfies (3.5) to within some tolerance

$$\left\|\hat{\mathsf{V}}_f \boldsymbol{f}(\boldsymbol{y})\right\| \leq \epsilon, \ \ \forall \ \boldsymbol{y} \in \mathsf{S} \ . \tag{5.2}$$

Numerical schemes based on continuation methods are typically used to solve (5.1), which becomes very difficult for $k > 1$.

On the other hand, armed with the tools from the previous chapters for computing the ILDM dimension, it is possible to take an indirect approach. Redefine the set S as

$$\mathsf{S} = \{\boldsymbol{y} \in \mathbf{R}^{n_s} : \Gamma^k \boldsymbol{y} \leq \epsilon\} \ . \tag{5.3}$$

Given a trajectory $\boldsymbol{y}(t)$ satisfying (2.18a), subject to some initial conditions $\boldsymbol{y}_o$, compute the time of arrival (t^k) of $\boldsymbol{y}(t)$ to $\mathcal{M}^k$ as defined in (3.25). Together with (5.3),

$$\boldsymbol{y}(t) \in \mathsf{S}, \ \ \forall \ t \geq t^k \ . \tag{5.4}$$

In other words, $\mathcal{M}^k$ is numerically computed (i.e., the set S is populated) by solving (2.18a)

Mixture ID:	*Mixture B*
Composition	$2H_2$–O_2–$7Ar$
Density (g/cc)	0.5e-3
Internal Energy (ergs/g)	8e9
Reaction Mechanism	Maas-Warnatz

Table 5.1: Properties and reaction mechanism for Mixture B.

subject to different initial conditions. This "filling of a manifold" by curves is called a congruence (Schutz, 1980).

5.1   Example: Construction of a One-Dimensional ILDM

The procedure described in the previous section is used to compute the one-dimensional ILDM for the detonation problem studied in Rastigejev et al. (2000) (also see §2.5.3 of Singh, 2003). The conditions, denoted by Mixture B, are indicated in Table 5.1. The Maas-Warnatz mechanism (see Table 1.1) contains 9 species (including the inert species Ar) and 37 irreversible reactions. The CV system is represented by

$$\frac{d\boldsymbol{y}}{dt} = \boldsymbol{f}(\boldsymbol{y}; \rho, e) \ . \tag{2.18a}$$

The one dimensional manifold $\mathcal{M}^1$ is unique in its topological simplicity: it is a curve through the equilibrium point in chemical state-space, and the equilibrium point divides the curve into two disconnected components. A one-dimensional manifold can thus be completely filled by two properly chosen trajectories.

Using a point $\boldsymbol{y}_o \in \mathcal{M}^1$ as initial data to (2.18a), the trajectory that results is a part of $\mathcal{M}^1$, starting at $\boldsymbol{y}_o$ and terminating at equilibrium. The next procedure determines, in the linear approximation, the two initial data (roughly speaking, one on each side of equilibrium), that maximize the extent of the solution to $\mathcal{M}^1$.

First, compute the one-dimensional slow eigenspace of the system, which is an affine linear space centered at the equilibrium point spanned by the slowest eigenvector. This is shown in Figure 5.1. The meaning of this eigenspace, which will be denoted by L^1 for convenience, is elementary (see for example Arnold, 1973, Hirsch and Smale, 1974) and will not be elaborated upon. It can be shown that, in the neighborhood of the equilibrium point,
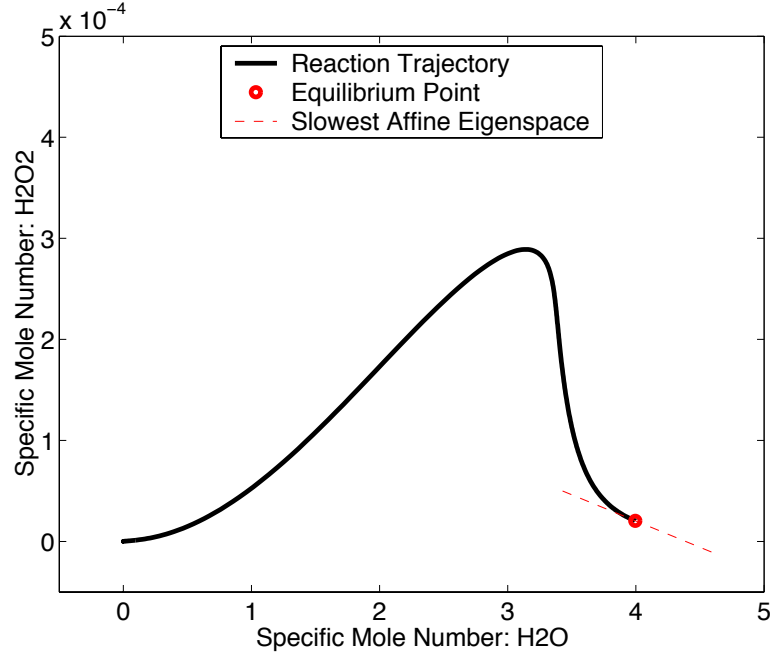
Figure 5.1: CV reaction trajectory, equilibrium point and the slowest linear eigenspace.

$\mathcal{M}^1$ is tangent to L^1. At equilibrium, denoted by $\boldsymbol{y}_\infty$,

$$f(\boldsymbol{y}_\infty) = \boldsymbol{0} \ . \tag{5.5}$$

The eigenvalue decomposition of the Jacobian J takes the form

$$\mathsf{J}(\boldsymbol{y}_\infty) = \begin{pmatrix} | & | \\ v_1 & \mathsf{V}_f \\ | & | \end{pmatrix} \begin{pmatrix} \lambda_1 & 0 \\ 0 & \Lambda_f \end{pmatrix} \begin{pmatrix} - \ \hat{v}_1 \ - \\ - \ \hat{\mathsf{V}}_f \ - \end{pmatrix} \ , \tag{5.6}$$

where the slow eigenspace $\mathsf{V}_s = v_1$ and $\hat{\mathsf{V}}_s = \hat{v}_1$ are the left and right eigenvector associated with the slowest eigenvalue, respectively. Since $\boldsymbol{y}_\infty$ satisfies $\hat{\mathsf{V}}_f \boldsymbol{f}(\boldsymbol{y}) = \boldsymbol{0}$ trivially from (5.5), the equilibrium point is on $\mathcal{M}^k$ for all values of k. Because the ILDM is defined as a preimage (5.1) of the function $\hat{\mathsf{V}}_f \boldsymbol{f}$, the kernel of the derivative of this function at $\boldsymbol{y}_\infty$ gives the tangent space of $\mathcal{M}^1$ (see Guillemin and Pollack, 1974):

$$\begin{aligned} d(\hat{\mathsf{V}}_f \cdot \boldsymbol{f}) &= d\hat{\mathsf{V}}_f \cdot \boldsymbol{f} + \hat{\mathsf{V}}_f \cdot df_{\boldsymbol{y}} \\ &= \hat{\mathsf{V}}_f \mathsf{J} \end{aligned} \tag{5.7}$$

The derivative at equilibrium is particularly simple, because the directional derivative

$d\hat{V}_f \cdot f$ vanishes as f vanishes. Using (5.6),

$$\hat{V}_f = \Lambda_f \hat{V}_f \ . \tag{5.8}$$

The tangent to $\mathcal{M}^1$ can therefore be simplified to

$$\ker d(\hat{V}_f \cdot f) = \ker(\hat{V}_f \mathsf{J}) \ . \tag{5.9}$$

But from (5.6), this kernel can be found easily:

$$\begin{pmatrix} - \ \hat{v}_1 \ - \\ - \ \hat{V}_f \ - \end{pmatrix} \Big(\mathsf{J}(\boldsymbol{y}_\infty) \Big) \begin{pmatrix} | \\ v_1 \\ | \end{pmatrix} = \begin{pmatrix} \lambda_1 \\ 0 \end{pmatrix} \tag{5.10}$$

Hence, $\mathcal{M}^1$ is tangent to the slowest eigenvector at equilibrium,

$$\ker d(\hat{V}_f \cdot \boldsymbol{f}) = \mathrm{span}\{v_1\} \ . \tag{5.11}$$

The more general result that the tangent at the equilibrium point to $\mathcal{M}^k$ is the k-dimensional slow eigenspace spanned by eigenvectors at equilibrium is obtained in exactly the same manner. This result is used in the next section.

The next step is to extend L^1 as far as possible. In addition to the elemental constraint (2.21) already described, the chemical state-space is further limited by the "positivity constraint" that all components of $\boldsymbol{y}$ need to be positive,

$$y_i \geq 0, \ \ \forall \ i = 1..n_s \ . \tag{5.12}$$

As a result of (2.21) and (5.12), the admissible chemical state-space is compact (in fact, a convex-polytope) (Coxeter, 1973). The determination of the maximal extent of L^1 becomes a problem in linear programming, and convexity allows the solution to be determined simply by ray-tracing:

$$\begin{aligned} \gamma_r = \max \gamma : \boldsymbol{y} = \boldsymbol{y}_\infty + \gamma v_1, \quad y_i \geq 0 \ \forall \ i = 1..n_s \\ \gamma_l = \max \gamma : \boldsymbol{y} = \boldsymbol{y}_\infty - \gamma v_1, \quad y_i \geq 0 \ \forall \ i = 1..n_s \end{aligned} \tag{5.13}$$

In one dimension, the linear programming problem is akin to extending L^1 until one of the n-inequalities in (5.12) becomes an equality. The range of validity for the thermo-
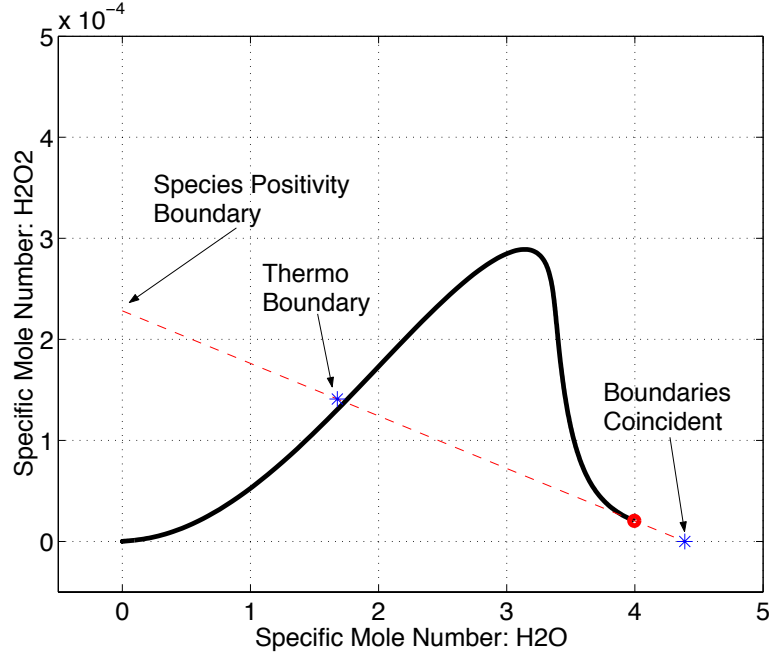
Figure 5.2: The dashed line represents the maximal extent of the slowest linear eigenspace subjected to positivity constraint. Asterisks indicate the boundary with the additional constraint imposed by (5.14).

dynamic data imposes an additional constraint: at a given value of density and internal energy,

$$T_{\min} \leq T(\boldsymbol{y}; \rho, e) \leq T_{\max} . \tag{5.14}$$

The maximal linear eigenspace as well as its thermodynamic boundary, determined by (5.14), is illustrated in Figure 5.2.

The two points representing the thermodynamic boundary of the one-dimensional eigenspace are used as initial data to (2.18a). By using the time of arrival concept from the previous section, each resulting trajectory can be partitioned into two sets: before reaching $\mathcal{M}^1$ and after.

By truncating the initial portion of the trajectory, the piece that lies entirely in $\mathcal{M}^1$ is obtained. The numerical solution of $\mathcal{M}^1$ is the union of the truncated trajectories from the two boundary points. That is illustrated in Figure 5.3. This figure also clearly demonstrates that the original trajectory, also shown in Figure 5.1 and Figure 5.2, is attracted onto $\mathcal{M}^1$ well before reaching the equilibrium position.
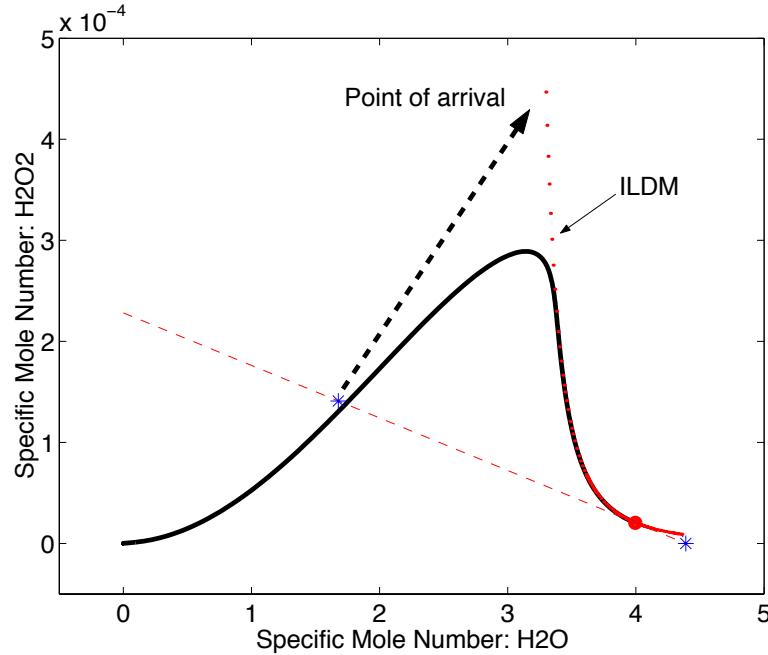
Figure 5.3: The dotted line represents the numerical solution to the one-dimensional ILDM. The deleted portion of the trajectory on the left, corresponding to $\boldsymbol{y}(t < t_1)$, is replaced by an arrow from initial data (asterisk) to the point of arrival.

5.2 Example: Construction of Higher Dimensional ILDM

Computations of higher-dimensional ILDMs proceed in exactly the same manner as in the previous section. First the linear programming problem for the maximal linear eigenspace is solved, and its boundary is shrunken according to (5.14). Points on this boundary (the thermodynamic boundary) are evolved and the initial portion of each trajectory is truncated leaving behind the portion that lies entirely in $\mathcal{M}^k$. When a two-dimensional ILDM is sought, the manifold boundary is one-dimensional and is topologically a closed loop. This procedure is applied to Mixture A in Table 3.1, and the result is shown in Figure 5.4.

This algorithm can be parallelized in the obvious manner by means of domain decomposition of the thermodynamic boundary. In higher dimensions, even though the algorithm remains the same, the amount of work to be done becomes geometrically greater. For a three-dimensional ILDM, the maximal affine eigenspace is a three-dimensional convex polytope embedded in the full configuration space. Its boundary is a two-dimensional surface that needs to be sampled, tessellated and meshed. Such a boundary is shown in Figure 5.5.
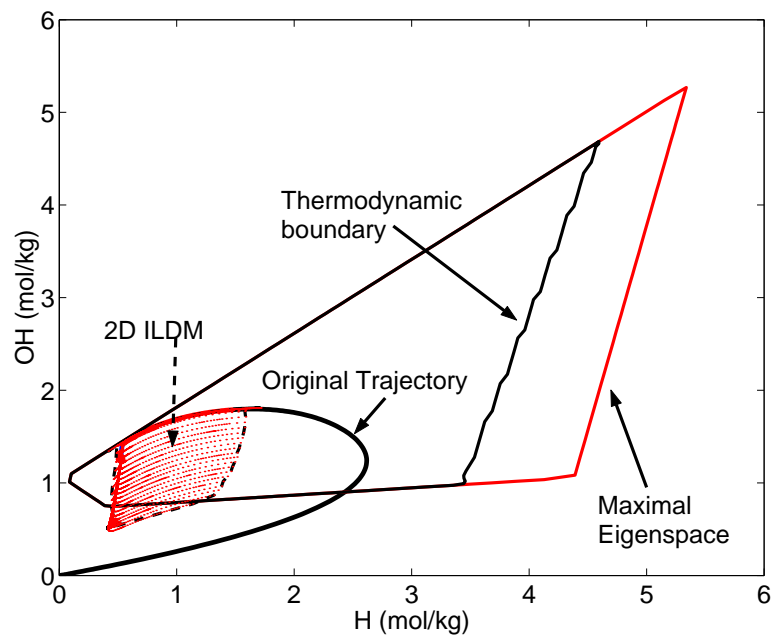
Figure 5.4: An illustration of the step involved in the construction of a two-dimensional ILDM. Mixture composition is shown in Table 3.1.
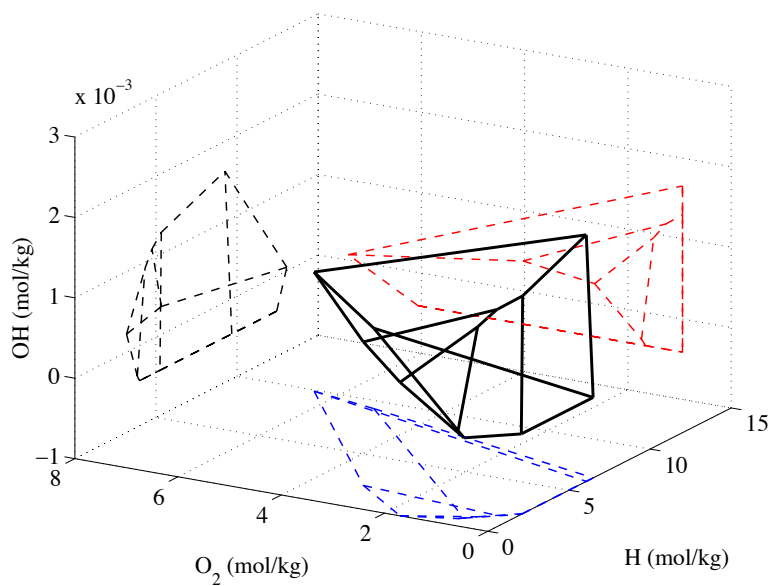
Figure 5.5: The convex-polytope representing the three-dimensional slow eigenspace is shown. The boundary of the convex volume consists of polygonal faces.

The surface in Figure 5.5 has 12 vertices and 18 distinct edges forming 8 planar faces. The Euler Characteristic (Guillemin and Pollack, 1974) for the surface is $\chi = F - E + V = 8 - 18 + 12$ is 2, from the fact that its boundary is a compact surface in two dimensions (i.e., topologically a sphere).

Using the method, ILDMs of up to three dimensions (in chemical coordinates, not including the two trivial dimensions from the two thermodynamic parameters, density and internal energy) have been computed successfully. With such high-dimensional manifolds, systematic tessellation of the boundary may no longer be viable and a Monte-Carlo sampling of the eigenspace (or the thermodynamic) boundary should be used.

5.3   Integration on ILDMs

Once an ILDM of a given (or even variable) dimension, representing the slow dynamics of a given set of ODEs, has been computed and stored, its accuracy must be verified. One standard way of testing ILDMs found in the literature is to compare CFD results obtained using ILDMs against full-chemistry benchmark solutions. But considering that the set of ODE represents only one ingredient in solving the full set of evolutionary equations representing the fluid dynamics, and that the ILDM is a reduction of this set of ODEs, it is advantageous to test the ILDM directly in a context independent of the full CFD procedure.

In this section, the ILDM computed with the algorithm developed in the previous section is used with standard ODE solvers to integrate equations having the standard form

$$\frac{d\boldsymbol{y}}{dt} = \boldsymbol{f}\left(t, \boldsymbol{y}; z\right) \ . \tag{5.15}$$

Standard solvers such as the backward difference solver DEBDF of the DEPAC package (Shampine and Watts, 1979), the LSODE suite of Hindmarsh (1983), and all ODE solvers in the MATLAB[*] programming environment, allow the integration of (5.15) through a more or less standard programming interface. The function $\boldsymbol{f}$ of (5.15) representing the vector field of the detailed chemical kinetics is usually provided by a user defined subroutine consisting of CHEMKIN (Kee et al., 1987) calls. In this example, all rate calculations are computed with the newly developed optimized mechanism compiler, *Fuego*, by Michael Aivazis.

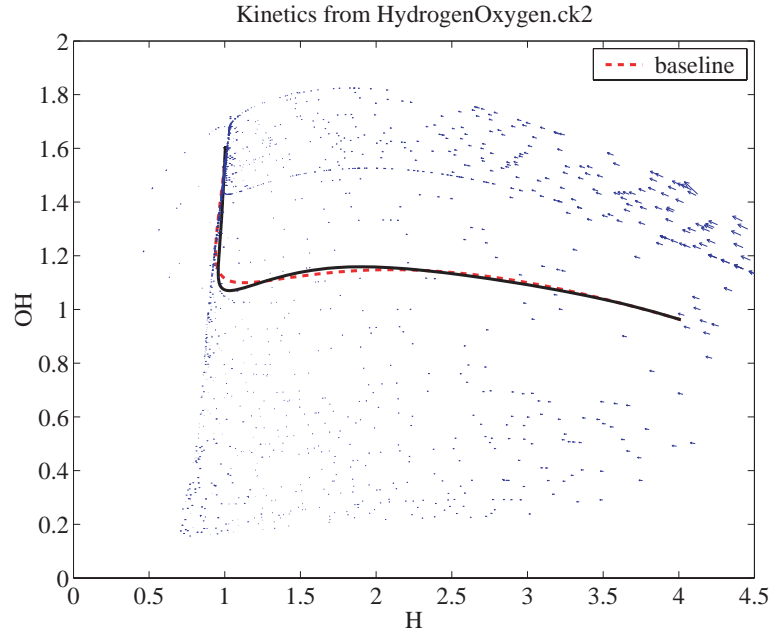[*]MATLAB is a registered trademark of The MathWorks, Inc.

Figure 5.6: Integration on sampled ILDM by unstructured interpolation using MARS (solid line) is compared against the benchmark solution using the full kinetics used in generating the ILDM.

For the reduced kinetics, the function f will be provided instead from interpolation on the ILDM. By using the same interface as the detailed kinetics, switching between full kinetics and ILDM can be done seamlessly and the huge repository of existing ODE solvers can be used without modification. An example of the vector field represented by a two-dimensional ILDM (computed for the Hydrogen-Oxygen mechanism), using the conditions similar to Mixture A (albeit at one-tenth the density), is shown in Figure 5.6.

Also shown in the figure are two trajectories: the solid line represents a solution of the vector field represented by the ILDM starting from a point on the manifold, and the dashed line corresponds to the benchmark solution computed using full kinetics starting from the same initial condition. The backward difference solver DEBDF of Hindmarsh (1983) is used for both cases. Interpolation on the ILDM is done using the MARS (Multivariate Adaptive Regression Splines) package by Friedman (1991).

The advantage of using an unstructured interpolation is twofold. First, as can be seen from Figure 5.6, the vector field from the congruence procedure described at the beginning of this chapter provides a natural adaptive sampling: the one-dimensional ILDM $\mathcal{M}^1$ subset of $\mathcal{M}^2$ has a higher sampling density.
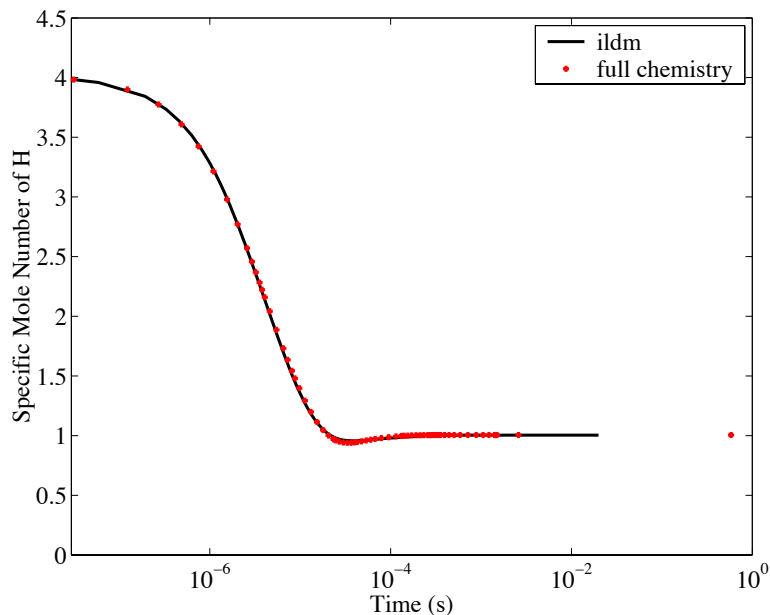
Figure 5.7: The evolution of the amount of H (in mol/kg) computed using the ILDM is compared against the full chemistry solution.

Second, no special precautions are required to handle the manifold boundaries, a difficulty that is discussed in much of the existing literature that deals with implementation details (see for example Eckett, 2001, Maas, 1998).

The temporal evolution of the ILDM trajectory in Figure 5.6 is shown in Figure 5.7 against the full chemistry benchmark. It can be seen that the ILDM solution compares to the benchmark solution with remarkable accuracy.

It should be remarked that, while the ILDM solution in this example is computed using a backward difference solver, more computationally efficient explicit solvers (as in Eckett, 2001) can be used, as much of the stiffness Hairer (1996) associated with the original ODE has been removed. Roughly speaking, the stiffness of an m-dimensional ILDM is the ratio between the m*th* fastest timescale (of the original system) and the slowest, and this ratio is, in general, orders of magnitude smaller than the ratio between the fastest and slowest timescales of the original system.

5.4   Some remarks

There are a few important caveats that limit the usefulness of the ILDM. The first is the curse of dimension: a typical one-dimensional ILDM needs about 100 sampling points, and

the two-dimensional ILDM of Figure 5.4 contains about 5000. Obviously, interpolating on ILDMs of even higher dimension would quickly become a problem. On the other hand, even if storage and interpolation were not problematic, having an ILDM of too high a dimension would still lead to deteriorated accuracy. This may be counterintuitive, but is obvious with the following analogy: a parabola in space can be represented by discretizing it directly much more efficiently and accurately than by putting a three dimensional grid around the curve and locating it as a contour. The question of how many dimensions to use will be addressed in Chapter 6.

In addition, integration on an ILDM requires an initial condition that lies on it, and practical initial conditions never lie on the ILDM. For example, the specific mole number of H in Figure 5.7 begins at 4 mol/kg, clearly not a physically relevant detonable mixture before ignition. In fact, capturing the von Neumann point will in general require an ILDM of a higher domensional than can normally be handled. This issue is explored in §6.5.

Chapter 6

Application of ILDM to ZND detonation

The standard interpretation of ILDM as a reduction technique (Maas and Pope, 1992b) is that it identifies the chemical reactions whose timescales are commensurate with those of the fluid mechanics and decouples them from the rest. Theoretical foundations are not firm as far as we know, but valuable insights have been gained by studying the ILDM technique in the context of singular perturbation methods (Rhodes et al. (1999) and Kaper and Kaper (2002)). We now know, for example, that the aforementioned decoupling is only approximate, and the identification of the slow manifold imprecise. Nevertheless, while the ILDM algorithm is not applicable to dynamical systems in general, it has had much success when applied to chemically reactive systems, and in particular to flame calculations.

Because the fastest processes are explicitly set to equilibrium, it is important to determine the error that results. A convergence study whereby we systematically increase the dimensionality of the ILDM in a CFD calculation is impractical.

6.1   The ZND Model

In this section, the techniques of dimension estimation are applied to a one-dimensional (planar) steady Zel'dovich-von Neumann-Doering (ZND) detonation with detailed chemistry. The equations of motion governing the evolution of the state variables in the steady

frame (see §4A of Fickett and Davis, 1979) are*

$$\dot{p} = -\rho w^2 \frac{\dot{\sigma}}{\eta_n} \ , \tag{6.1a}$$

$$\dot{\rho} = -\rho \frac{\dot{\sigma}}{\eta_n} \ , \tag{6.1b}$$

$$\dot{y}_i = \mathcal{W}_i \frac{\dot{\omega}_i}{\rho} \ , \tag{6.1c}$$

$$\dot{w} = w \frac{\dot{\sigma}}{\eta_n} \ , \text{ and} \tag{6.1d}$$

$$\dot{T} = T \left[(1 - \gamma M_n{}^2) \frac{\dot{\sigma}}{\eta_n} - \frac{\mathcal{W}}{\rho} \sum \dot{\omega}_i \right] \ , \tag{6.1e}$$

where w is the particle velocity in the steady frame, $\eta_n = 1 - M_n{}^2$ is the sonic parameter with M_n being the Mach number, and $\mathcal{W}_i$ and $\dot{\omega}_i$ are the molecular weight and molar production rate of species i, respectively. The thermicity $\dot{\sigma}$ for an ideal gas mixture is defined by

$$\sigma_i = \frac{\mathcal{W}}{\mathcal{W}_i} - \frac{h_i}{c_p T} \ , \tag{6.2}$$

where $\mathcal{W}$ is the mixture average molecular weight, h_i is the specific enthalpy for species i, and c_p is the mixture-averaged specific heat at constant pressure. The thermicity components in (6.2) consist of contributions from mole production as well as enthalpy changes: they determine the coupling between the chemical reaction and the gasdynamics. The contribution of the thermicity coefficients is represented as

$$\dot{\sigma} = \sum_i \sigma_i \dot{y}_i \ . \tag{6.3}$$

From (6.3), net exothermic and mole producing reactions combine to produce positive values of $\dot{\sigma}$, and net endothermic and mole reducing reactions combine to produce negative values.

Given an initial state $(\rho_o, p_o, \boldsymbol{y}_o)$ and a shock speed D, the normal shock relations can be used to determine the post-shocked state, called the von Neumann point, $(\rho(0), p(0), \boldsymbol{y}(0))$ for use as initial conditions of (6.1). The evolution equation for the velocity w (6.1d) is usually not needed because it can be obtained by using the conservation of mass: $\rho(t)w(t) = \rho_o D$. Similarly, other thermodynamic variables $(e, T, \text{ etc.})$ can be obtained as functions of

---

*The temperature equation (6.1e) assumes that the mixture-averaged molecular weight is constant. If this is not the case, it is usually more convenient to obtain temperature as a function of, for example, pressure and density.

Mixture C

Independent quantities	Composition	$2H_2$–O_2–$7Ar$
	Initial Temperature	298 K
	Initial Pressure	0.066 atm
Dependent quantities	Initial Density	8.5e-5 g/cc
	Initial Internal Energy	-7.9e-8 ergs/g
	T_{vN}	1904 K
	T_{CJ}	2807 K
	P_{vN}	1.73 atm
	P_{CJ}	1.06 atm
Reaction Mechanism		Hydrogen-Oxygen

Table 6.1: Properties and reaction mechanism for Mixture C.

$(\rho, p, \boldsymbol{y})$.

The unsupported (CJ) ZND reaction zone structure for stoichiometric H_2–O_2 with 70% Ar dilution, initially at 0.066 atm and 298 K, is computed by numerically solving (6.1) using an adaptation of the program ZND by Shepherd (1986). These conditions are summarized in Table 6.1.

In Figure 6.1, the evolution of temperature and pressure for the ZND detonation is plotted as a function of distance from the leading shock. The spatial profiles of the chemical species O_2 and H are shown in Figure 6.2. The leading shock is located at 0 on the abscissa. It can be observed from these figures that the induction zone length for the detonation is approximately 0.15 cm.

The detailed reaction mechanism (Hydrogen-Oxygen, see Table 1.1) used in this study consists of 12 species from 4 elements (H, O, N, Ar). Three of these species contain nitrogen, which is absent from the mixture. This leaves 9 accessible species and 3 elemental constraints, for a maximum theoretical ILDM dimension of 6. A numerical representation of the ILDM is, as discussed in Chapter 5, a set of points which sample the ILDM. It is clearly impractical to mesh or tabulate a four- (or higher-) dimensional ILDM of any significant size. For example, in Maas (1998), an artificial constraint is introduced that limits the search of the manifold to within some convex hull in composition space.

In other words, while the ILDM solution can extend beyond this artificial boundary, its solution is computed only up to the boundary. This is justified by, and the boundary specified is specified by, the numerical analyst's knowledge of the domain of the accessed (as opposed to accessible) states. For example, while the theoretically accessible states in
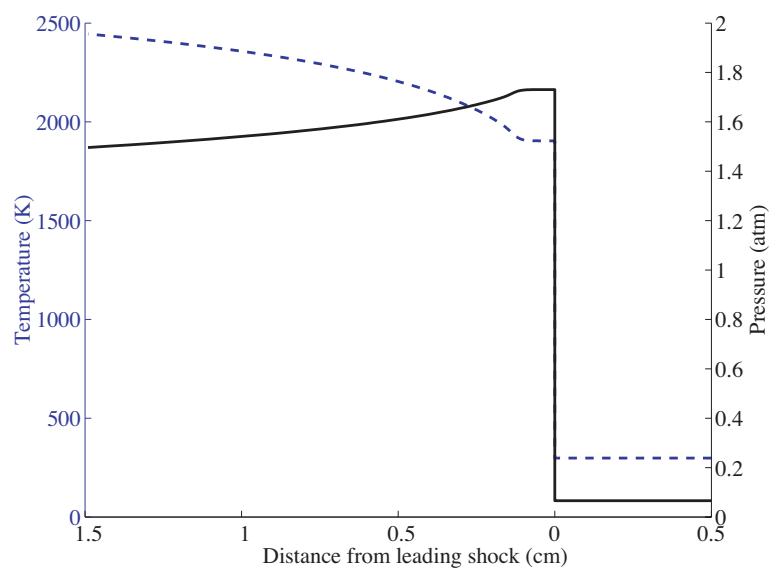
Figure 6.1: The steady ZND profiles for temperature and pressure for stoichiometric H_2–O_2 with 70% Ar dilution, initially at 6.67 kPa and 298 K. Temperature is represented by the dashed line and pressure by the solid line. The induction zone length for the case under study is approximately 0.15 cm.
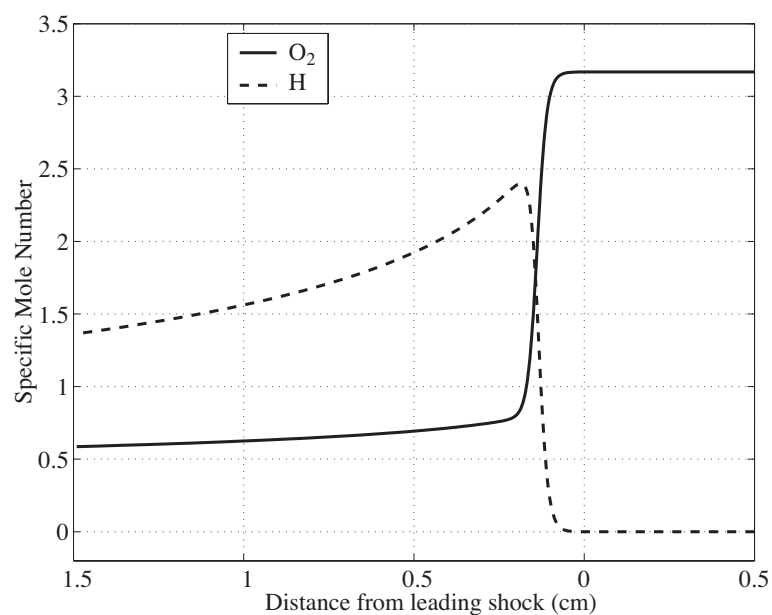

Figure 6.2: The steady ZND profiles for the specific mole numbers of O_2 and H for Mixture C.

a homogeneous, diffusion-less detonation simulation are all compositions that satisfy the elemental conservation constraints, the accessed states are typically highly localized. Such knowledge can be gained from solutions of similar (but often simpler) problems with the full chemical kinetics model.

In addition, the higher the dimensionality of the ILDM sought, the more closely this artificial boundary hugs the accessed states of the model problem in order to avoid the curse of dimension, i.e., an exponential increase in the cost of tabulation with the ILDM's dimension. In Blasenbrey et al. (1999), the authors discussed a strategy for automatic identification of "the boundaries of a convex ILDM independent on a specific application." Their definition of convexity implies only that trajectories starting on the boundary of their computed ILDM remain on the ILDM. However, a model-independent reduction/tabulation can never work, because one can always initialize a calculation to a state that is outside the range of such a tabulation.

Another question that is often raised, but until now not quantitatively addressed, is how far the detailed mechanism can be reduced without seriously affecting the physics of the reacting flow under simulation. In other words, what should the dimension of the ILDM be? Previous work, for example Maas (1998), Singh and Powers (1999),and Eckett (2001), discussed picking a fixed dimension based on a comparison of the fluid mechanics and reaction timescales. Using the concept of ILDM dimensionality discussed in §3.3, the minimum dimension of the ILDM can be computed based on the ZND model.

The ILDM-dim $(\boldsymbol{y})$ (3.23) along the ZND profile of a model problem is computed and shown in Figure 6.3. From this figure, it can be seen that a three-dimensional ILDM $\mathcal{M}^3$ is sufficient to capture most of the flow-field, except in a very thin layer behind the leading shock. The figure also shows that a one-dimensional ILDM (one dimension in species, plus density and energy) fails to capture only the first five microseconds of the transients, justifying what seems to be an absurd amount of reduction as one-dimensional ILDMs are commonly used in the detonation community (Singh and Powers (1999), Singh et al. (2001a)).

It should be noted that, because the unreacted mixture of a detonable gas is in meta-stable equilibrium, its ILDM dimension is *given* a value of zero. The passage of a shockwave of sufficient strength can initiate a reaction, and this is manifested as an increase in ILDM dimensionality. This can be seen in Figure 6.3.
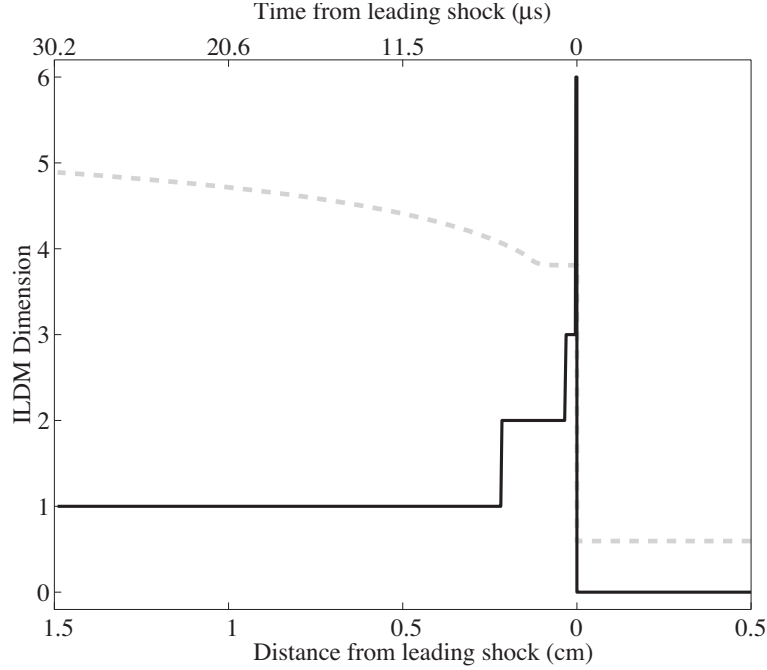
Figure 6.3: The ILDM dimension along the CJ ZND trajectory is plotted. The temperature profile is superimposed on the plot as the dashed line.

The thin layer immediately behind the leading shock, containing the extremely fast transients, can be examined more closely in Figure 6.4. The rapid build-up of OH radical in this high-dimensional induction region is clearly seen.

6.2 Treating the fastest transients

As seen quantitatively in the previous section, and discussed in Eckett (2001), the induction zone region contains fast transients and the dynamics cannot be represented by low-dimensional ILDMs. In fact, such high-dimensional regions are not limited to the induction zones. For slightly more complex systems, such as with the mixture H_2–N_2O–$3N_2$ described in Pintgen et al. (2002), the dimensions are high even away from the induction region. The ILDM dimensionality along the ZND profile for the mixture initially at 298 K and 20 kPa, having an overdrive factor f of 1.4, is shown in Figure 6.5.

The overdrive factor f is defined as

$$f = \left(\frac{u_{\mathrm{znd}}}{u_{\mathrm{CJ}}}\right)^2 , \tag{6.4}$$
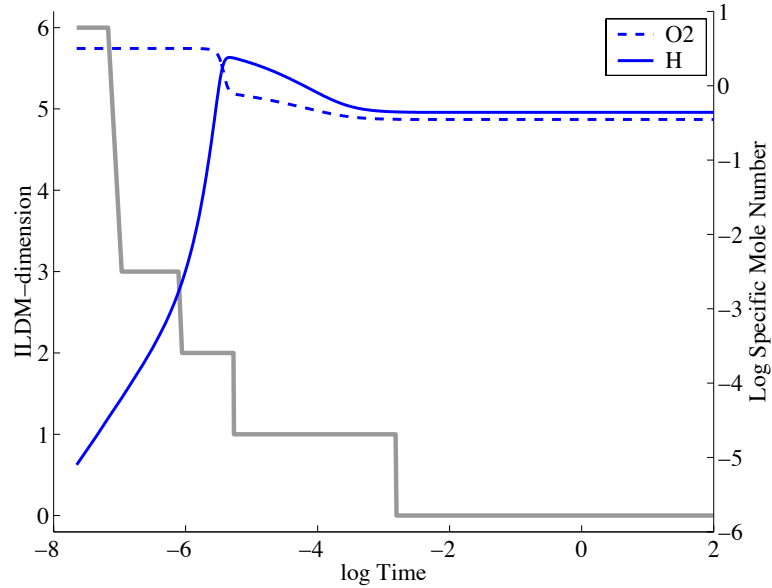
Figure 6.4: The species evolution and ILDM dimension for the ZND detonation are shown using log scales.

where u_{znd} is the detonation velocity of the steady ZND detonation and u_{CJ} is the CJ velocity and is the minimum velocity for which a ZND solution exists (see, for example, Fickett and Davis, 1979). The detailed mechanism used consists of 4 elements and 20 species (Miller and Bowman, 1989), of which the 12 species mechanism used previously for Hydrogen-Oxygen detonation is a subset.

ILDM, by its very definition, is designed to handle near equilibrium processes. The equation defining the manifold, previously introduced in Chapter 3, is

$$\mathcal{M}^k = \{\boldsymbol{y} : \hat{\mathsf{V}}_f f(\boldsymbol{y}) = \boldsymbol{0}\} \, . \tag{3.5}$$

All the rate information of the chemical kinetics as a function of the composition is embodied in the function $f(\boldsymbol{y})$. Thermodynamic equilibrium (for a well-formed set of reaction pathways) will satisfy (3.5) exactly, because all the components of f are zero ($f(\boldsymbol{y}) = \boldsymbol{0}$). The definition of the ILDM can be viewed as a more relaxed definition of equilibrium: an n-dimensional ILDM corresponds to states where, written in a sorted eigenbasis, all but n components of f are zero.
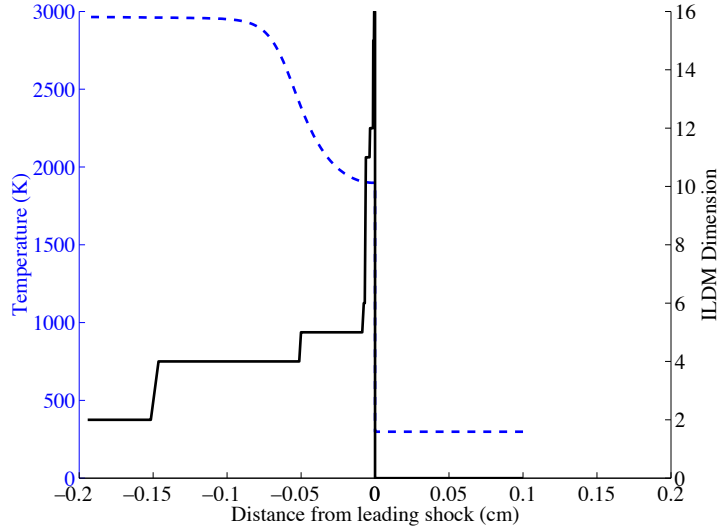
Figure 6.5: The ILDM dimension of an overdriven ZND detonation of H_2–N_2O–$3N_2$ is shown as a function of distance from the leading shock. The dashed line is the temperature profile and gives an visual indication of the length of induction region.

6.3 Conservation laws and ZND detonation

Since the initial transients of a detonation equilibrate quickly, manifestation of which is that the induction zone is thin compared to the length of the reaction zone, the question arises whether these transients can be assumed to occur infinitely fast? This issue will be explored from a thermodynamic point of view.

For a detonation wave propagating with velocity D into a mixture with initial state $(\rho_o, p_o, \boldsymbol{y}_o)$, conservation of mass and momentum requires that the thermodynamic state of a particle (ρ, p) behind the detonation front for a steady process lies on the Rayleigh line in the p-v plane (see Fickett and Davis, 1979):

$$\mathcal{R} = \rho_o^2 D^2 - \frac{p - p_o}{v_o - v} = 0 \tag{6.5}$$

In addition, conservation of energy requires the state $(\rho, p, \boldsymbol{y})$ to lie on the Hugoniot curve

$$\mathcal{H} = e(\rho, p, \boldsymbol{y}) - e(\rho_o, p_o, \boldsymbol{y}_o) - \frac{1}{2}\frac{p + p_o}{v_o - v} = 0 \ , \tag{6.6}$$

where e is the equation of state. For systems of ideal gases, $e = e(T, \boldsymbol{y})$ (2.35). A p-v diagram for the stoichiometric detonation at an overdrive $f = 1.4$ of a hydrogen and oxygen mixture, initially at 300 K and 1 atm, is shown in Figure 6.6. The mixture properties are summarized

		Mixture D
Independent quantities	Composition	$2H_2$–O_2
	Initial Temperature	300 K
	Initial Pressure	1.0 atm
	Overdrive f	1.4
Dependent quantities	CJ velocity u_{CJ}	2840 m/s
	Detonation velocity D	3361 m/s
	T_{vN}	2307 K
	T_{CJ}	3967 K
	P_{vN}	46.38 atm
	P_{CJ}	39.81 atm
Reaction Mechanism		Hydrogen-Oxygen

Table 6.2: Properties and reaction mechanism for Mixture D.

in Table 6.2. The temperature, pressure and ILDM dimensionality along the ZND solution are plotted as a function of the distance from the leading shock in Figure 6.7(a).

The ZND solution $p(x)$ and $v(x)$ along the reaction trajectory, where x is a the distance from the leading shock, can be written as $p(v)$. Being a steady solution, the function $p(v)$ must lie on the overdriven Rayleigh line, starting from the unreacted Hugoniot and ending at the equilibrium Hugoniot. As illustrated in Figure 6.7(b), the solution seems to be comprised of states lying on $\mathcal{M}^2$ and $\mathcal{M}^1$ only when the ILDM dimensions is as high as 6 (from Figure 6.7(a)). The reason, as shown in Figure 6.7(a), is that the ILDM dimension drops from 6 to 2 with hardly any pressure change; the drop from 6 to 2 happens entirely inside the energetically neutral induction zone.

6.4   The missing transients

Assuming that a one-dimensional ILDM is chosen for this problem, the states in the induction zone that do not lie on $\mathcal{M}^1$ cannot be represented. The effects of treating these ignored transients as occuring infinitely rapidly are investigated in this section.

Since the definition of a one-dimensional ILDM $\mathcal{M}^1$ is based on the adiabatic constant-volume combustor (see §2.2), the exact projection of an initial state $(\rho, e, \boldsymbol{y})$ to $\mathcal{M}^1$ is the integration of (2.11) until the trajectory reaches $\mathcal{M}^1$, followed by the assumption that this process happens instantaneously. However, because this integration happens at constant density and internal energy, the pressure of the final (projected) state cannot be constrained.
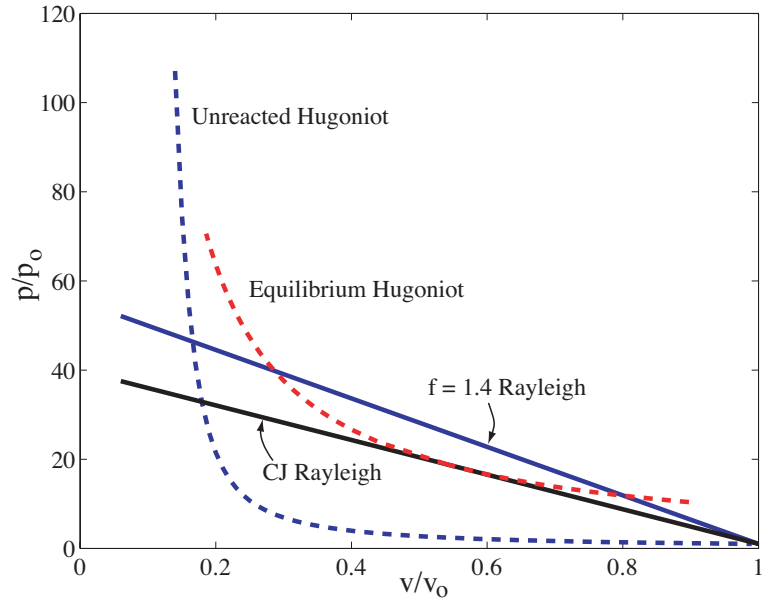
Figure 6.6: p-v diagram for H_2-O_2 detonation at $f = 1.4$ (Mixture D of Table 6.2).

(a) ILDM dimension along ZND solution
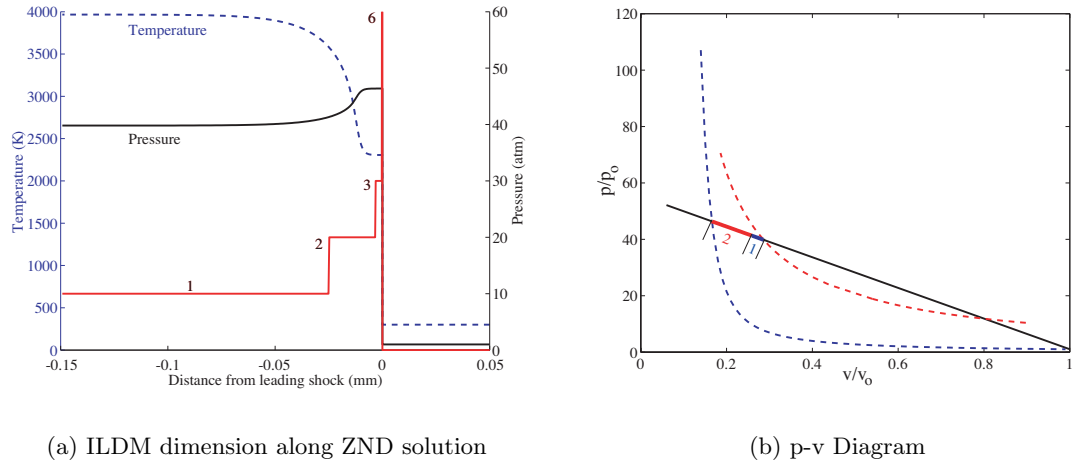
(b) p-v Diagram

Figure 6.7: The ILDM dimensionality profiles (a) and p-v diagram (b) for Mixture D of Table 6.2.
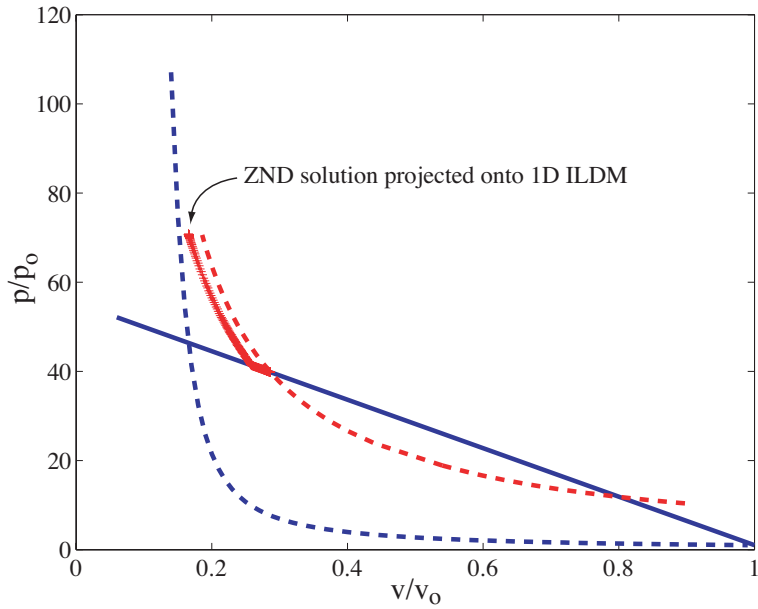
Figure 6.8: Projecting the ZND solution onto $\mathcal{M}^1$. States initially on $\mathcal{M}^1$ are unchanged, the remaining are evolved as an adiabatic constant volume process towards equilibrium.

The effect of this projection is shown in Figure 6.8.

We can conclude from Figure 6.8 that using an ILDM of insufficient dimension (for this example, $\mathcal{M}^1$) leads to a completely unrealistic reaction zone structure that is unfaithful to the actual ZND structure. However, as seen in Figure 6.7(b), a projection onto $\mathcal{M}^2$ will stay on the Rayleigh line, since $p(v)$ lies on ILDMs of dimension 2 or less.

The difference comes from the fact that, even though the state immediately behind the shock has an ILDM dimension of 6, it drops to 2 without any significant pressure change.

In other words, by considering only the steady-state solutions, the fast initial transients can be assumed infinitely fast only when the thermicity $\dot{\sigma}$, a measure of the contribution from heat release as well as mole changes, is negligible. The problem illustrated in Figure 6.8 is in fact a consequence of the operator-split procedure for the CFD calculation, for the following reason. If the initial transients were assumed to be infinitely fast, the composition, pressure and volume would evolve (infinitely quickly) along the Rayleigh line. The operator-split scheme, however, forces the composition to change at fixed internal energy and volume, which leads to catastrophic results. The effect of the operator-split scheme will be discussed in more detail later.

6.5   Reaction manifolds

An obvious solution for handling states that do not lie on an ILDM is to solve the full system, and the ILDM is used only when the state to be integrated lies sufficiently close to the ILDM. This approach is followed, for example, in Singh et al. (2001a) in conjunction with a one-dimensional ILDM (with a lookup table dimension of 3, because of the ILDM's dependence on the two additional parameters ρ and e).

In this section, the "induction manifold" approach of Eckett (2001) is described. It is designed to integrate states in the induction zone, where the method of ILDM is inapplicable. The method, which reduces the full mechanism to a one-parameter progress variable-based integration, bridges the gap between a given initial state and the ILDM. Developed independently for use in flame simulations, the method of "Flamelet Generated Manifold" (van Oijen and de Goey, 2000) considers a multi-dimensional flame as an ensemble of one-dimensional laminar flamelets. Similarly, the induction manifold treats chemical reactions across the leading shock as an ensemble of adiabatic constant-volume self-ignition processes.

As can be seen from Figure 6.5, it is not always practical to use an ILDM of so high a dimension as to be valid up to the end of the induction region. Anticipating the use of the induction manifold technique throughout the entire flow domain, not limited to the induction region, the technique will be renamed the *Reaction Manifold*.

Let the unreacted mixture composition be $\boldsymbol{y}_o$. The adiabatic constant-volume solution is a two-parameter family of trajectories $\boldsymbol{y}(t; \rho, e)$ which solves (2.18a) with initial conditions $\boldsymbol{y}(0) = \boldsymbol{y}_o$ at constant ρ and e. This family of trajectories can be thought of as a trajectory-valued function of the two variables ρ and e. The pairing (ρ, e) recurs often, and will be called the *thermodynamic coordinate*. This, together with *composition coordinate* $\boldsymbol{y}$, determines the complete state of the system. The reaction manifold is

$$\mathcal{IM} : (\rho, e) \mapsto \boldsymbol{y}(t) \ . \tag{6.7}$$

The technique of the reaction manifold assumes, and is in fact motivated by the observation, that states accessed in CFD simulations of detonations lie close to this family. In

other words, for all states $(\rho, e, \boldsymbol{y})$ in the induction zone, there exists t^* such that

$$\mathcal{IM}(\rho, e)(t^*) \simeq \boldsymbol{y} \ . \tag{6.8}$$

The application of this technique to the time-advance operator $\mathcal{L}_S$ is immediate:

$$\mathcal{L}_S : \boldsymbol{y}(t) \mapsto \boldsymbol{y}(t + \Delta t) = \mathcal{IM}(\rho, e)(t^* + \Delta t) \tag{6.9}$$

When can (6.9) be expected to well approximate the operator $\mathcal{L}_S$? One clear requirement is that the unreacted (preshock) state should be homogeneous, with composition $\boldsymbol{y}_o$. In addition, the flow has to be diffusionless so that the elemental composition remain constant. If the trajectories of the chemical system $\dot{\boldsymbol{y}} = \boldsymbol{f}(\boldsymbol{y}; \rho, e)$ follow the same path (possibly at different speeds) with respect to the thermodynamic coordinate (ρ, e), then the reaction manifold will be exactly correct. The concept of orbits is useful here; orbits are the points in phase space that lie on a trajectory, whereas a trajectory is a function of time that is a solution of the differential equations.

For example, when a single non-reversible progress variable is used through an Arrhenius rate law to represent a reaction, the reaction paths (orbits) are independent of temperature and pressure; the progress variable (in one-dimensional phase-space) always goes from $\lambda = 0$ towards $\lambda = 1$. In this respect, the reaction manifold technique reduces the full mechanism to a non-reversible progress variable-based reaction, the state-dependent reaction rate of which comes from the full mechanism and not from an analytical rate law. This assumption is most valid near the initial composition and in the induction region, where the physical processes to initiate the chemical reactions can generally be assumed to follow a single-route. This behavior makes sense for chemical mechanisms, but is clearly not true for dynamical systems in general.

On the other hand, the reaction manifold will again be valid near the equilibrium point because the last part of each trajectory in $\mathcal{IM}$ is part of the attracting manifold $\mathcal{M}^1$.

The approximate validity of the technique is illustrated in Figure 6.9(a) using the ZND detonation of Mixture D (Table 6.2). The circle marker represents one point along the ZND trajectory (dashed line), and its state is denoted by $(\rho^*, e^*, \boldsymbol{y}^*)$. The solid line is then given by $\mathcal{IM}(\rho^*, e^*)$ of (6.7). Because the trajectory $\mathcal{IM}(\rho^*, e^*)$ passes very near to the marker,

(a) Reaction Manifold Illustration

(b) Parametric Dependence of Trajectories
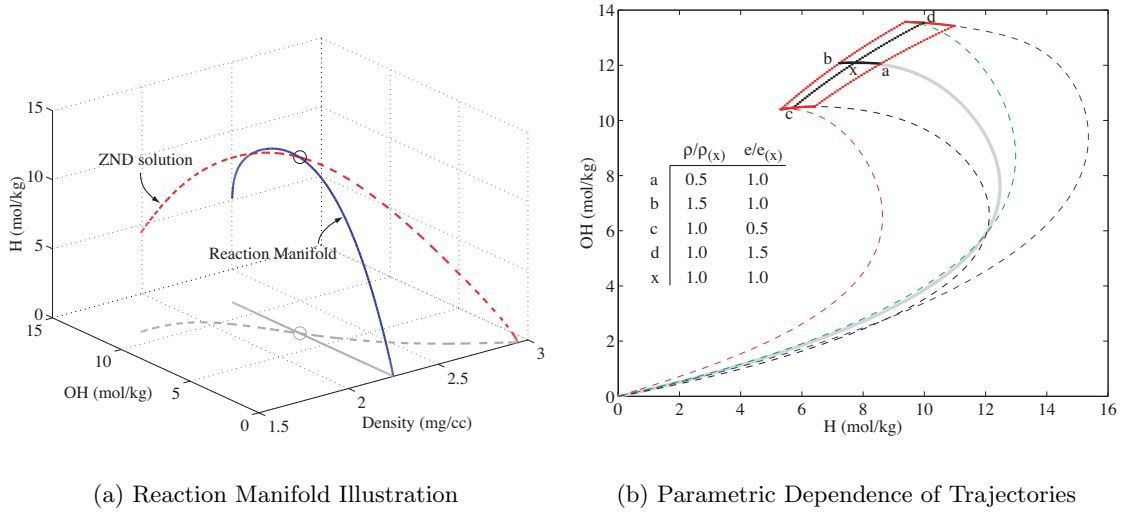
Figure 6.9: The ZND solution is seen to lie close to the reaction manifold (a). Smooth parametric dependence of trajectories on the thermodynanmic coordinate (ρ, e) is shown in (b).

there exists t^*, defined in (6.8), such that $\mathcal{IM}(\rho^*, e^*)(t^*) \simeq \boldsymbol{y}^*$. As discussed earlier, this approximate equality is very accurate near the end of the trajectory because it is part of $\mathcal{M}^1$, and is accurate near the initial conditions because of the orbits initial independence on the density and internal energy. This, and the smooth dependence of trajectories with respect to density and internal energy, is shown in Figure 6.9(b).

So far two interpretations have been given for the reaction manifold algorithm. The first is as a reduction of the full mechanism to a progress variable-based reaction, and the second is as an extended one-dimensional manifold $\mathcal{M}^1$ that works well initially (near the initial composition) and terminally (on $\mathcal{M}^1$).

A third interpretation is that the reaction manifold is a high-dimensional ILDM computed on a very limited (infinitely thin) region according to typical accessed states of a CFD simulation. This interpretation is consistent with high-dimensional (4D, for example) ILDMs that are computed within a very tightly specified region in phase-space.

A one-dimensional ZND detonation is computed using the reaction manifold to approximate the chemistry operator $\mathcal{L}_S$, and a comparison of the spatial density profile with the full mechanism solution is shown in Figure 6.10.

The reaction manifold technique is shown to be capable of reproducing the steady structure of the ZND detonation, in spite of its drastic reduction of a detailed mechanism to a
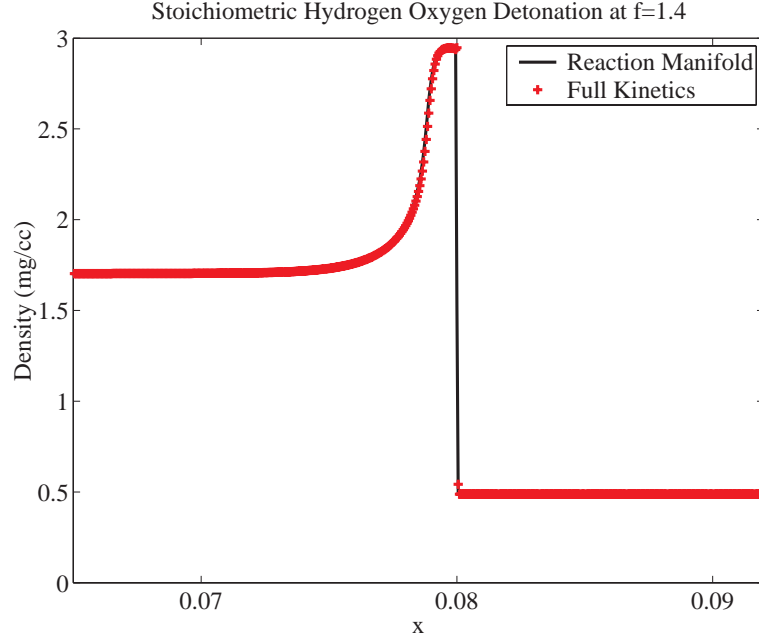
Figure 6.10: Applying the reaction manifold to a CFD simulation. The steady-state detonation profile of the full mechanism (symbols) is accurately captured by this simple reduction.

single progress variable. Another substantial advantage of this method is that the family of trajectories $\mathcal{IM}$ can be computed on the fly. In fact, the reaction manifold technique has been implemented as an ODE solver using the simple algorithm specified in 6.1.

In the C++ implementation, the function T returns a `pair⟨int,int⟩` defined in the standard library, which can be used as a key to index the dictionary `map`. The algorithm builds up the trajectory database, and hence $\mathcal{IM}$, as the simulation proceeds.

The integrator is also robust in the sense that the return value always comes from trajectories computed using the full mechanism, ideally with an implicit solver. As such, the value returned by the integrator is always a valid composition. Compared to other integrators that solve the full mechanism approximately (and perhaps explicitly) to improve speeds, the result of the approximate integration is prone to unphysical compositions, such as negative mass-fractions or states that lead to unphysical temperatures when the equation of state is solved.

The accuracy, however, depends critically on the last step in Algorithm 6.1. To illustrate, consider the one-dimensional timestep splitting

$$\boldsymbol{W}^{t+\Delta t} = \mathcal{L}_S \mathcal{L}_{F_x} \boldsymbol{W}^t \ , \tag{6.10}$$

---

constants: $\Delta\rho$, Δe and $\boldsymbol{y}_o$

definitions:

$$T(\rho, e) = (\text{floor}(\rho/\Delta\rho), \text{floor}(e/\Delta e))$$

$$T^{-1}(i, j) = ((i + 1/2)\Delta\rho, (j + 1/2)\Delta e)$$

input: $\rho, e, \boldsymbol{y}, \Delta t$

Get trajectory $\boldsymbol{y}(t)$ from database.

(1) See if trajectory indexed by $T(\rho, e)$ is in database.
Return trajectory if found.

(2) Compute constant-volume trajectory subjected to the initial
density and energy from $T^{-1}(T(\rho, e))$ and the initial composition $\boldsymbol{y}_o$
Add trajectory to database and return trajectory.

Find t^* on $\boldsymbol{y}(t)$ such that $\boldsymbol{y}(t^*) \simeq \boldsymbol{y}$.

return: $\boldsymbol{y}(t^* + \Delta t)$

Algorithm 6.1: The reaction manifold integrator.

---

where the operators $\mathcal{L}_S$ and $\mathcal{L}_{F_x}$ are the same as in (2.6). Suppose that the evolution of a (Lagrangian) particle is followed, and that its state is initially $(\rho_1, e_2, \boldsymbol{y}_1)$. The use of the reaction manifold implies that the state $\boldsymbol{y}_1$ is constrained on $\mathcal{IM}(\rho_1, e_1)$. In the absence of diffusion, the operator $\mathcal{L}_{F_x}$ then has the effect of perturbing the density and energy to (ρ_2, e_2) with $\boldsymbol{y}_1$ held constant for the Lagrangian particle. Because of the general dependence of reaction orbits on density and energy, the state $\boldsymbol{y}_1$ does not lie on $\mathcal{IM}(\rho_2, e_2)$. The determination of t^* in the algorithm is equivalent to a projection onto $\mathcal{IM}(\rho_2, e_2)$ and, unfortunately, many choices are possible.

In spite of the ILDM's liberal use of inner products (since it requires the notion of orthogonality), which implicitly defines the metric, it is not clear whether the Euclidean metric is the natural one for the chemical configuration (phase) space. One alternative is entropy projection: find $s_1 = s(\rho_1, e_1, \boldsymbol{y}_1)$ and define t^* such that $s(\rho_2, e_2, \mathcal{IM}(\rho_2, e_2)(t^*)) = s_1$. The advantage of entropy projection is that entropies for CV trajectories are always monotonic, so if s_1 is larger than the maximum (equilibrium) entropy on $\mathcal{IM}(\rho_2, e_2)$, it is clear that the correct projection is the equilibrium point. Furthermore, the projection obviously does not violate the second law of thermodynamics.

Unfortunately, entropy is not a good indicator of progress and such a projection can change the temperature quite significantly if the perturbation is high. This is undesirable since the reaction rates depend exponentially on temperature. Moreover, an isothermal projection is impossible because temperature does not always vary monotonically for constant-volume reactions, and in addition, the temperature variation in the induction zone is so small that such a projection is bound to be inaccurate.

From experience with numerical simulations, the best projection is any monotonically varying species that is known to be a good indicator of the reaction progress. For the simulation shown in Figure 6.10, the amount of H_2O is used as the progress variable.

6.6   Some remarks on the operator splitting

Assuming that a projection is chosen, can we expect the CV trajectory starting from $(\rho_2, e_2, \boldsymbol{y}_1)$, denoted by $\boldsymbol{y}_1(t)$, to stay close to $\mathcal{IM}(\rho_2, e_2)$?

If the trajectory $\mathcal{IM}(\rho_2, e_2)(t^* + t)$ is denoted by $\boldsymbol{y}(t)$, the question becomes whether

$$\boldsymbol{y}_1(t) \simeq \boldsymbol{y}(t) \ ? \tag{6.11}$$

If $\boldsymbol{y}_1$ is a small perturbation of $\boldsymbol{y}(t^*)$, then $\mathbf{u} = \boldsymbol{y}_1(0) - \boldsymbol{y}(0)$ measures the distance between the trajectories. The evolution of $\mathbf{u}(t)$ is governed by the variational equation (see, for example, Hirsch and Smale, 1974) of the original CV system in (2.11),

$$\dot{\mathbf{u}} = \mathsf{J}(t)\mathbf{u} \ , \tag{6.12}$$

where $\mathsf{J}(t)$ is the time-dependent Jacobian matrix of the original adiabatic constant-volume system. Because experience (and Eckett, 2001) has shown that the spectrum of J is usually negative, the distance between the two trajectories will shrink. This is a desirable property that is not true for dynamical systems in general. An extreme example is a chaotic invariant set (Holmes et al., 1996), where almost all pairs of trajectories, starting arbitrarily closely, diverge.

The effect of the operator split, and hence the actions of the operators $\mathcal{L}_{F_x}$ and $\mathcal{L}_S$, is now discussed in the context of an Eulerian flow simulation. Applying the timestep-splitting of (6.10) to a one-dimensional CFD calculation of a ZND detonation, the steady-state solution of the reactive Euler equation thus obtained should coincide with the solution obtained by solving the ZND structure equation.

Using (6.10), the state accessed by a single control volume during the passage of a detonation can be plotted. This is shown in Figure 6.11. The solid line is the solution obtained by solving the ZND structure equation (6.1). The symbols chart the temporal evolution of the thermodynamic coordinate (represented on the abscissa by the density) and the composition coordinate (represented on the ordinate axis by the mass-fractions of OH) of a single control-volume. The effect of the operator $\mathcal{L}_S$ in this case is the same as discussed earlier in the Lagrangian setting: it updates the chemical composition of the fluid element in the control volume at constant ρ and e. The operator $\mathcal{L}_{F_x}$, because of the Eulerian setting affects not only the thermodynamic coordinate (ρ, e), but also the composition $\boldsymbol{y}$ because of convection. The overall effect of the time-advance operators $\mathcal{L}_S LX$ is to converge to the steady ZND solution, obtained by solving the coupled gasdynamics-chemistry system
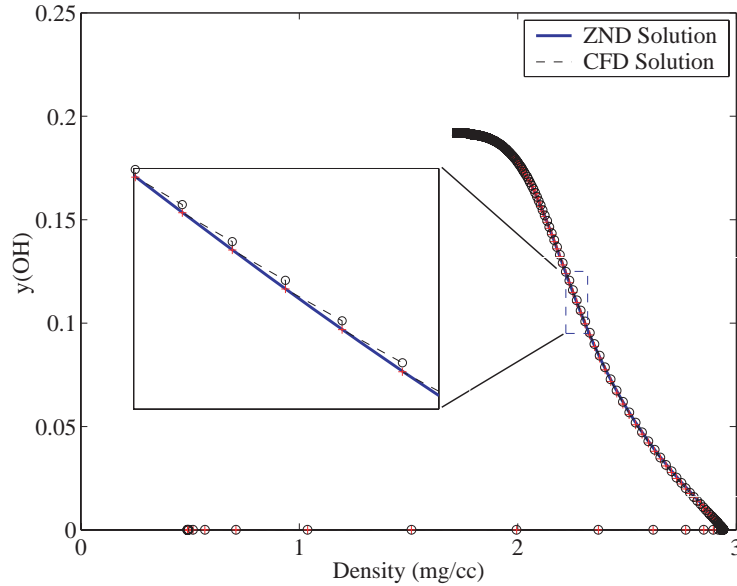
Figure 6.11: Illustrating the effect of $\mathcal{L}_{F_x}$ and $\mathcal{L}_S$ for a one-dimensional calculation of stoichiometric Hydrogen-Oxygen detonation (Mixture D, Table 6.2) at $f = 1.4$. The solid line is the solution of the ZND structure equation and the dotted line joining the symbols comes from a one-dimensional CFD simulation solving the reactive Euler equations.

directly without splitting.

There are two observations that can be made from Figure 6.11. First, the effect of the operator $\mathcal{L}_S$ and $\mathcal{L}_{F_x}$ is small. This is necessarily so by design because, in general, the CFD computation will be set up to resolve high gradients, and variables will therefore change "slowly" through one timestep. This means that the perturbation from $\mathcal{L}_S$ to (ρ, e) across a timestep will be small, *unless* the calculation is under-resolved (which could lead to instability of the method).

The second observation is that, when the calculation is resolved, the action of the operator $\mathcal{L}_S$ is also small (as can be observed qualitatively from the figure). This action $y^t \rightarrow y^{t+1}$ can be of the same magnitude as the projection $y^t \rightarrow y^{t^*}$. In fact, near equilibrium, the actual reaction rate is so slow that any projection leads to large errors.

To illustrate, the diffraction of a CJ detonation wave in the mixture of $2H_2$–O_2–$7A$rover a cylindrical obstacle, initially at 6.67 kPa and 298 K, is simulated. Numerical schlieren-type images are computed using the algorithm described in Quirk (1994). Figure 6.12 shows four frames of the detailed chemistry simulation in the frame of reference of the right-running shock (hence the stationary obstacle appears to run to the left). The corresponding frames computed using reaction manifold reduced kinetics are shown in Figure 6.13. It can be

observed from these two figures that while the main phenomena and the strong gradients, namely the leading detonation and the reflected shocks, are reproduced using the reaction manifold technique, the weaker gradients, for example the expansion behind the curved reflected shock, are noisy in the reduced simulation.
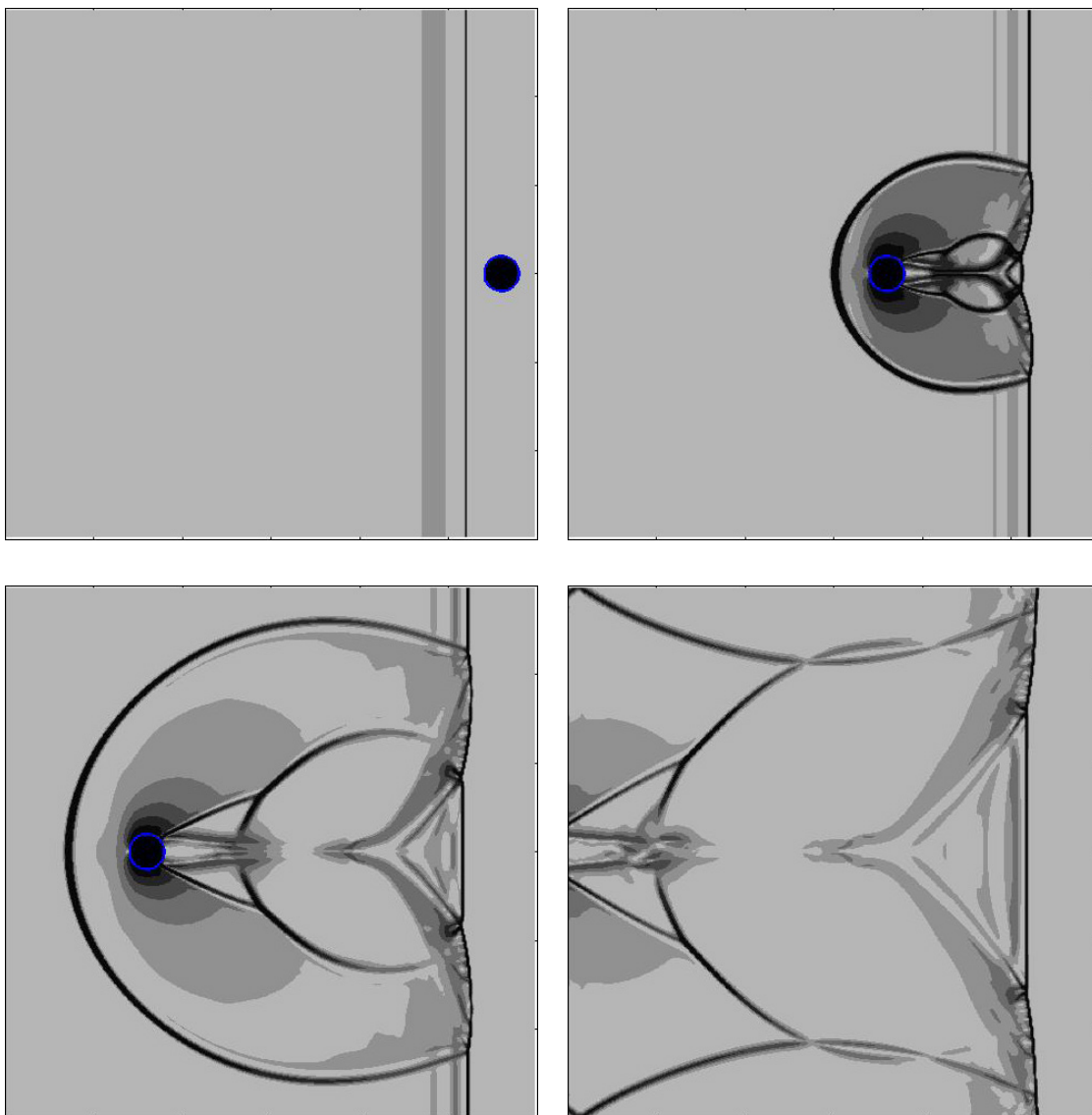
Figure 6.12: Numerical schlieren images for a detonation diffraction over cylindrical obstacle. Mixture: $2H_2$–O_2–$7Ar$, initially at 6.67 kPa and 298 K.
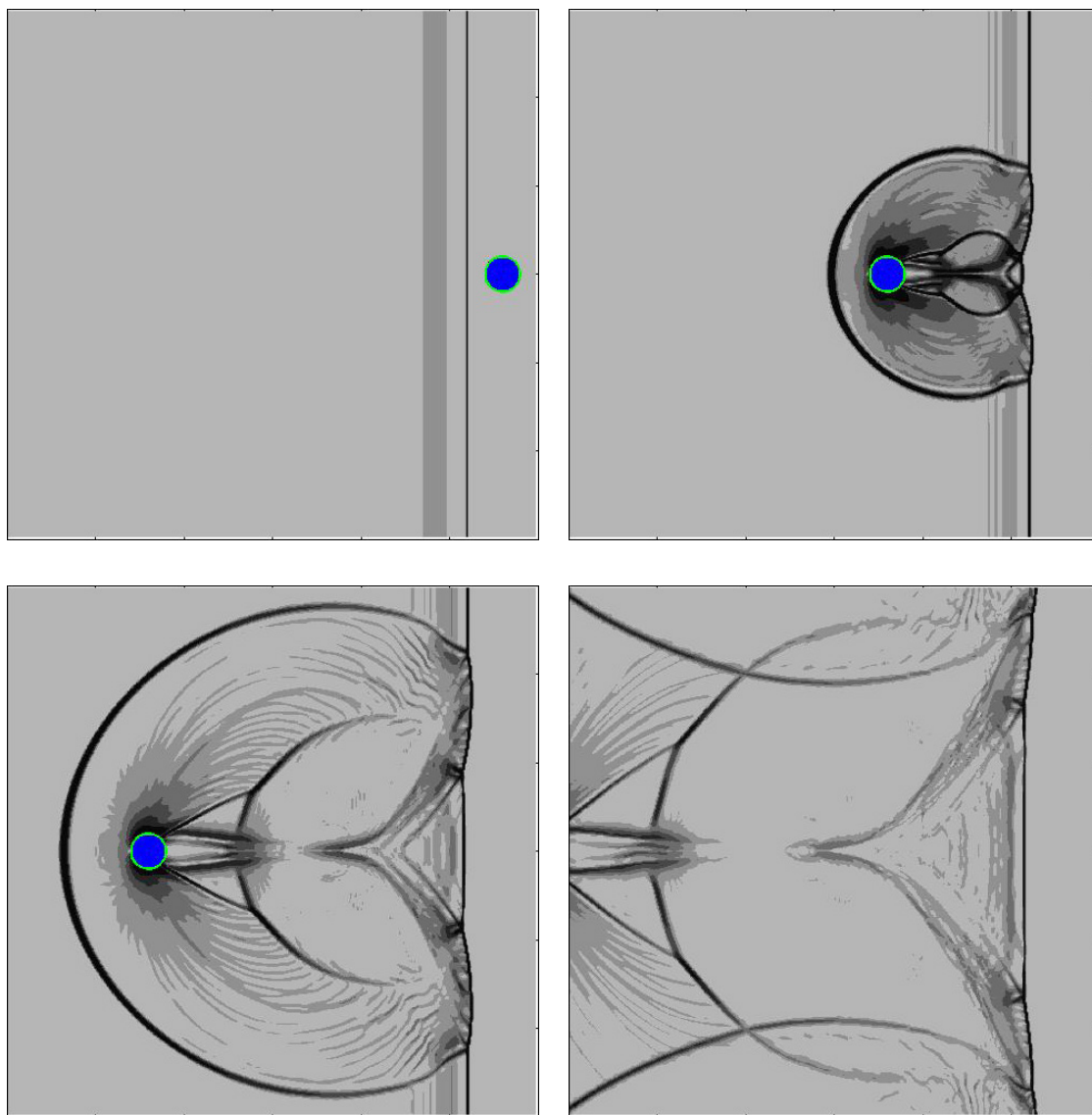
Figure 6.13: Simulation of Figure 6.12 using reaction manifold reduced chemistry.

Chapter 7

Detonation Initiation by Hypersonic Projectiles

In this chapter, we discuss progress towards understanding the phenomenon of detonation initiation by projectiles, inspired by the experiments of Kaneshige. In Kaneshige (1999) different flow regimes, including both steady and unsteady shock-induced combustion and stabilized and unstable detonation initiations, are experimentally observed. The two contrasting combustion modes of stabilized steady shock-induced combustion and stabilized detonation are illustrated, together with shadowgraph images from Kaneshige (1999), in Figure 7.1.

A theoretical model based on shock curvature has been developed to predict detonation initiation. The method, based on local considerations of the temperature derivative at the shock front, is verified by means of detailed numerical simulations in two dimensions.

7.1   Governing equations for steady reactive flows in two dimensions

The equations governing the evolution of a steady, inviscid, two-dimensional compressible reacting flow can be written in a *natural coordinate system* following the approach of Liepmann and Roshko (2001). Let the orthogonal coordinate system *s-n* be defined such that streamlines are lines of constant n, as shown in Figure 7.2(a). Such a natural coordinate system is shown in Figure 7.2(b) for a planar, steady supersonic flow around a cylindrical projectile (see Table 7.1), to be discussed in §7.2.

The constant s coordinate lines of Figure 7.2(b) are streamlines from integrating, using the Tecplot$^{\circledR}$ package*, the velocity field (u, v) of the simulation described in §7.2. Ac-

---

*Tecplot is a registered trademark of Amtec Engineering Inc.
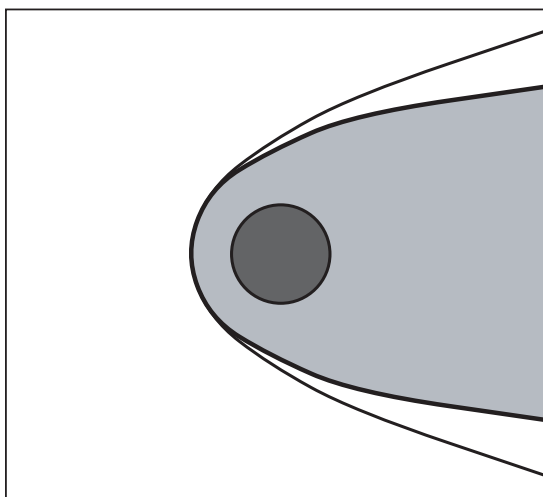
(a) Shock-induced supersonic combustion
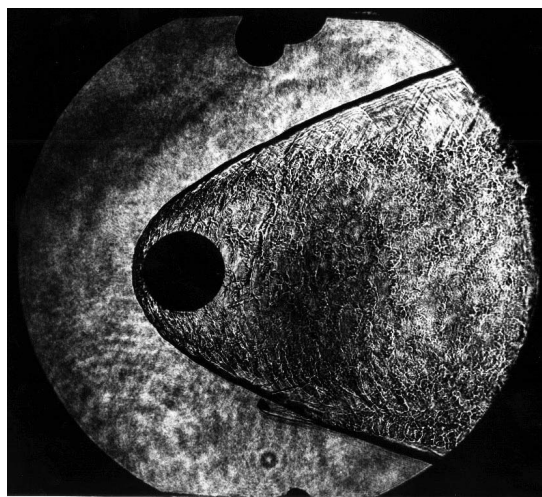
(b) Shadowgraph (Supersonic combustion)

Coupled Reaction Zone
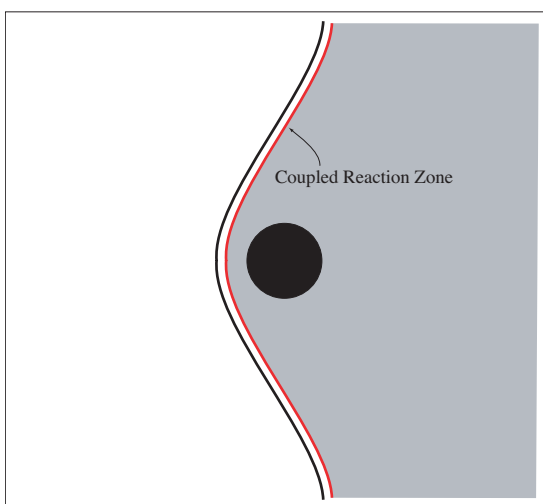
(c) Stabilized Coupled Detonation

(d) Shadowgraph (Coupled Detonation)

Figure 7.1: Illustrations and shadowgraphs of supersonic combustion versus detonation initiation. Projectile is 25.4 mm in diameter traveling in stoichiometric Hydrogen-Air $2H_2$–O_2–$3.76N_2$ at room temperature. The initial pressures are 42.1 kPa for (b) (taken from Figure B.43 of Kaneshige, 1999) and 256 kPa for (d) (taken from Figure B.61 of Kaneshige, 1999).

(a) The *natural coordinate system*
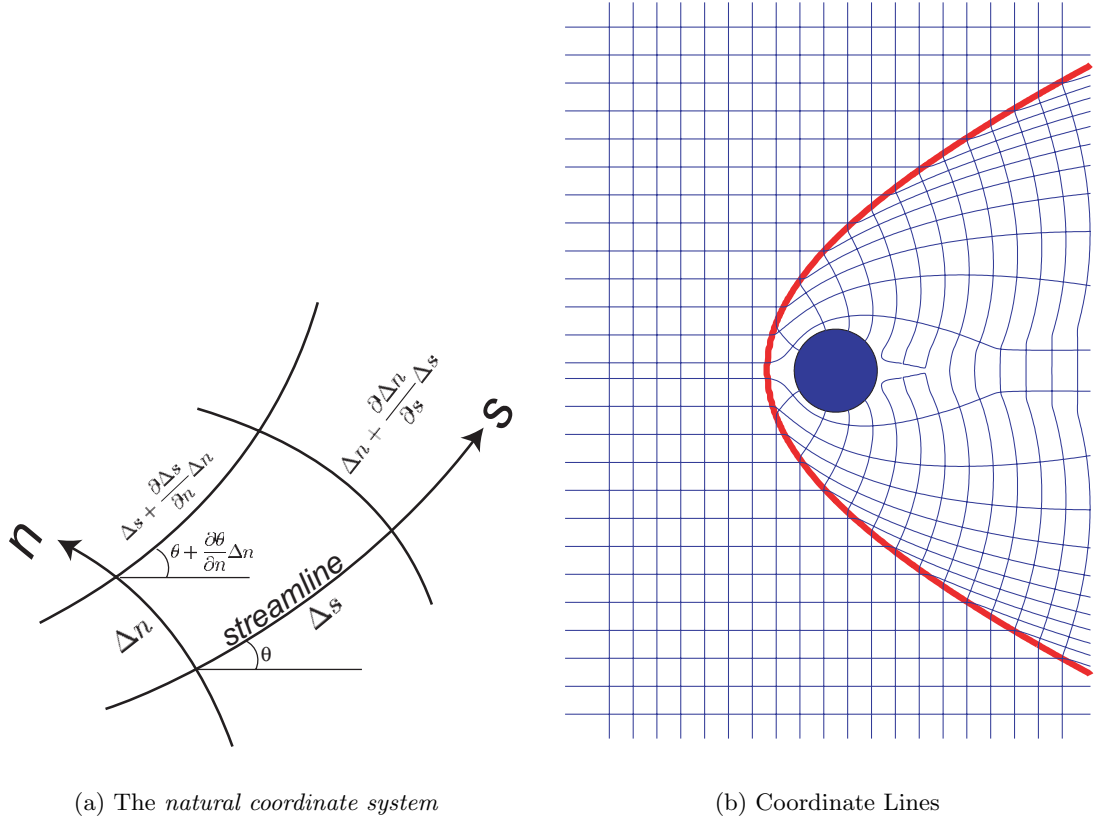
(b) Coordinate Lines

Figure 7.2: The *natural coordinate system* along streamlines (a) and for chemically reactive steady flow around a projectile (b).

cording to Amtec Engineering, Inc. (1998), the integration is performed using a predictor-corrector algorithm with adaptive step-size control. Similarly, the constant n lines are obtained by integrating the field of normals $(-v, u)$, and are everywhere tangent to the streamlines.

The conservation equations are

$$\frac{\partial}{\partial s}(\rho u) + \rho u \frac{\partial \theta}{\partial n} = 0, \tag{7.1a}$$

$$\rho u \frac{\partial u}{\partial s} + \frac{\partial p}{\partial s} = 0, \tag{7.1b}$$

$$\rho u^2 \frac{\partial \theta}{\partial s} + \frac{\partial p}{\partial n} = 0, \tag{7.1c}$$

$$\frac{\partial}{\partial s}\left(h + \frac{u^2}{2}\right) = 0, \quad \text{and} \tag{7.1d}$$

$$u \frac{\partial y_i}{\partial s} = \Omega_i, \tag{7.1e}$$

where the field variables (velocity, pressure, etc.) are functions of (s, n). The velocity in this coordinate system is by construction everywhere parallel to the s coordinate lines, and is denoted by its magnitude u and the direction θ. Restricting the equations (7.1) onto a streamline, the one-dimensional reaction zone structure equation (6.1) can be extended to handle quasi-one-dimensional geometries:

$$\dot{p} = -\frac{\rho u^2}{\eta} \left[\dot{\sigma} - u \frac{\partial \theta}{\partial n} \right] \tag{7.2a}$$

$$\dot{\rho} = -\frac{\rho}{\eta} \left[\dot{\sigma} - M^2 u \frac{\partial \theta}{\partial n} \right] \tag{7.2b}$$

$$\dot{y}_i = \mathcal{W}_i \frac{\dot{\omega}_i}{\rho} \tag{7.2c}$$

$$\dot{u} = \frac{u}{\eta} \left[\dot{\sigma} - u \frac{\partial \theta}{\partial n} \right] \tag{7.2d}$$

$$\dot{T} = \frac{T}{\eta} \left[\left(1 - \gamma M^2 \right) \dot{\sigma} - u M^2 \left(1 - \gamma \right) \frac{\partial \theta}{\partial n} - \frac{\mathcal{W} \eta}{\rho} \sum \dot{\omega}_i \right] \tag{7.2e}$$

Because the simple conservation relationship $\rho u = \rho_o D$ no longer holds as the stream-tube area is allowed to change, the fluid-particle acceleration $\dot{u}$ (7.2d), obtained using the conservation of mass (7.1a), is required.

The term $\partial \theta / \partial n$ above is a measure of streamline divergence. It can be expressed in terms of the streamtube cross-sectional "area" $A(s)$ as

$$\frac{\partial \theta}{\partial n} = \frac{1}{A} \frac{dA}{ds} \ . \tag{7.3}$$

When $A(s)$ is constant, (7.2) reduces to the one-dimensional ZND form given in (6.1). Using $d/dt = u \, d/ds$ and setting the thermicity coefficient to zero, (6.1) becomes the standard evolutionary equation for "quasi-one-dimensional" isentropic flow.

Similar to those of (6.1), the initial conditions $(\rho(0), p(0), \boldsymbol{y}(0), u(0))$ of (7.2) lie on the unreacted Hugoniot of some initial (pre-shock) state. The post-shock velocity is no longer strictly subsonic when oblique shocks are considered. To solve (7.2) requires a prescription of the area profile $A(s)$ or, equivalently, $u \partial \theta / \partial n$.

(a) Numerical Schlieren   (b) Water mass fractions
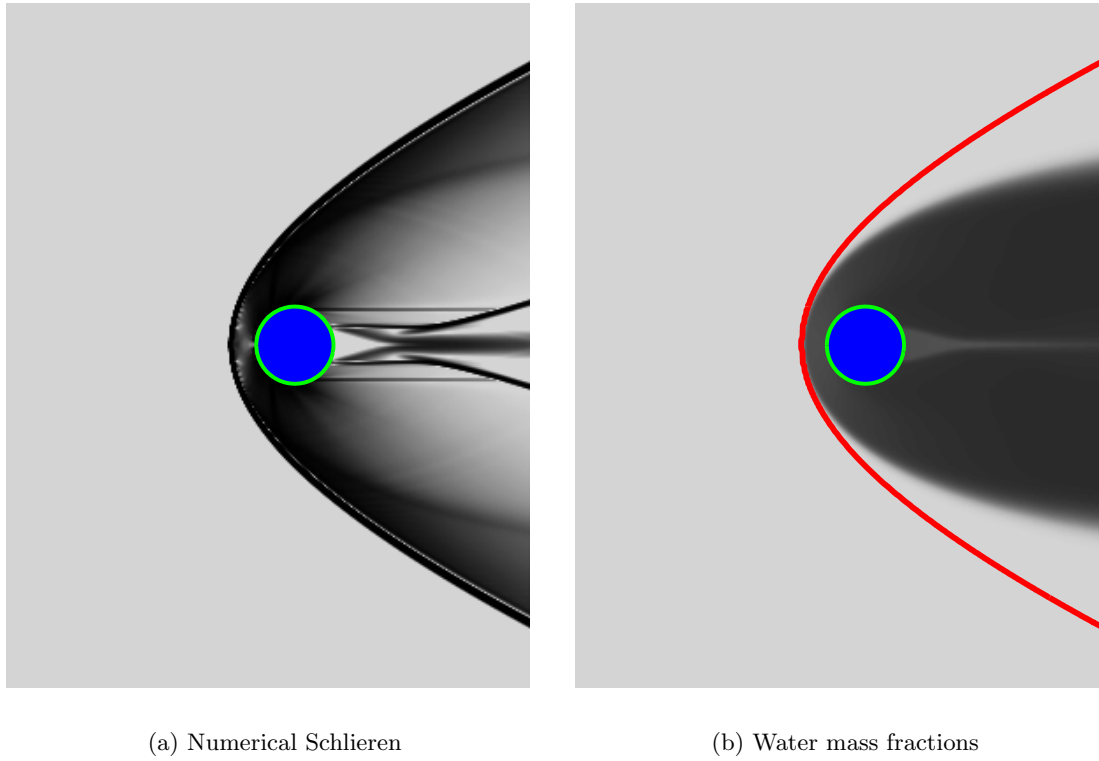
Figure 7.3: Numerical simulation of steady shock-induced combustion (k13 of Table 7.1). A numerical schlieren is shown in (a). A grayscale of water mass-fractions (b) clearly displays the non-reactive region. The maximum value of y(H_2O) is 0.066.

7.2 Shock-induced combustion

When the projectile's velocity is large enough to induce combustion at the stagnation pressure and temperature, a shock-induced supersonic combustion regime is possible. Figure 7.1(a) shows a schematic, and Figure 7.1(b) a shadowgraph, of such a configuration obtained by Kaneshige (1999). In the experiment, a spherical projectile 25.4 mm in diameter was shot into a stoichiometric Hydrogen-Air mixture at room temperature and a pressure of 42.1 kPa. The CJ induction zone length for this mixture was 0.38 mm and the CJ velocity was 1950 m/s. Two pertinent length scales of interest are the particle diameter d and the induction zone length Δ, which can be estimated by numerical integration of the ZND equations (6.1) with a detailed reaction mechanism. The ratio d/Δ for this experiment was 67.

It is expected that in such a configuration, a limiting shock angle β exists below which the bow shock is sufficiently oblique relative to the oncoming flow that no reaction occurs.

Simulation ID:	k13	k13x
Mixture Id:	Mixture C (Table 6.1)	
Overdrive f	1.8	
CJ Velocity	161787 cm/s	
Projectile Velocity u_p	217060 cm/s	
Projectile Diameter d	0.30 cm	
CJ Induction Zone Δ	0.15 cm	
Grid (nx,ny)	(300,300)	(256,256)
Domain (x,y)	(2.0 cm, 2.0 cm)	(1.7 cm, 1.7 cm)
Simulated Flight Distance	80 cm	52 cm

Table 7.1: Simulation parameters for cases k13 and k13x.

7.2.1 Numerical simulation with detailed chemistry

In this section, a numerical simulation of shock-induced combustion by a supersonic projectile using the Hydrogen-Oxygen mechanism (Table 1.1) is discussed.

Figure 7.3(a) is a schlieren image of the detailed kinetics numerical simulation of a 3 mm diameter cylindrical projectile in stoichiometric hydrogen and oxygen in 70% argon dilution at 298 K and 0.066 atm. The steady CJ induction zone length is 1.5 mm. The CJ velocity for this mixture is 1617.9 m/s and the projectile has a velocity of 2170.6 m/s. A 2 cm by 2 cm domain is covered with a uniform grid having 300 cells in each direction, resulting in 22 mesh cells per (CJ) ZND induction length. A symmetry boundary condition is used, and the simulation represents a channel 4 cm in height. The simulation is carried out in the projectile's frame of reference, and the calculation is run for a duration corresponding to a projectile flight length of 80 cm. The ratio d/Δ for the simulation is 2. The data from the simulation (case *k13* of Table 7.1) was lost after a disk crash. When rerun as case *k13x*, the simulation was set up to run for the same total time (or flight distance) but was terminated at 52 cm once the flow field has become visually steady (see the image sequence of Figure 7.4) in post-processing.

A numerical schlieren (from k13) is shown in Figure 7.3(a), and a grayscale plot for the mass fraction of water, which serves as a good indicator of reaction progress, is shown in Figure 7.3(b). The images are mirrored about the plane of symmetry in post-processing, as only the top half of the full channel is simulated.

The ratio of particle diameter to induction zone length differs significantly between the experiment ($d/\Delta = 67$) shown in Figure 7.1(b) and the simulation ($d/\Delta = 2$) out of necessity as the size of the domain is on the order of $10d$, while the grid size has to

be an order of magnitude smaller than Δ. Nevertheless, stabilized supersonic combustion exhibiting behavior strikingly similar to the experimental results of Kaneshige (1999) was observed. The main advantage of the detailed kinetics simulation is that it makes the entire flow field available at a high resolution for analysis.

7.2.2 The numerical procedure

The cylindrical projectile is modeled as a rigid-body defined as a closed-loop, discretized by 72 straight-line segments. The coupling is performed with the GEL algorithm of Arienti et al. (2003). The initial conditions, described next, are rather peculiar.

The simplest initial condition is to let a uniform inflow interact through GEL coupling with a stationary cylinder modeled by the rigid body. However, this is the numerical analogue of instantaneously accelerating the projectile to its final velocity u_p, and will very often cause the simulation to fail; the strong expansion wave rarefies the fluid behind the projectile, causing the pressure to go near vacuum and the temperature to drop out of range.

Two measures are taken to circumvent this problem. First, the particle is given a high, but finite, acceleration. Second, a one-dimensional CJ ZND solution whose shock-front is ahead of the projectile is set as the initial condition. Since the projectile is traveling at super-CJ velocity, the ZND wave gets "washed" back once the simulation starts. The high temperature of the ZND solution behind the projectile prevents the rarefaction from causing the temperature to fall out of bounds.

A sequence of frames from the simulation is shown in Figure 7.4. Flow is from left to right; the projectile moves to the right initially, and becomes stationary when it reaches its final speed.

From Figure 7.5, it can be observed that fluid particles will have one of three distinct fates after passing through the shock: no reaction, supersonic reaction, and subsonic-to-supersonic transition with reaction. Representative streamlines for each of the aforementioned fates are labeled (a), (b) and (c), respectively, in Figure 7.5.

7.2.3 Nonreactive streamline

In this section, the properties following streamline (a) of Figure 7.5 are discussed. This analysis was performed before the disk crash and corresponds to case k13 of Table 7.1.

$x = 0$ cm

$x = 1$ cm

$x = 2$ cm

$x = 3$ cm

$x = 4$ cm

$x = 5$ cm

$x = 6$ cm

$x = 7$ cm

$x = 8$ cm

$x = 9$ cm

$x = 12$ cm

$x = 15$ cm

$x = 20$ cm

$x = 30$ cm

$x = 40$ cm

$x = 52$ cm
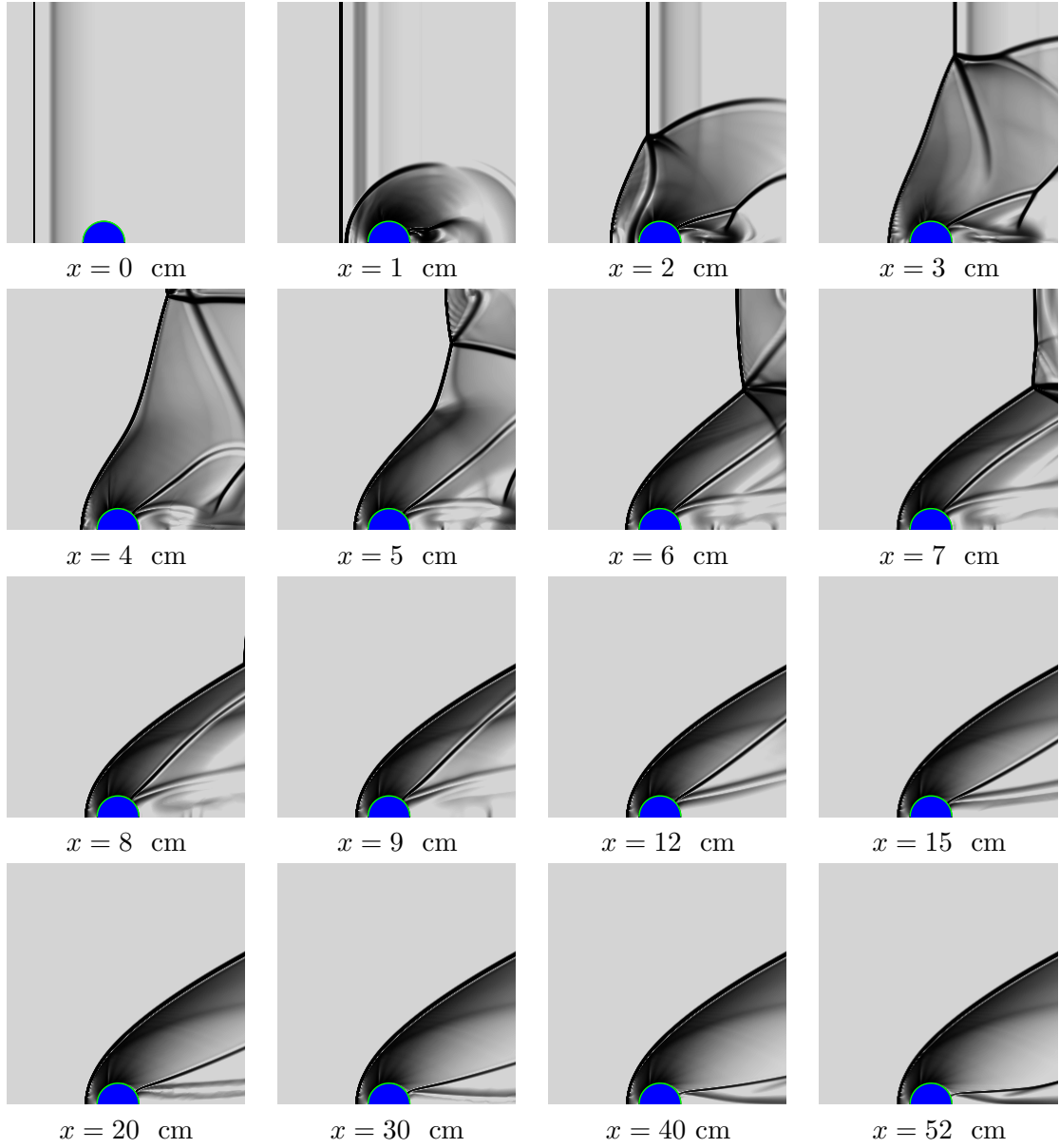
Figure 7.4: Image sequence for case k13 of Table 7.1.
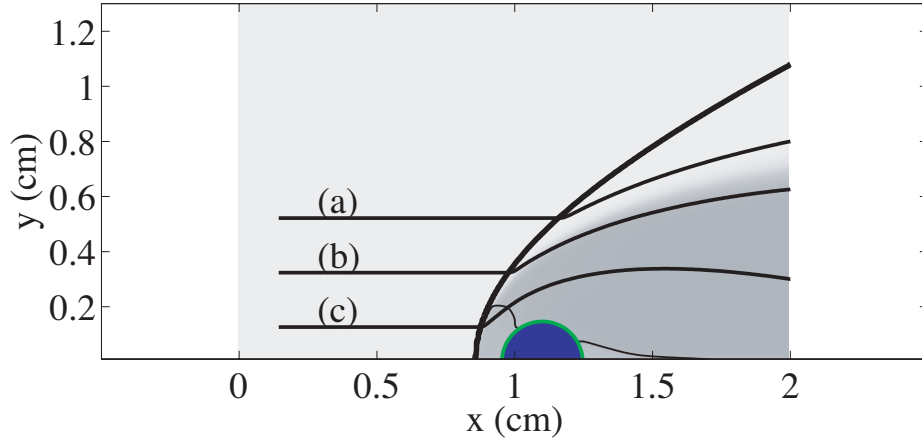
Figure 7.5: Three streamlines in shock-induced combustion. Streamline (a) undergoes no apparent reaction. Both streamlines (b) and (c) are reactive with streamline (c) exhibiting subsonic-to-supersonic transition when crossing the sonic locus.

The pressure, temperature, density and velocity profiles of the flow field, nondimensionalized by the freestream values and interpolated onto the streamline (a) of Figure 7.5, are shown in Figure 7.6. The mass fraction of water along this streamline has a maximum value of less than 0.04%, two orders of magnitude smaller than its equilibrium ZND value (at the CJ point) of 8.7%.

Once the fluid-particle passes through the bow shock, the flow along the unreactive streamline is isentropic. As a result, the preshock state, shock angle β, and area variation of the streamtube completely determine the thermodynamic states along the streamline. Without making the perfect gas assumption of constant specific heats, an algebraic *area Mach number relation* cannot be written in closed form and requires a numerical solution, the recipe is given in Algorithm 7.1.

Using the isentropic relationship, the state along an unreactive streamline can be computed once the streamtube area variation is known. This variation can be obtained with relatively high accuracy using data interpolated on the streamline, as no numerical differentiation is necessary. From the conservation of mass, we get

$$\frac{A(s)}{A_o} = \frac{\rho_o D}{\rho(s)u(s)} \ .$$ (7.4)

Using (7.4) and the computed values of ρ and u interpolated onto the streamline, the streamtube area ratio (for streamline (a) of Figure 7.5) is obtained as a function of the
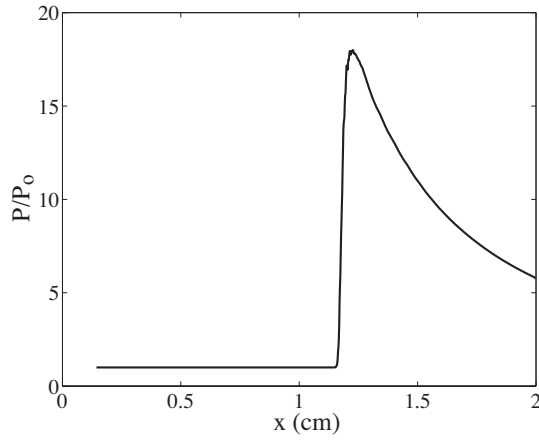
(a) Pressure
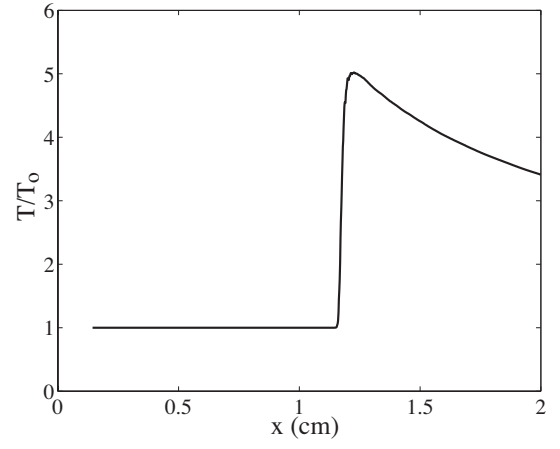
(b) Temperature
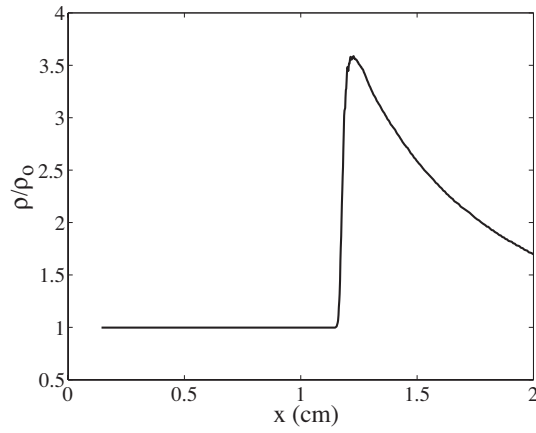
(c) Density
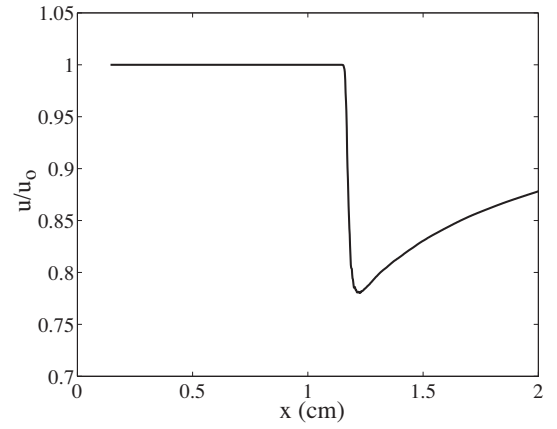
(d) Speed

Figure 7.6: Nondimensional profiles as a function of x axis coordinate position interpolated onto streamline (a) of Figure 7.5.

---

definitions:

Stagnation Enthalpy: $H = h(T_o) + \frac{u_o^2}{2}$

$err = s(T, p) - s_o$

input: $\rho_o, p_o, T_o, u_o, \boldsymbol{y}, A/A_o$

Compute entropy and stagnation enthalpy, to be held constant.

Find velocity u that satisfies conservation exactly, and isentropy approximately:

(1) Guess u^* using perfect gas relationship.

(2) Compute $\rho^* = \rho_o u_o \frac{A_o}{A}$ using conservation of mass.

(3) Compute $h^* = H - \frac{u^{*2}}{2}$.

(4) Solve for T^* : $h(T^*) = h^*$, then get ρ^* with equation of state.

(5) Iterate on u^* to render entropy error err to zero.

With converged u, compute thermodynamic properties.

return: u, P, T, etc. as a function of A/A_o.

Algorithm 7.1: Solution procedure for real gas isentropic flows.

(a) Streamtube Area Ratio

(b) Piecewise-linear Fit
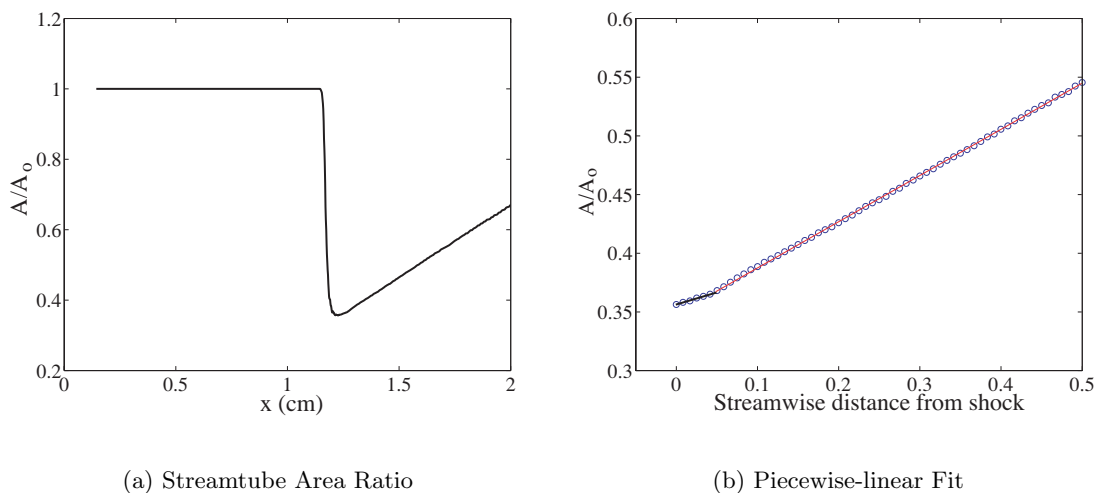
Figure 7.7: The streamtube area-ratio A/A_o plotted as a function of the streamline's x-axis position (a), and its piecewise-linear fit (b).

position on the x-axis, shown in Figure 7.7(a). Defining the post-shock point to be point $s = s^*$ where $A(s)/A_o$ is at a minimum, the post-shock portion $A(s \geq s^*)/A_o$ is plotted, now as a function of streamwise distance from s^*, in Figure 7.7(b).

Using the procedure given in Algorithm 7.1 with the function $A(s)/A_o$ obtained from (7.4), the thermodynamic state on the streamline can be computed pointwise, relative to the base (post-shocked state) at s^*. Alternatively, the evolution of the thermodynamic state can be determined by solving the evolutionary equation in (7.2). As seen in Figure 7.7(b), the area-ratio is an approximately piecewise-linear function of distance on the streamline. Fitting the profile enables the determination of $\partial\theta/\partial n$ via (7.3) needed in (7.2).

The predicted temperature and pressure profiles, normalized by the post-shock state P^* and T^* defined previously, are plotted in Figure 7.8. Figure 7.8(a) shows T and P computed as a function of the area ratio interpolated on the streamline using Algorithm 7.1, and plotted as a function of the x-coordinate position.

Figure 7.8(b) shows T and P computed using the evolutionary equation (7.2), with initial conditions obtained by solving the shock-jump condition across the oblique shock, with a shock angle determined by differentiating the fitted shock profile. A piecewise-linear approximation of the area profile $A(s)/A_o$ is used for the area-divergence terms in (7.2), and the profiles are plotted along the streamwise coordinate s. This approach will be used later to analyze the steadiness of reactive, hence non-isentropic, streamlines.
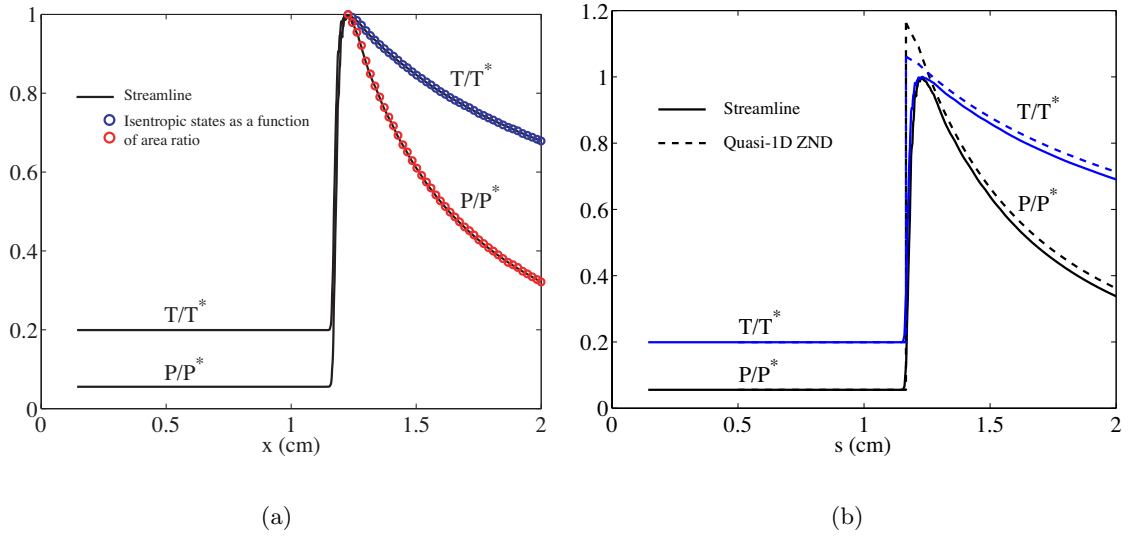
Figure 7.8: Temperature and pressure evolution after the shock, normalized by the post-shock value T^* and P^*, are computed with Algorithm 7.1 (a) and with the quasi-one dimensional ZND model (b).

7.2.4 Reactive streamlines

The projectile simulation (k13 of Table 7.1) discussed previously in this section was rerun, because of a disk failure, with a tighter domain having less wasted space in front of and above the projectile. The new domain is covered by a uniform mesh 256 cells by 256 cells with each side measuring 1.7 cm. A symmetry boundary condition is used on the bottom, and the simulation represents a channel that is 3.4 cm in height. This is case k13x of Table 7.1.

The last timestep of the simulation showing a gray-scale plot of the water mass fraction, reflected about its symmetry plane, appears in Figure 7.9(a). The sonic line, typical of supersonic flows over blunt bodies, is shown both in front of and behind the circular projectile. The upper streamline is the *CJ streamline*, which crosses the shock at the CJ angle. Streamline (b) is a representative for supersonic combustion, to be discussed later. Streamline (c) is also reactive and, in addition, undergoes subsonic to supersonic transition. The thermicities $\dot\sigma$ from (6.3) along these three streamlines are computed and plotted as functions of their x-coordinate positions in Figure 7.9(b).

The leading shock is reoriented so it is concave up with its nose shifted to the origin, as shown in Figure 7.10. A least-square polynomial is fitted to the shock and its first derivative,

(a) Water mass-fractions

(b) Thermicity along streamlines
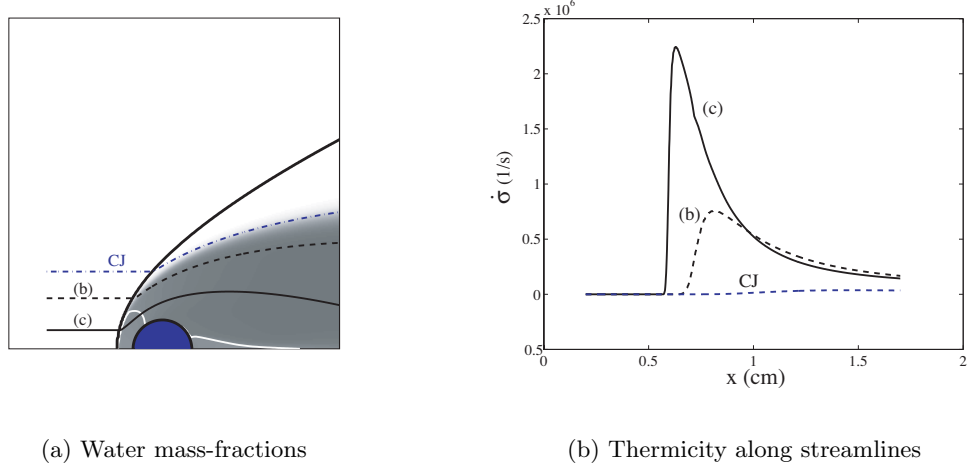
Figure 7.9: A greyscale image of the mass fraction of water, indicative of reaction progress, is shown in (a). The streamline marked "CJ" crosses the shock at the CJ angle while the streamline *(b)* is representative of supersonic combustion. Streamline *(c)*, in addition to being reactive, also undergoes subsonic to supersonic transition. The thermicities $\dot{\sigma}$ along the three streamlines are plotted in (b).
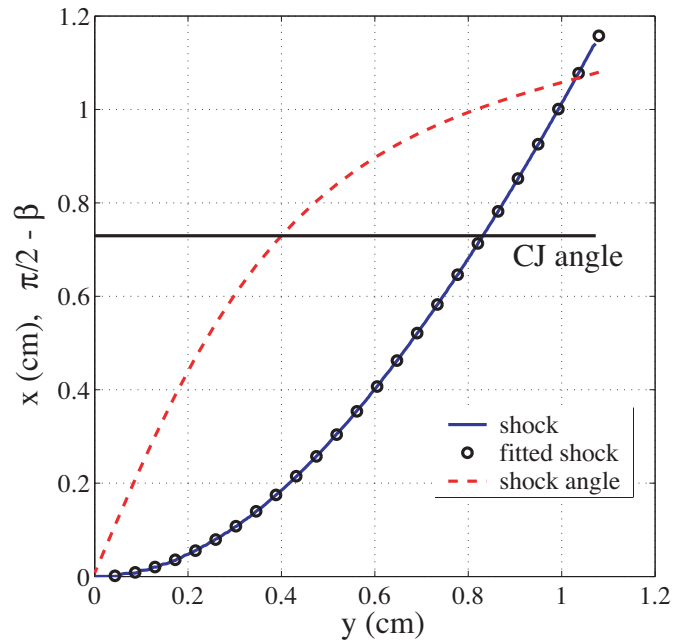
Figure 7.10: The leading shock is shown reoriented and fitted. The intersection of the dashed line (the first derivative) and the stepped line indicates the location where the shock passes through the CJ angle. The ordinate axis is in centimeters for the shock and radians for the angles.

(a) Streamtube Area Profile

(b) Nondimensional Profiles on Streamline
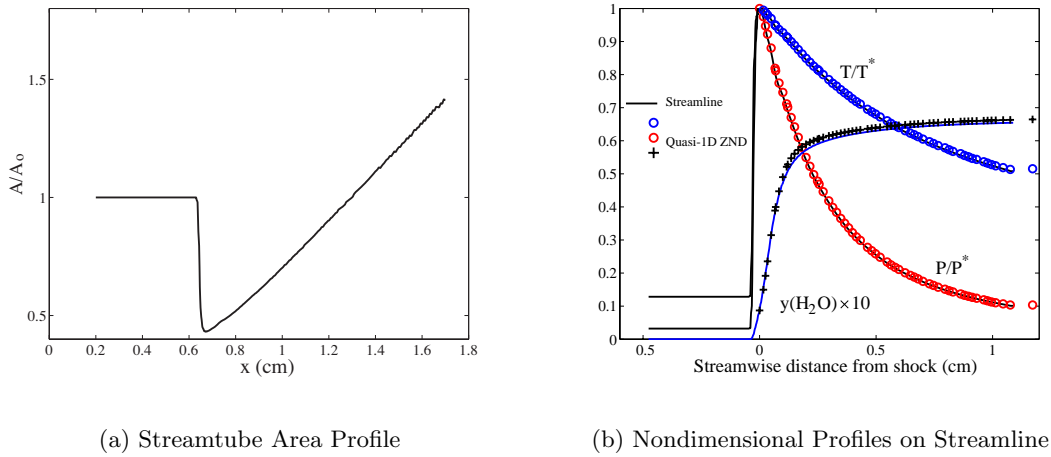
Figure 7.11: The streamtube area profile $A(s)/A_o$ for the reactive streamline shown in Figure 7.9 is in (a), as a function of x-axis position. The temperature and pressure, interpolated onto the streamline from the full CFD simulation and normalized by the post-shock values, are shown as the solid lines in (b). The symbols are obtained by solving the quasi-one-dimensional ZND equations in (7.2).

equal to $\tan(\pi/2 - \beta)$, is shown dashed. Its intersection with the stepped line indicates the location at which the shock crosses the CJ angle $\beta = \arcsin(1/\sqrt{1.8})$.

The area profile $A(s)/A_o$ of the infinitesimal streamtube is computed, using (7.4), for streamline (b) of Figure 7.9(a). Together with an initial condition from the post-shock state interpolated onto the streamline, the evolution of all properties on the streamline behind the shock can be computed by numerical solution of (7.2). This solution is compared against the solution from the full CFD calculation in Figure 7.11.

The temperature and pressure profiles interpolated onto the streamline, normalized by their respective post-shock values, are shown as the solid lines in Figure 7.11(b). The numerical solutions of the quasi-one-dimensional ZND equations in (7.2), are shown as symbols on the plot. Their close agreement indicates that the transient CFD solution has reached steady state. While the pressure is expected to decrease behind the von Neumann point for a net-exothermic reaction, the temperature should *rise*, a rise that is clearly missing from the plot.

The reason for the missing rise is that the temperature increase due to reaction has been overwhelmed by the cooling effect due to quenching. We have already seen from Figure 7.11(b) that the quasi-one-dimensional ZND solution tracks the CFD solution well,
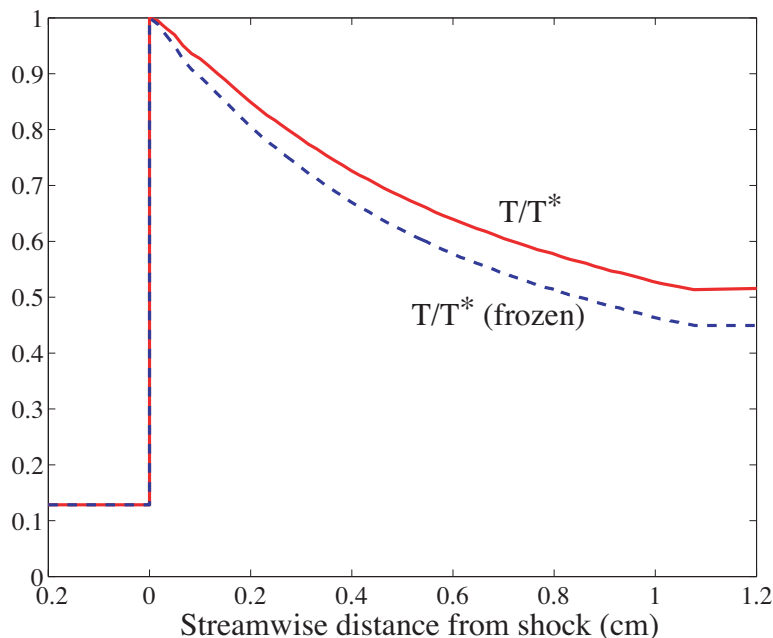
Figure 7.12: Temperature along streamline (b) of Figure 7.9(a). The upper line is the nondimensional temperature obtained from solving the quasi-one-dimensional ZND solution (as seen in Figure 7.11(b)). The line marked *frozen* is obtained by solving the quasi-one-dimensional equations with the reactions turned off.

we can now compute the temperature evolution along the same streamtube at frozen (free-stream) composition. These two solutions are plotted in Figure 7.12. The heat release from chemical reactions accounts for the difference between the two solutions.

7.2.5 Transonic reactive streamline

Figure 7.13(a) shows the Mach number and the area ratio along a streamline that crosses the sonic point (streamline (c) of Figure 7.9(a)). For quasi-one-dimensional (frictionless, adiabatic) unreactive flows, transitions from subsonic to supersonic can occur only at a throat, where the area is at a local minimum. In the presence of chemical reactions (see (7.2)), this "sonic throat" occurs at the point where the total contribution of area change and heat release, $\dot{\sigma} - u\partial\theta/\partial n$, vanishes. For the present numerical simulation, Figure 7.13(a) shows that gasdynamics effects dominate as the streamline crosses the sonic point at the throat area. Figure 7.13(b) shows the evolution of temperature, pressure and the mass fraction of water along the streamline. The symbols on the figure indicates the location of the subsonic-supersonic transition. Because of this transition, numerical solutions of the

(a) Mach number and area ratio

(b) Nondimensional profiles on streamline
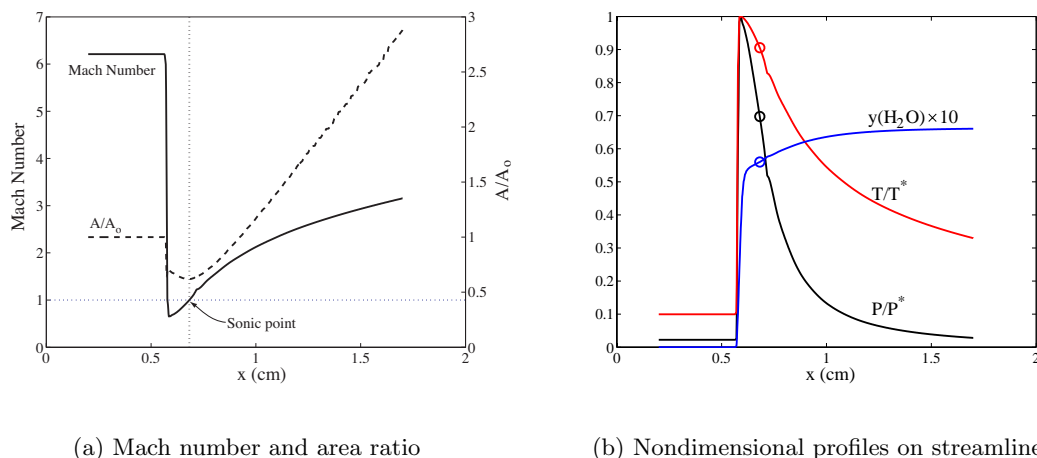
Figure 7.13: (a) Mach number and area ratio of a streamline that crosses the sonic line. The cross hair indicates the location of the sonic point aft of the shock. (b) Nondimensional temperature and pressure and water mass fraction for streamline (c) in Figure 7.9(a).

quasi-one-dimensional equations (7.2) are difficult to obtain as a precise knowledge of the streamtube-area profile is required to avoid the singularity at the sonic point.

7.2.6   The need for reduced chemistry

To be able to simulate conditions commensurate with experiments, the size of the projectile (d) needs to be much larger than the order of the half-reaction zone length (Δ). In the experiments of Kaneshige (1999), the ratio d/Δ often exceeds 100. Unfortunately, achieving this ratio is very difficult for the Argon-diluted Hydrogen-Oxygen mixture used in the above simulations. This mixture (Table 6.1), chosen for its stability properties, has a very long reaction zone behind the induction region (see Figure 6.1). This reaction zone is on the order of 10 times the size of the 0.15 cm induction zone, and using a minimum of 10 cells across the induction zone means 100 control volumes per Δ, or 10000 control volumes per projectile diameter to achieve $d/\Delta = 100$!

In order to model and predict detonation initiation, a very accurate calculation of the early (high dimensional, in the context of ILDM) transients near the von Neumann point is critical, discouraging the use of ILDM reduced chemistry.

The impropriety of using the ILDM in the induction region is further complicated by the expansion behind the projectile, which not only quenches the fluid but also increases the
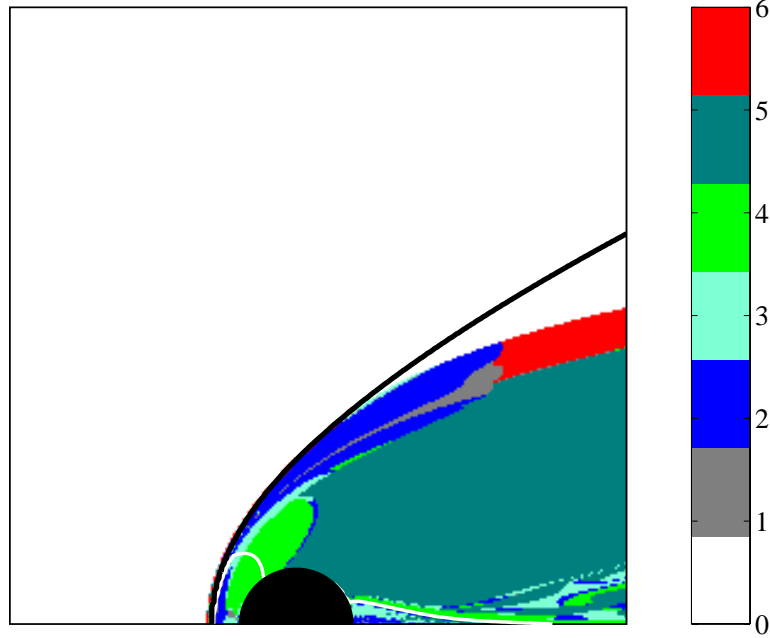
Figure 7.14: The ILDM dimensions for k13x.

ILDM dimension. A map of the computed ILDM dimensionality for the flow field is shown in Figure 7.14. These reasons, and the need to simulate a much larger domain, motivate the switch to simplified chemistry that is described in the next section.

7.3   One-step irreversible chemistry

For the remainder of this chapter, a perfect-gas, single-step irreversible reaction model is used. Assume that a binary perfect-gas mixture consists of two components (A, B) having the same molecular weight, connected by the single irreversible reaction $A \to B$. Letting their heat capacities be equal (and constant), the equation of state of the mixture is

$$Pv = RT \tag{7.5a}$$

$$e = RT/(\gamma - 1) - \lambda q , \tag{7.5b}$$

where λ denotes the fraction of the product B and q is the heat of the reaction. The first-order Arrhenius form is chosen for the reaction rate,

$$\frac{d\lambda}{dt} = k(1 - \lambda) \exp\left(-E_a/RT\right) . \tag{7.6}$$

Following Eckett (2001), the thermodynamic quantities are nondimensionalized by the free-stream values P_o, T_o, ρ_o:

$$\tilde{\rho} = \frac{\rho}{\rho_o} \qquad \tilde{P} = \frac{P}{P_o} \qquad \tilde{T} = \frac{T}{T_o}$$

And the other properties are

$$\tilde{e} = \frac{e}{RTo} \ , \qquad\qquad \tilde{E}_a = \frac{E_a}{RT_o} \ , \qquad \tilde{q} = \frac{q}{RT_o} \ ,$$

$$u_{ref} = \sqrt{RTo} \ , \quad \text{and} \quad \tilde{u} = \frac{u}{u_{ref}} \ .$$

Defining the length scale by the half-reaction length $\Delta_{1/2}$, the distance behind a CJ shock wave at which the progress variable $\lambda = 0.5$,

$$t_{ref} = \frac{\Delta_{1/2}}{u_{ref}} \ , \quad \tilde{t} = \frac{t}{t_{ref}} \ , \quad \text{and} \quad \tilde{x} = \frac{x}{\Delta_{1/2}} \ . \tag{7.7}$$

Finally the nondimensional equation of state becomes

$$\tilde{P}\tilde{v} = \tilde{T} \quad \text{and} \tag{7.8a}$$

$$\tilde{e} = \tilde{T}/(\gamma - 1) - \lambda\tilde{q} \ , \tag{7.8b}$$

and the nondimensional rate law is

$$\frac{d\lambda}{d\tilde{t}} = \tilde{k}(1 - \lambda)\exp\left(-\tilde{E}_a/\tilde{T}\right) \ , \tag{7.9}$$

where the rate constant $\tilde{k}$ is chosen such that $\lambda = 0.5$ at $\tilde{x} = 1$.

For notational simplicity, the tildes will be omitted and all variables will be understood to be nondimensionalized for the remainder of this chapter.

7.4   Straight oblique detonation wave

When the detonation wave is straight and oblique, the quasi-one-dimensional ZND equations of (7.2) reduce to the one-dimensional equations of (6.1). Details can be found in Shepherd (1994). A schematic of an idealized straight oblique detonation wave is shown in Figure 7.15.
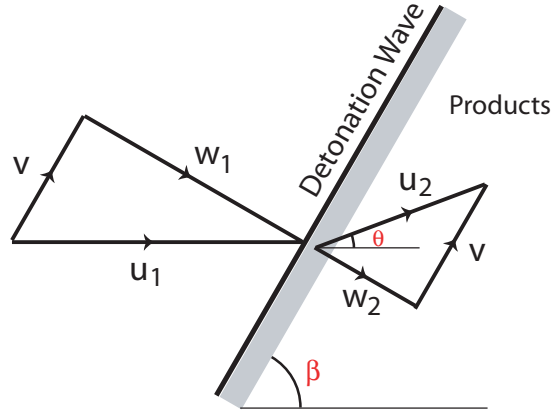
Figure 7.15: Schematic of an idealized straight oblique detonation wave.

The angle of the streamline for a straight oblique detonation wave is

$$\theta = \beta - \arctan\left(\frac{w}{v}\right) \ , \tag{7.10}$$

where the tangential velocity v is constant, and the normal velocity w evolves according to

$$\dot{w} = w\frac{\dot{\sigma}}{\eta_n} \ . \tag{6.1d}$$

Differentiating (7.10),

$$\dot{\theta} = \frac{-v}{v^2 + w^2}\dot{w} \ . \tag{7.11}$$

Substituting (6.1d) into (7.11),

$$\dot{\theta} = -v\frac{w}{v^2 + w^2}\frac{\dot{\sigma}}{\eta_n} \ , \tag{7.12}$$

and rearranging (7.10) and substituting into the above,

$$\dot{\theta} = -\frac{v}{w}\sin^2(\beta - \theta)\frac{\dot{\sigma}}{\eta_n} \ . \tag{7.13}$$

Then using (7.10) again, rearranged to $v = w/\tan(\beta - \theta)$, the streamline curvature from obliquity and chemical reaction is

$$\dot{\theta} = -\frac{1}{2}\sin 2(\beta - \theta)\frac{\dot{\sigma}}{\eta_n} \ , \tag{7.14}$$

or

$$u\frac{\partial\theta}{\partial s} = -\frac{1}{2}\sin 2(\beta - \theta)\frac{\dot{\sigma}}{\eta_n} \ . \tag{7.15}$$

Note the factor of $1/2$ and u missing in Eq (39) of Shepherd (1994). In addition, translational invariance along the straight-wave gives (see Eq (26) in Shepherd, 1994)

$$\frac{\partial}{\partial n} = \frac{-1}{\tan(\beta - \theta)}\frac{\partial}{\partial s} \ . \tag{7.16}$$

Substituting (7.15) into the above, the differential relationship for streamtube divergence due to obliquity and chemical reaction is

$$u\frac{\partial\theta}{\partial n} = \cos^2(\beta - \theta)\frac{\dot{\sigma}}{\eta_n} \ . \tag{7.17}$$

Using (7.17), it can be verified that the quasi-one-dimensional ZND equations of (7.2) reduce to the one-dimensional set in (6.1).

7.4.1   Trajectory through a straight oblique detonation

In this section, an algorithm for computing the curved trajectory of a fluid particle through a straight oblique detonation wave (Algorithm 7.2) is presented. It is the basis for determining the profile of the *streamline wedge* discussed in §7.4.2.

definitions:

Shock Angle: $\beta = \arcsin(1/\sqrt{f})$

Flow Velocity (preshock) : u_o

Velocity (Tangential Component) : v

Velocity (Normal Component, postshock) : $w(t)$

input: f, and the normal ZND solution

Compute $v = u_o/\cos\beta$, to be held constant

Get $w(t)$ from solution of (6.1), the normal ZND equations.

Get $x(t)$, and $y(t)$ (see Figure 7.16)

(1) $x(t)$ is the particle's position in the normal direction from the normal ZND solution.

(2) $y(t) = v * t$, v is constant

Get $x'(t)$ and $y'(t)$ by rigid rotation

(1) $r(t) = \sqrt{x(t) + y(t)}$ and $\alpha(t) = \arctan(y(t)/x(t)) - (90 - \beta)$

(1) $x'(t) = r(t)\sin(\alpha(t))$ and $y'(t) = r(t)\cos(\alpha(t))$.

return: $x'(t)$ and $y'(t)$

Algorithm 7.2: Particle trajectory through a straight oblique detonation wave.
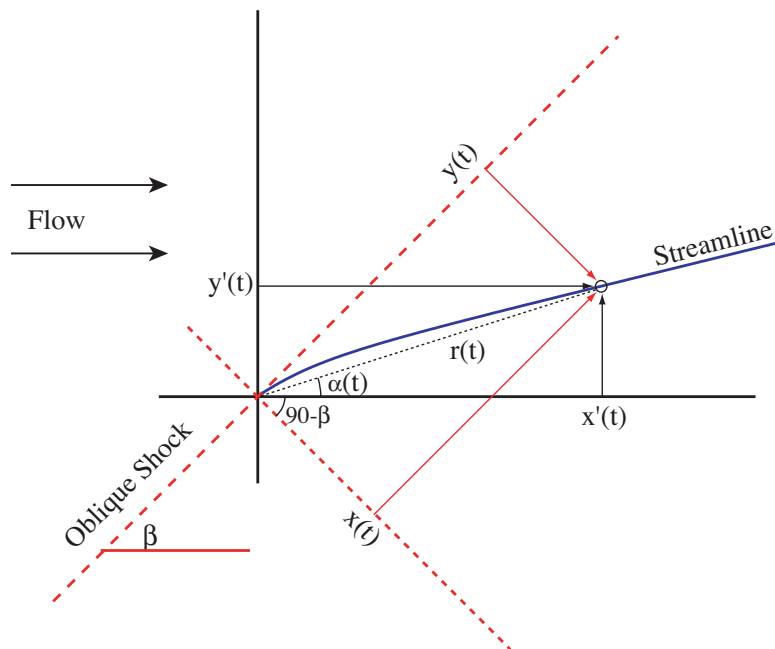
Figure 7.16: Streamline for an idealized oblique detonation.

7.4.2 Numerical simulation of straight oblique detonation

For a projectile traveling at a supersonic Mach number M, the strength of an inert bow shock decays smoothly from the nose to an acoustic disturbance inclined at the Mach angle $\sin^{-1}(1/M)$ away from the projectile. In contrast, a successfully initiated detonation wave is observed to decay from a normal-incident overdriven detonation to an oblique detonation inclined at the CJ angle $\sin^{-1}(M_{CJ}/M)$. Such a wave is characterized by its shock angle β and the flow deflection angle θ, and a schematic is shown in Figure 7.15.

Supersonic flow over a wedge provides a convenient means to realize a steady oblique detonation. The requirements are that the incoming flow velocity must be greater than the CJ velocity, and that the wedge's profile must be compatible with flow deflection due to the combined effect of the shock and the chemical reaction under the ZND model. Numerical simulations of straight oblique detonations have been studied by Grismer and Powers (1996), who focused on the detonation stability over flows of curved wedges, and by Pratt et al. (1991), who studied the attachment and stability of oblique detonation waves over wedges of various angles.

Most of the result that follows is based on the mixture P1, chosen to have the same equation of state as the defined in Case B of Table 2.1 of (Eckett, 2001), albeit with an

	Case	P1	P2
Independent quantities	γ	1.4	1.4
	q	12	12
	E_a	15	30
Dependent quantities	k	16.1	284.
	U_{CJ}	5.08	5.08
	U_{vN}	1.08	1.08
	$M_{0_{CJ}}$	4.29	4.29
	$M_{0_{vN}}$	0.428	0.428
	E_a/T_{vN}	3.32	6.64
	P_{vN}	21.3	21.3
	P_{CJ}	11.2	11.2
	T_{vN}	4.52	4.52
	T_{CJ}	6.76	6.76

Table 7.2: Parameters and properties of the mixtures P1 and P2

E_a/T_{vN} that is slightly lower to ensure longitudinal stability of a planar CJ detonation.

For an exothermic reaction, the normal component of the post-shock velocity w_2 increases continuously as the density decreases from a maximum at the von Neumann point. The flow deflection θ decreases from a maximum at the shock and reaches a minimum at equilibrium ($\lambda = 1$). A shock and detonation polar for an incoming flow, with an overdrive $f = 2$ for the mixture P1 described in Table 7.2, is shown in Figure 7.17. The oblique wave analogue of the Rayleigh line, encapsulating the conservation of mass and momentum, is the Rayleigh curve (see Shepherd, 1994). The Rayleigh curve corresponding to the CJ wave angle $\beta = 45°$ is shown as the dashed line in Figure 7.17. The intersection of the Rayleigh curve with the shock Hugoniot (the upper line) is the von Neumann point. The reaction proceeds downwards along the Rayleigh line towards the CJ point, the lower intersection with the equilibrium Hugoniot.

Unlike an inert oblique shock, the profile of the wedge that is compatible with a straight oblique ZND detonation wave is curved. The profile of this wedge can be computed by solving the ZND equations (6.1). The procedure used is described in Algorithm 7.2. Once this profile is obtained, it is discretized by straight-line segments to represent the solid boundary for the reactive flow simulation, using the Ghost-fluid Eulerian Lagrangian coupling algorithm of Arienti et al. (2003).

A steady oblique detonation wave, with an incoming flow velocity corresponding to an overdrive factor f of 2, is shown in Figure 7.18(a). The marker on the upper left corner
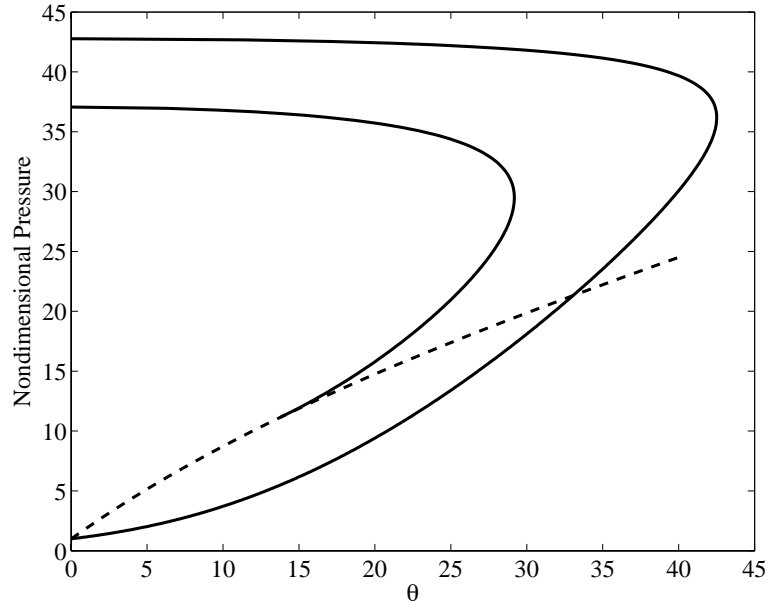
Figure 7.17: Shock and detonation polars for the mixture P1 described in Table 7.2 with an upstream velocity of $\sqrt{2}U_{CJ}$ (i.e., $f = 2$) are plotted as the lower and upper solid line, respectively. The Rayleigh curve for a CJ detonation, corresponding to an oblique wave with a wave angle $\beta = 45°$, is shown as the dashed line.

indicates the size of $\Delta_{1/2}$ used to normalize distances (see (7.7)). Line II is the locus of the half-reaction. The simulation is performed on a uniform 600x600 grid covering a domain that is 20 units by 20 units, with 30 cells per half-reaction zone. The analytical shock angle is $\beta = 45°$.

Translation invariance along the direction of the oblique wave means that all gradients in the direction of the wave vanish (see Shepherd, 1994). Line III in Figure 7.18(a), slanted at the exact shock angle, will be used later when discussing the coupling scheme. The dashed line (S) in the figure is a streamline obtained from Tecplot by integrating the velocity field. The pressure and temperature are interpolated onto the streamline and plotted against the exact ZND model in Figure 7.19(a) as a function of streamwise distance. The exact values can be obtained in various ways.

One approach is to solve the one-dimensional ZND equations in (6.1), producing results that are a function of the distance *normal* to the oblique shock, with which the streamline distance can be obtained.

Another approach that gives the same result, but avoids the numerical solution of a system of ODE (given by (6.1)), is to solve for the intersection of the Rayleigh line and

(a) Oblique Detonation Wave

(b) Nonreactive Curved Shock
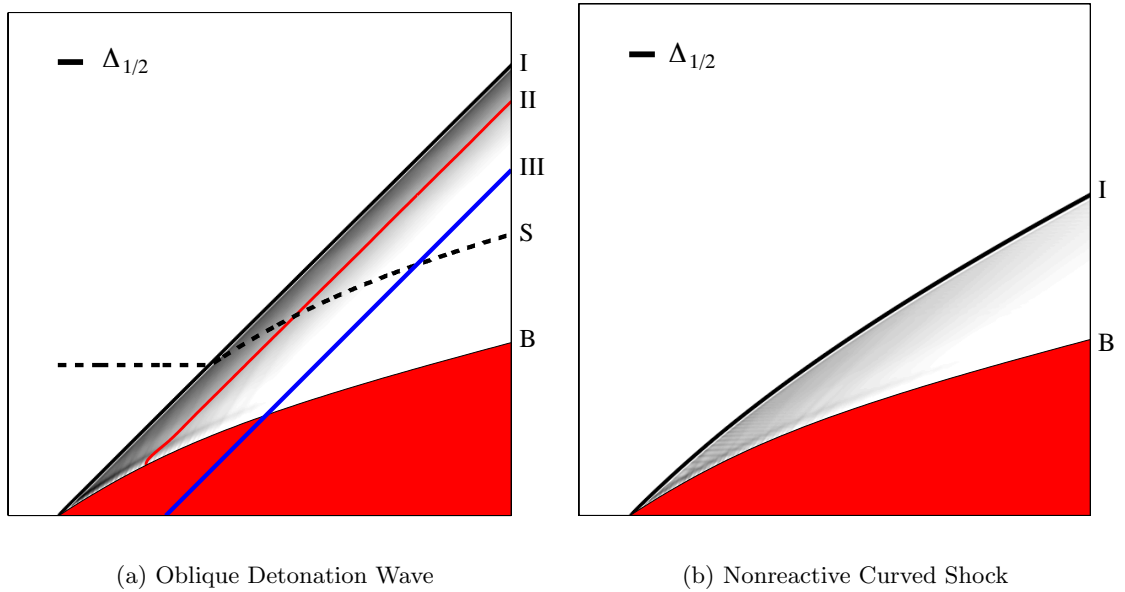
Figure 7.18: Numerical Schlieren of an oblique detonation wave over a streamline-shaped wedge is shown in (a). Line I is the leading shock, II is the locus of half reaction $\lambda = 0.5$. Line III is an interpolation line oriented at $45°$, 3 length units away from the leading-shock (I) in the direction normal to the shock. An inert flow field over the same wedge is shown in (b).

the partial-reaction Hugoniot equations to get state properties as a function of reaction progress λ. This can then be used to simplify the evolutionary equation to $\dot{\lambda} = f(\lambda, T(\lambda))$ (see Fickett and Davis, 1979).

The nondimensional pressure and temperature profile interpolated onto the streamline in Figure 7.18(a) is compared against the one-dimensional model in Figure 7.19(a). Their close agreement is an indication that the transient simulation is at steady-state.

It is worth noting that this simulation can serve as a benchmark problem for the Ghost-fluid Eulerian-Lagrangian coupling scheme, in addition to the ones already discussed in Arienti et al. (2003). Translational invariance of the flow along a straight oblique shock allows the exact solution of the two-dimensional flow field to be simplified to a function of distance normal to the straight oblique wave.

To illustrate, the temperature and density 3 units downstream of the oblique shock in the normal direction are interpolated from the two-dimensional grid and plotted against the exact solution in Figure 7.20(b). The leading shock, as well as the interpolation line 3 units in the normal direction downstream, is shown in Figure 7.20(a). The grey area beneath

(a) Temperature and Pressure   (b) Thermicity
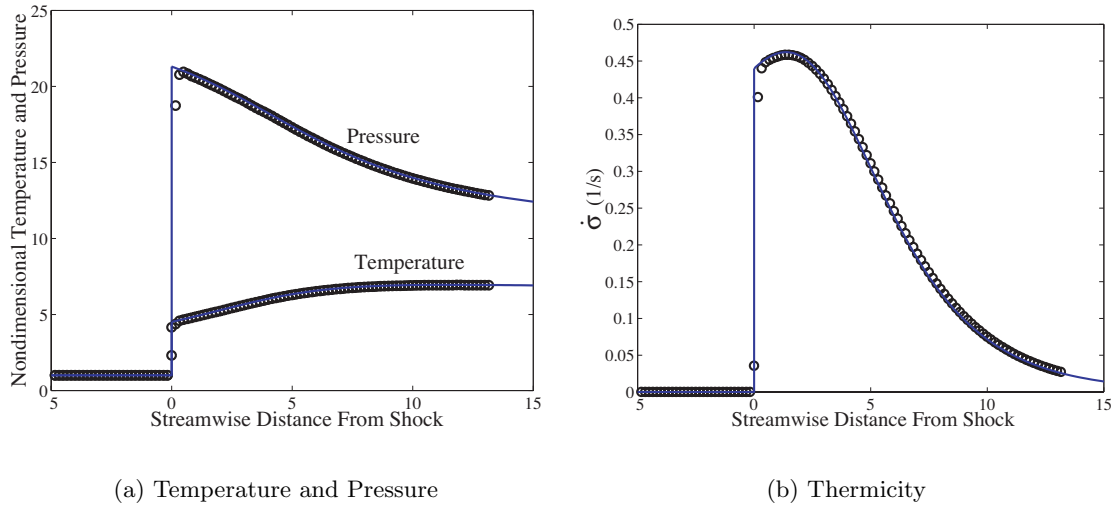
Figure 7.19: The nondimensional temperature and pressure evolution (a) and the thermicity $\dot{\sigma}$ (b) along a streamline through an oblique detonation. Symbols are interpolated from the 600x600 CFD domain and solid lines are computed with a one-dimensional ZND model.

Run ID:	b3	b7d	b7dn2
domain (x,y)	(50,100)	(50,100)	(30,45)
grid (nx,ny)	(500,1000)	(500,1000)	(320,480)
overdrive f	2.0	1.4	1.4
Mixture EOS	P1	P1	P1
Projectile Length	10.0	5.0	5.0
Simulated Flight Distance	400	980	840
Image Sequence	Figure 7.37	Figure 7.38	Figure 7.39

Table 7.3: Simulation parameters for streamline-shaped projectiles (cases b3, b7d and b7dn2).

the wedge's surface is an approximate representation of the extent of the ghost region. In Figure 7.20(b), the interpolated profiles are plotted as a function of y and the vertical line demarcates the location of the solid boundary. It can be seen that away from the boundary, the CFD solutions and the exact solutions are in close agreement.

7.4.3 Streamline-shaped projectiles

A truncated wedge can be used, instead of the full streamline, as a solid boundary for the reactive fluid to flow over. In fact, such a wedge becomes a sharp-pointed projectile for which a straight attached oblique detonation can be initiated.

The simulation shown in Figure 7.21 (case b3 of Table 7.3) exhibits successful initiation

(a) Interpolation Line

(b) Temperature and Pressure Profiles
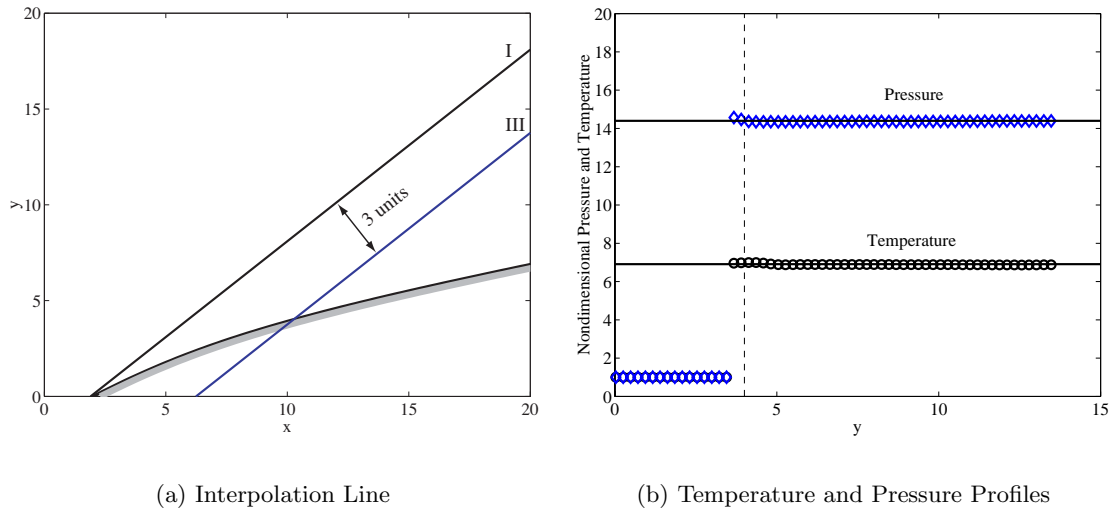
Figure 7.20: Comparison between the CFD and the "exact" temperature and pressure solution. The leading shock and the interpolation line parallel to the shock 3-units downstream are shown in (a). The grey area under the wedge's surface illustrates the approximate thickness of the ghost region used by the boundary coupling scheme.

of an attached oblique detonation by a projectile, a solution which is not possible with blunt nosed projectiles (cylinders and spheres).

A sequence of frames for this case is shown in Figure 7.37. The domain is very tall, in order to avoid shock reflection at the top boundary. A CJ detonation wave solution originally ahead of the projectile is used as the initial condition, as discussed in §7.2.2. Because the projectile travels at super-CJ speed ($f = 2$), and the simulation is carried out in the projectile's frame of reference, the CJ-detonation gets washed back and leaves the domain after the projectile has traveled roughly 160 units distance.

One difficulty encountered when the overdrive f is lowered is that the CJ detonation painted in as initial condition will not leave the domain using simple zero-gradient outflow boundary conditions. This can be observed in the image sequence of Figure 7.38.

When $f = 1.4$, the steady solution has an apparent dependence on initial data. Figure 7.22(a) is the last frame of b7d, and has a CJ detonation for initial condition. Figure 7.22(b) is the last frame of b7dn2, and has a uniform inflow initial condition. From the image sequences in Figures 7.38 and 7.39, it can be observed that both solutions have settled to a steady state. As described in §7.2.2, much care is required to prevent the numerical method from failing due to the expansion behind the projectile. For case b7dn2, such a

(a) Full Domain
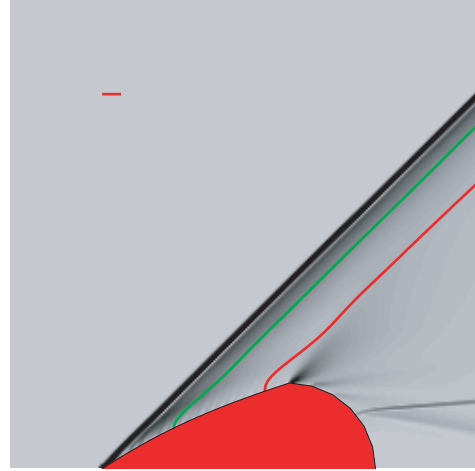
(b) Zoomed

Figure 7.21: Numerical Schlieren for the last frame of b3 in Table 7.3.
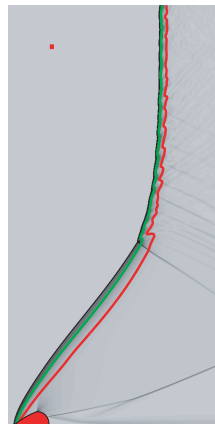
(a) Case b7d
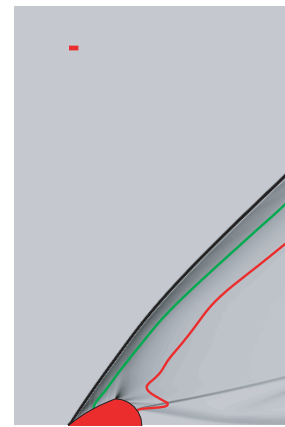
(b) Case b7dn2

Figure 7.22: Numerical schlieren images and reaction contours for b7d and b7dn2 (see Table 7.3).

Run ID:	b11	b11sr2	b16b
domain (x,y)	(30,20)	(5,6)	(35,50)
grid (nx,ny)	(600,400)	(250,300)	(350,500)
overdrive f	2.0	2.0	2.0
Mixture EOS	P1	P1	P1
Projectile Radius	1.0	1.0	5.0
Simulated Flight Distance	500	480	1000
Image Sequence	Figure 7.40	Figure 7.41	Figure 7.42

Table 7.4: Simulation parameters for cases b11, b11sr2 and b16b.

failure is avoided by very gradually accelerating the projectile to its final velocity. This can be seen in the image sequence of Figure 7.39 by observing the change in the projectile's position between the first and second frames.

To avoid the outflow boundary conditions just discussed, the simulations for the rest of the chapter focus on a single overdrive, $f = 2$. A solution has since been found that obviates the need for a CJ detonation initial condition and its associated tall domain requirement.

With this approach, an inert shock is placed in front of the projectile, and a nonreactive simulation is performed for a fixed number of timesteps before the reaction model is turned on. This allows the initial shock to be swept out of the domain much more quickly than if a CJ detonation had been used. In addition, it is observed that the simulation tends to settle to a steady state very quickly once the reaction model is switched on.

7.5 Critical decay rate model for initiation

In this section, the critical decay rate model of projectile-induced detonation (Kaneshige, 1999) is presented. For a projectile traveling at super-CJ speeds in a detonable mixture, the two main stabilized regimes are shock-induced combustion (no initiation) and coupled detonation (successful initiation). Experimentally, for a given projectile size and velocity, there exists a critical pressure threshold for a given mixture composition above which stabilized detonations are observed (see Figure 7.1). An increase in pressure leads to an increase in reaction rates, reducing the length scales associated with chemistry.

The transition between shock-induced combustion and detonation initiation is also observed numerically. For all numerical simulations that follow, the reaction length scale is used to nondimensionalize distance (see (7.7)) and is therefore fixed. Instead of pressure, the size of the projectile, and hence the fluid dynamic length scale, is varied.

(a) Case b11: Radius = 1

(b) Case b16b: Radius = 5
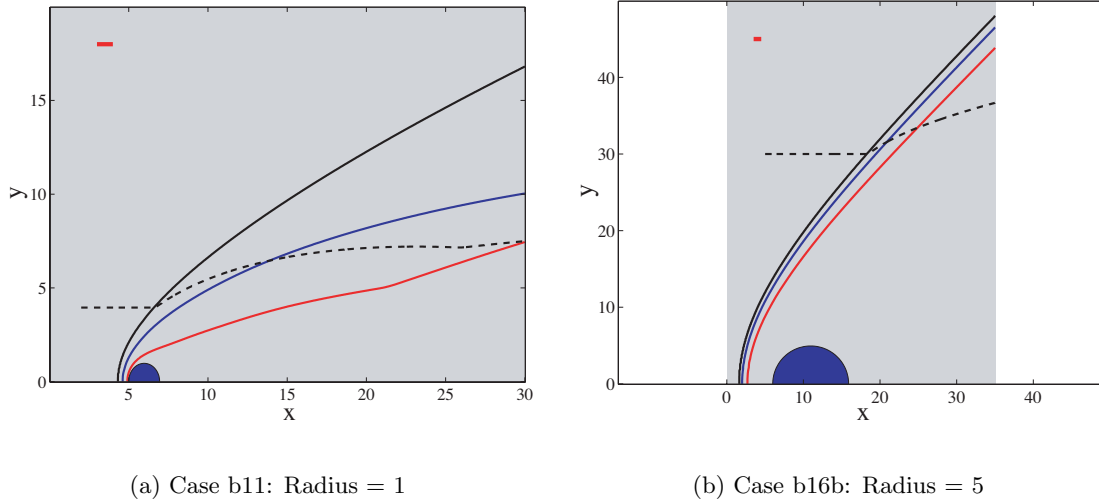
Figure 7.23: Steady reactive flows over supersonic projectiles. The leading shock and contours of 50% and 90% reaction for the two cases are plotted.

The leading shocks and the contours of 50% and 90% reactions with mixture P1 (see Table 7.2) for flows over projectiles of radii 1 (case b11) and 5 (case b16b) are shown in Figure 7.23. A marker indicating the size of the half-reaction length (i.e., 1 length unit) is shown on the upper left. Case b11sr2 is a high-resolution simulation near the nose. Parameters for the simulations are summarized in Table 7.4. The simulations were performed, as before, in the frame of reference of the traveling projectile. The steady-state solution is obtained by running time-accurate transient simulations for a significant number of steps (on the order of 30,000). The durations of the simulations for Case b11 and b16b correspond to the projectile traveling a distance of 500 and 1000 half-reaction lengths, respectively.

With the smaller projectile (Case b11, Figure 7.23(a)), the reaction zone decouples from the shock front, while the shock induces supersonic combustion near the nose and becomes inert away from the projectile. With the larger projectile (Case b16b) the reaction zone stays coupled as the shock turns from being normal to the incoming flow at the symmetry plane to the CJ angle $\beta = 45°$.

The streamline plotted in Figure 7.23(a) is the CJ streamline for Case b11. For Case b16b, because the leading shock approaches but does not reach the CJ angle, a representative streamline starting 30 units away from the stagnation streamline is used. The progress variable λ (Figure 7.24(a)) and the thermicity $\dot{\sigma}$ (Figure 7.24(b)) are plotted as functions of streamwise distance behind the shock.

(a) Profiles of λ
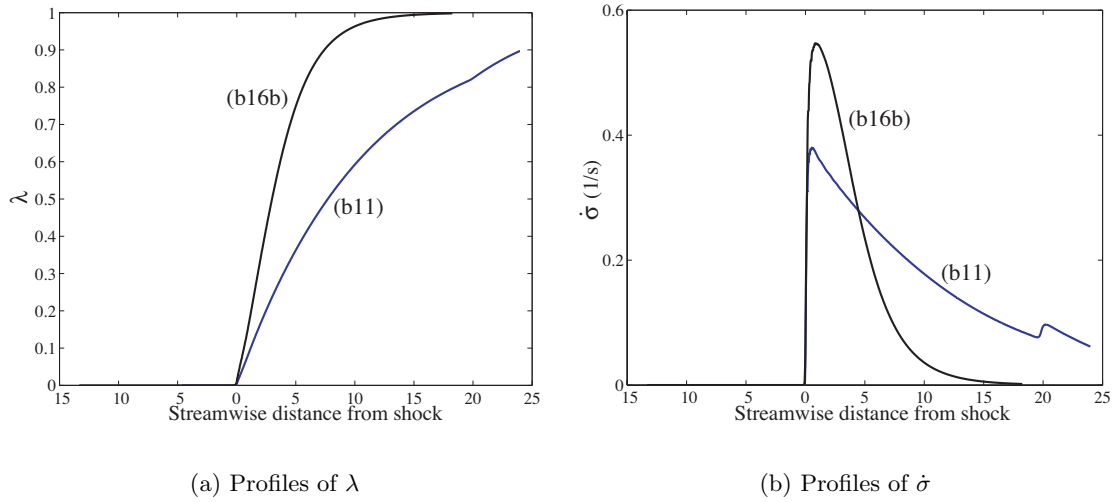
(b) Profiles of $\dot{\sigma}$

Figure 7.24: Reaction progress λ and thermicity ($\dot{\sigma}$) along the streamlines of Figure 7.23.

The leading shocks for these two cases are reoriented concave up with the shock tip at the origin. The profiles are then fitted (by sixth order polynomials) and differentiated to obtain the shock angle.

The fitted shock profile (solid line) and its first derivative (dashed) corresponding to $90° - \beta$ for the two cases appear in Figure 7.25. The CJ angle $\beta_{CJ} = 45°$ is indicated on the plots as a dotted line. For the non-detonative case on the left, the shock angle β goes through the β_{CJ} and eventually decays to the Mach angle sufficiently far downstream. The plot on the right shows that, with successful initiation, the shock angle asymptotically approaches β_{CJ}. For both cases, the steepening of the dashed lines (first derivatives) near the right edge is an artifact of the polynomial fitting. A different approach is to patch two functions together, one to handle the nose and the other to handle the straight portion.

Based on these two simulations for the mixture P1 at $f = 2$, it is to be expected that there is some critical radius for the projectile, between 1 unit and 5 units, above which a detonation will initiate successfully.

An initiation criterion suggested by Kaneshige (1999) is as follows. Immediately behind the curved shock, the evolution of a fluid particle depends on the balance of two effects: the heat release $\dot{\sigma}$ and gasdynamics quenching ($d\theta/dn$) due to streamline curvature (or streamtube area expansion). Two effects contribute to this expansion: chemical reaction and shock curvature. For a curved bow shock decaying (from being normal at the nose)

(a) Shock profile for Case b11

(b) Shock profile for Case b16b
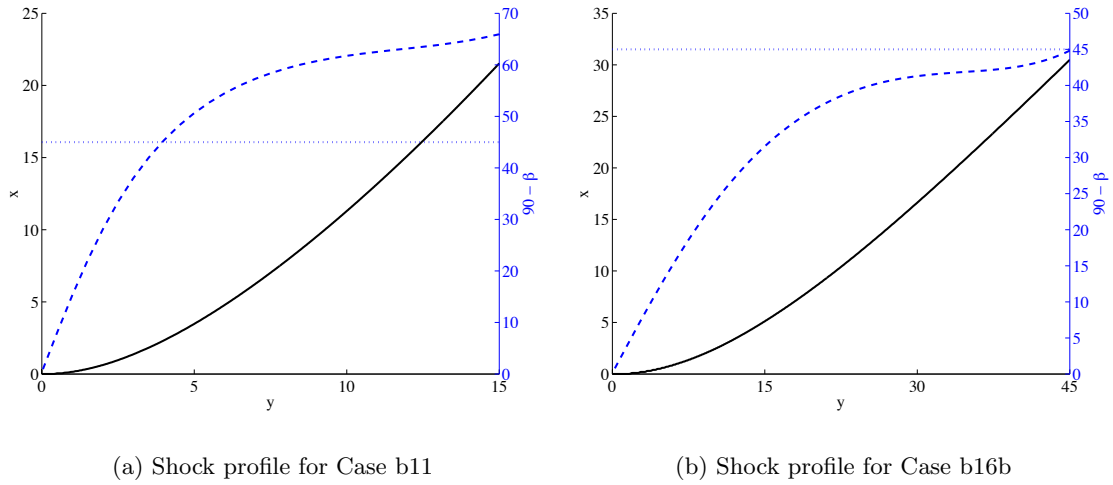
Figure 7.25: Shock and shock angles for Case b11 (a) and b16b (b). The shock is reoriented: the abscissa is y, the distance from the centerline. The fitted shock profile is shown as the solid line, and its first derivative $(90° − \beta)$ the dashed line. The dotted line marks the CJ angle $\beta = 45°$.

towards the CJ angle, it is conjectured that if the shock curvature is too high, the reaction will quench and the shock profile will pass right through the CJ angle, as seen for example in Figure 7.25(a).

Kaneshige proposed that criticality depends on the balance that causes the temperature derivative (of a Lagrangian particle at the von Neumann point) of an unsupported (CJ) detonation to vanish. For our simple mixture (no mole change, constant R), the temperature evolution equation (7.2e) can be simplified. Using the chain rule on the ideal gas EOS gives

$$\frac{\dot{T}}{T} = \frac{\dot{P}}{P} - \frac{\dot{\rho}}{\rho} , \qquad (7.18)$$

which can be expanded, using (7.2a) and (7.2b), to

$$\dot{T} = \frac{T}{\eta} \left[\left(1 - \gamma M^2\right) \dot{\sigma} - u M^2 \left(1 - \gamma\right) \frac{\partial \theta}{\partial n} \right] \qquad (7.19a)$$

$$= \frac{T}{M^2 - 1} \left[\underbrace{\left(\gamma M^2 - 1\right) \dot{\sigma}}_{A} - \underbrace{u M^2 \left(\gamma - 1\right) \frac{\partial \theta}{\partial n}}_{B} \right] . \qquad (7.19b)$$

(7.19) suggests that the temperature derivative is a balance between reaction (term A) and streamline divergence (term B). For supersonic flows $(M > 1)$, term A is positive $(\gamma > 1)$ when the thermicity is positive (heat release rather than heat absorption). Term

(a) Term A and B of (7.19) for b11   (b) Term A and B of (7.19) for b16b
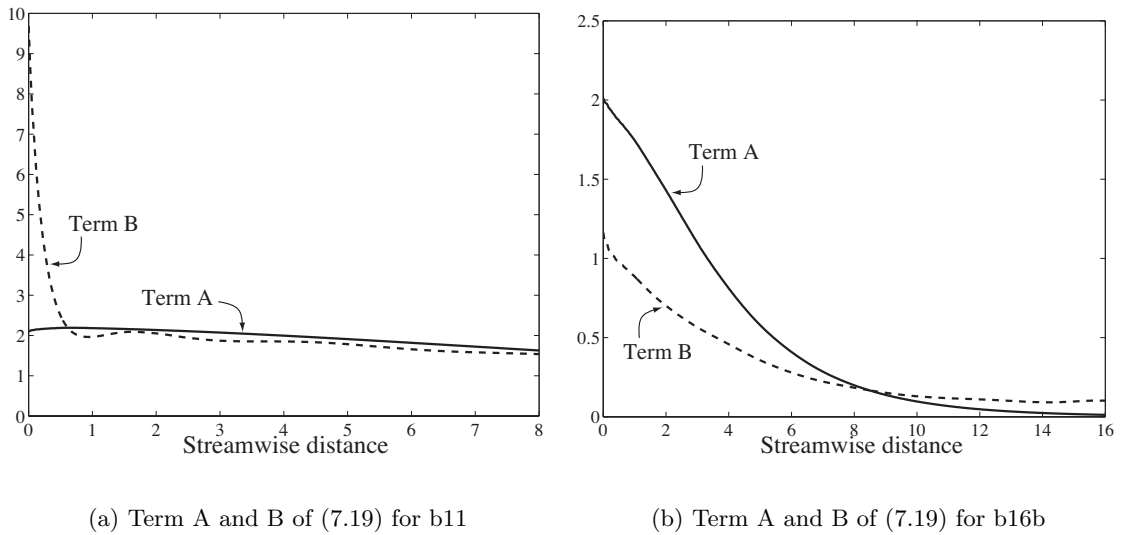
Figure 7.26: Balance of heat release and expansion (7.19).

B is also positive since $\gamma > 1$ and the term $\partial\theta/\partial n$ is positive for streamtube expansion ([see eq. (7.3)]). From (7.19b), the temperature derivative is positive when $A > B$. These two terms are plotted for the streamlines (see Figure 7.23) of b11 and b16b in Figure 7.26. In Figure 7.27, the $\dot{T}$ computed using (7.19) (marked "ZND" on the figures) is compared against the profile obtained by calucluating the first-order difference of the interpolated temperature profile (marked "Streamline").

From the relative sizes of A and B in Figure 7.26, the temperature is expected to drop at the shock ($\dot{T} < 0$) for b11, and to rise for b16b. While numerically differentiating the post-shocked state of the streamline of b16b shows that the derivative is indeed positive at the shock and agrees well with the computed profile (Figure 7.27(b)), there appears to be gross disagreement in the streamline for b11 (Figure 7.27(a)).

This discrepancy is an artifact of shock smearing. The difference between negative and positive post-shock gradients is illustrated in Figure 7.28(a). Numerical (shock-capturing) methods invariably misses and underestimates the post-shock peak when the gradient is negative (unless the method is oscillatory). For the CJ streamline of b11 this means that the von Neumann point temperature is a local maximum and is underpredicted, as shown in Figure 7.28(b). Thus, while the true profile that the numerical method is trying to capture has a peak followed by a negative gradient, its smeared numerical realization shows a positive gradient in the close vicinity of the shock.

(a) $\dot{T}$ for b11

(b) $\dot{T}$ for b16b
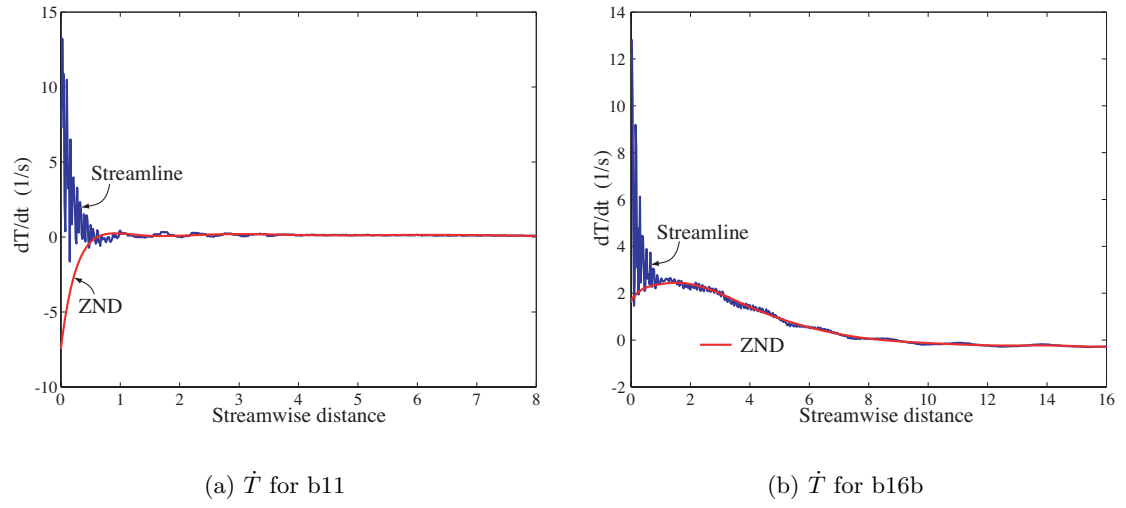
Figure 7.27: The temperature derivative $\dot{T}$ from streamline versus (7.19).

(a) Manifestations of shock smearing

(b) Temperature profile for b11
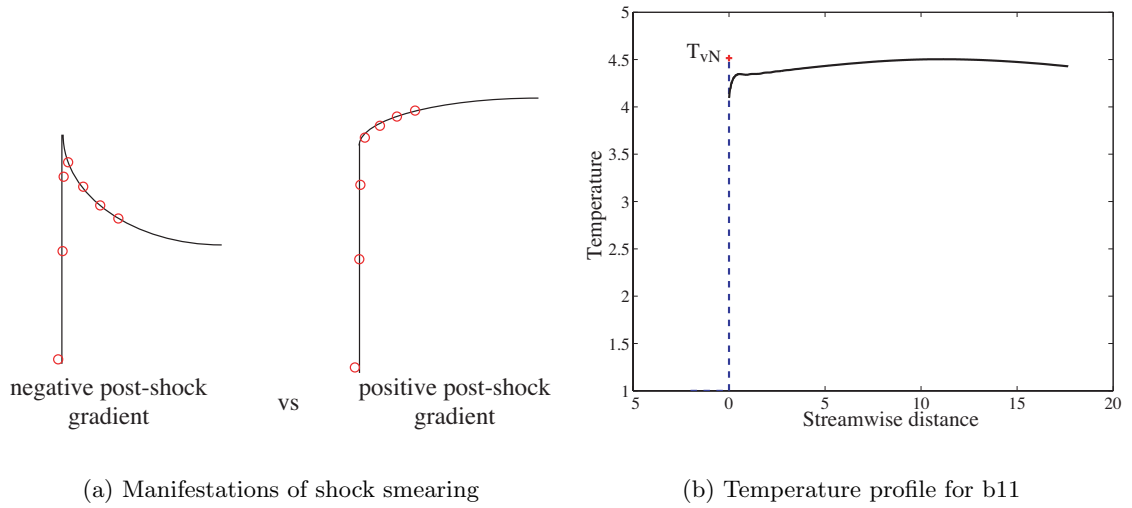
Figure 7.28: (a) contrasts the (disastrous) effect of shock smearing when the post-shock gradient is negative against the (mostly harmless) positive gradient. (b) shows temperature profile along the CJ streamline of b11 with the von Neumann point (smeared peak) marked.

The streamline divergence (term B), or expansion $\partial\theta/\partial n$, itself consists of two components: shock curvature and chemical reaction due to obliquity:

$$u\frac{\partial\theta}{\partial n} = \cos^2(\beta - \theta)\frac{\dot{\sigma}}{\eta_n} , \qquad (7.17)$$

which can be rewritten as

$$\left.\frac{\partial\theta}{\partial n}\right|_{\text{reaction}} = S_1\dot{\sigma} , \qquad (7.20)$$

where

$$S_1 \equiv \frac{\cos^2(\beta - \theta)}{u\eta_n} . \qquad (7.21)$$

(7.20) is thus the contribution of chemical reactions to the streamline divergence. This expansion can be written as the sum of a reactive part, given by (7.20), and a non-reactive part due to shock curvature κ.

Assuming that the shock curvature is known, the Lagrangian derivative of density $d\rho/ds$ for a planar nonreactive curved shock at the post-shock point (from (3.45) of Kaneshige, 1999) is given by

$$\frac{1}{\rho_o}\frac{d\rho}{ds} = \kappa\frac{2\cos(\beta - \theta)}{\gamma + 1}\left[\frac{\cos\theta}{\sin(\beta - \theta)\cos\beta} - \frac{8}{\gamma + 1}\frac{\sin\beta\cos^2(\beta - \theta)}{\sin\theta\sin(\beta - \theta)}\right] , \qquad (7.22)$$

where the wave curvature κ of a plane-shock having a profile $y(x)$, with the nose at the origin oriented concave up, is given by

$$\kappa = \frac{d^2y/dx^2}{\left[1 + (dy/dx)^2\right]^{3/2}} . \qquad (7.23)$$

From (7.2b), the derivative in (7.22) can also be expressed as a function of streamline divergence,

$$\frac{1}{\rho_o}\frac{d\rho}{ds} = \frac{\rho}{\rho_o}\frac{M^2}{\eta}\frac{\partial\theta}{\partial n} , \qquad (7.24)$$

where all properties are to be evaluated at the post-shock point. From (7.22), the streamtube expansion *at the shock* due to shock curvature can be calculated as

$$\left.\frac{\partial\theta}{\partial n}\right|_{\text{curvature}} = S_2\kappa , \qquad (7.25)$$

where

$$S_2 \equiv \frac{\rho_o}{\rho} \frac{\eta}{M^2} \left\{ \frac{2\cos(\beta-\theta)}{\gamma+1} \left[\frac{\cos\theta}{\sin(\beta-\theta)\cos\beta} - \frac{8}{\gamma+1} \frac{\sin\beta\cos^2(\beta-\theta)}{\sin\theta\sin(\beta-\theta)} \right] \right\} . \tag{7.26}$$

The (total) streamtube expansion at the shock is the sum of the reactive component (7.20) and the shock curvature component (7.25),

$$\frac{\partial\theta}{\partial n} = S_1\dot\sigma + S_2\kappa . \tag{7.27}$$

For a given freestream Mach number M_o and flow velocity $u_f s$, both S_1 and S_2 can be written as functions of the shock angle β. Using the oblique shock jump relations

$$\cot\theta = \tan\beta \left[\frac{(\gamma+1)M_o^2}{2(M_o^2\sin^2\beta - 1)} - 1 \right] , \tag{7.28a}$$

$$M_n{}^2 = \frac{(\gamma-1)M_o^2\sin^2\beta + 2}{2\gamma M_o^2\sin^2\beta - (\gamma-1)} , \tag{7.28b}$$

$$M = M_n\csc(\beta-\theta) , \tag{7.28c}$$

$$u = u_o\sqrt{\cos^2\beta + \frac{(\gamma-1)M_o^2\sin^2\beta + 2}{(\gamma+1)M_o^2\sin\beta}} , \quad \text{and} \tag{7.28d}$$

$$\frac{\rho}{\rho_o} = \frac{(\gamma+1)M_o^2\sin^2\beta}{(\gamma-1)M_o^2\sin^2\beta + 2} , \tag{7.28e}$$

the terms S_1 and S_2 can be plotted over a range of shock angles for Mixture P1 (Table 7.2) at an overdrive $f = 2$ (the corresponding freestream Mach number is $M_o = 6.07$). This plot is shown in Figure 7.29.

Using (7.27), the temperature evolution equation (7.19) can be separated into a component due to reaction and another due to shock curvature. Expanding S_1 from (7.21) and substituting into (7.19), the Lagrangian temperature derivative at the shock is

$$\frac{\dot T}{T} = \underbrace{(1-\gamma M^2)\frac{\dot\sigma}{\eta}}_{\text{heat release}} - \underbrace{M^2(1-\gamma)\frac{\cos^2(\beta-\theta)}{\eta_n}\frac{\dot\sigma}{\eta}}_{\text{obliquity}} - \underbrace{M^2(1-\gamma)\frac{u}{\eta}S_2\kappa}_{\text{curvature}} . \tag{7.29}$$

Using (see Figure 7.15)

$$\cos^2(\beta-\theta) = \left(1 - \frac{M_n{}^2}{M^2}\right) ,$$
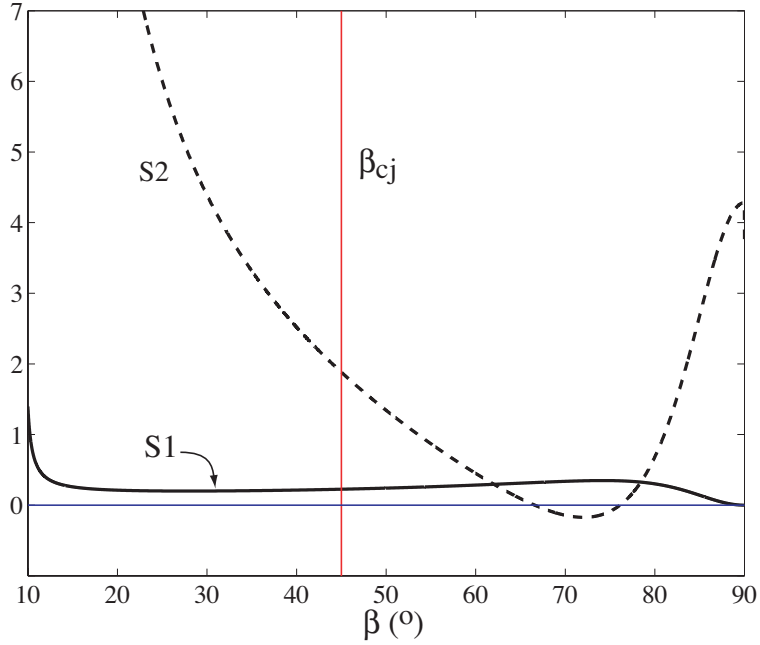
Figure 7.29: The two coefficients S_1 and S_2 of (7.27).

it can be verified that

$$\frac{1}{\eta_n} = \frac{1}{\eta} - \frac{M^2 \cos^2(\beta - \theta)}{\eta \eta_n}$$

and

$$\frac{w^2}{\eta_n} = \frac{u^2}{\eta} - \frac{u^2 \cos^2(\beta - \theta)}{\eta \eta_n} \ ,$$

hence (7.29) can be simplified to

$$\frac{\dot{T}}{T} = \left(1 - \gamma M_n{}^2\right) \frac{\dot{\sigma}}{\eta_n} - M^2 \left(1 - \gamma\right) \frac{u}{\eta} S_2 \kappa \ . \tag{7.30}$$

When $\kappa = 0$, (7.30) reduces to the evolutionary equation of temperature for a normal shock. The criterion for initiation according to the critical decay-rate model is that a particle crossing the leading bow-shock at the CJ angle must experience a temperature *rise* at the von Neumann point.

7.6   Determining the wave-curvature

Application of the critical decay-rate model requires that the wave-curvature κ be known when the shock is at β_{CJ}. Let this wave-curvature be labelled κ_{CJ}. When initiation is

Run ID:	Q1	b11sr2	b16b
domain (x,y)	(5,5)	(5,6)	(35,50)
grid (nx,ny)	(600,600)	(250,300)	(350,500)
overdrive f	2.0	2.0	2.0
Mixture EOS	P1 ($\lambda = 0$)	P1	P1
Projectile Radius	1.0	1.0	5.0
Simulated Flight Distance	64	480	1000
Description:	Unreactive	Shock-induced combustion	Detonation initiation

Table 7.5: Simulation parameters for cases Q1, b11sr2 and b16b.

Run ID:	R1	R2	R3	R4	R5	R6
Projectile Radius	1.0	2.5	5.0	12.0	1.0	1.0
domain (x,y)	(5,5)	(30,45)	(30,42)	(45,60)	(20,15)	(5,7.5)
grid size	0.0083	0.10	0.10	0.10	0.050	0.017
Number of Cells / Radius	120	25	50	120	20	60
Standoff distance / Radius	0.455	0.464	0.468	0.447	0.480	0.460

Table 7.6: Parameters for nonreactive simulations (EOS P1 at $\lambda = 0$).

successful, the shock angle asymptotically approaches β_{CJ} and the detonation wave becomes a straight oblique wave; $\kappa_{CJ} = 0$. The leading shock profiles for three different simulations showing varying degrees of reaction are shown in Figure 7.30. Parameters of the simulations are shown in Table 7.5 (with b11sr2 and b16b repeated from Table 7.4).

From Figure 7.30(a), it can be seen that the leading shock widens in the presence of exothermic reactions which cause expansion in the fluid behind the shock. If the profile changes smoothly with increasing degree of reaction, the curvature β_{CJ} assumes a maximum value for an inert shock and decreases with increasing degree of reaction (becoming 0 with successful initiation). This is illustrated in Figure 7.30(b).

Without *a priori* knowledge of the real shock shape (which depends on the degree of reaction), a value of κ_{CJ} is still needed. To this end, the inert profile is used (providing an upper bound on the true κ_{CJ}). For a given mixture and a given free-stream Mach number, the shock's profile scales with the projectile radius. Table 7.6 lists six simulations of the frozen ($\lambda = 0$, i.e., inert) flow of the gas mixture P1 at Mach 6.07 (which corresponds to an overdrive $f = 2$) over projectiles of different sizes. The tabulated values for the standoff distances between the projectile and the shock at the plane of symmetry are scaled by the projectile radii. The shock's profile is defined numerically as the $M = 4$ level-set, which appears to work well for this flow configuration.
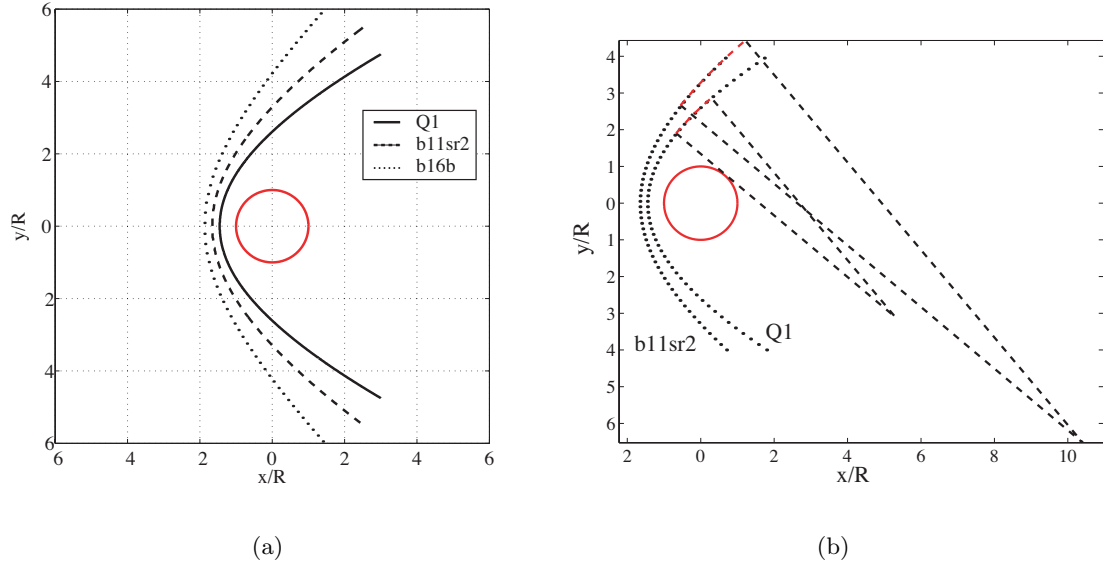
Figure 7.30: A comparison of the profiles of the leading shock at different degrees of reaction (a). The simulation parameters are tabulated in Table 7.5. (b) compares the radius of curvature at CJ $1/\kappa_{CJ}$ for the unreactive case (Q1) to that for the case exhibiting supersonic combustion (but no initiation) (b11sr2).

For the numerical simulation of the inert bow shock, two length scales are important. The physical length scale for the gasdynamics is given by the projectile radius R. Grid density therefore depends on the number of cells per projectile radius, which is reported in Table 7.4. On the other hand, the grid size itself is important in that the shock wave is smeared over a (fixed) number of grid cells, so decreasing the grid's spacing allows the shock's (interpolated) position to be determined more accurately. The shock profiles (scaled by the projectile radius) for the 6 cases are shown in Figure 7.31.

The case R1, having the finest resolution, is used to determine the shock profile. The re-oriented shock and the shock angles are plotted in Figure 7.32. Differentiating the sixth order polynomial fit to the shock, the CJ curvature κ_{CJ} is found from (7.23) to be

$$\kappa_{CJ} = 0.128\frac{1}{R} \;,\tag{7.31}$$

where R is the radius of the projectile. This provides the needed connection to the main balance equation (7.30).
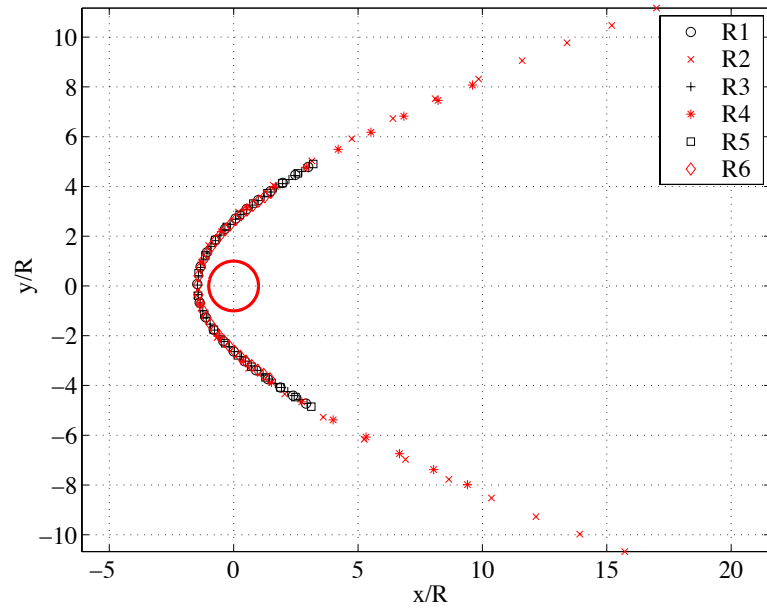
Figure 7.31: Inert bow shock over a cylindrical projectile traveling at Mach 6.07.
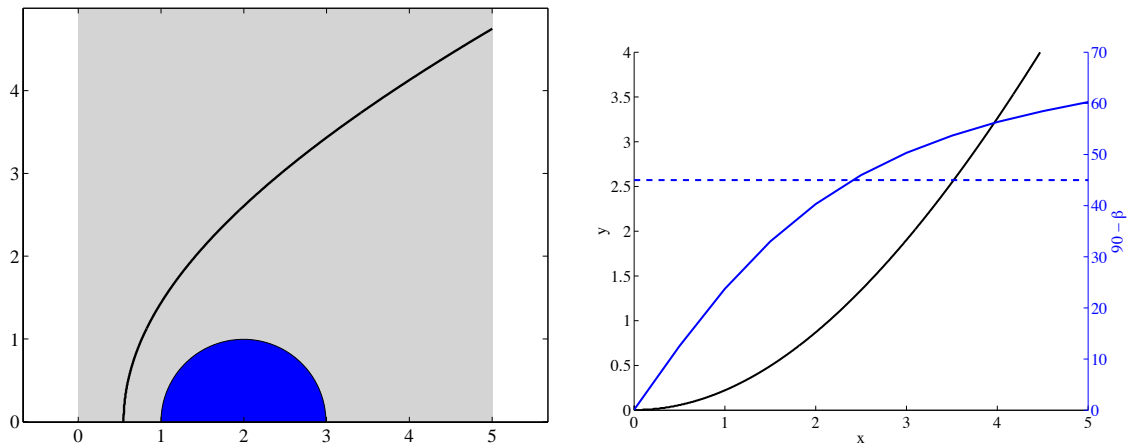
Figure 7.32: Inert shock and shock angles for the Case R1.

Mixture P1 and P2 at $\mathsf{f}=2$, $\beta=45^o$			
θ	33.03^o	u	5.19
η	-3.26	P	21.3
M	2.06	T	4.52
w	1.08	ρ	4.71

Table 7.7: Properties at the von Neumann point for a CJ detonation.

7.7 Predictions of the critical decay rate model

Based on the fitted shock profile for a projectile travelling at an overdrive of $\mathsf{f}=2$ from the previous section, the expansion quenching due to shock curvature (7.30) can be written as a function of the projectile radius using (7.31),

$$\frac{\dot{T}}{T} = \left(1 - \gamma M_n{}^2\right)\frac{\dot{\sigma}}{\eta_n} - M^2\left(1-\gamma\right)\frac{u}{\eta}\frac{0.128}{R}S_2 \ , \tag{7.32}$$

where all properties are to be evaluated at the von Neumann point of a CJ detonation. For the mixtures listed in Table 7.2 at an overdrive $\mathsf{f}=2$, the properties at the von Neumann point appear in Table 7.7.

Using the properties in Table 7.7 and the freestream density $\rho_o = 1$ (by virtue of nondimensionalization), the value of S_2 in (7.26) is computed to be 1.883. Substituting into (7.25),

$$\frac{\partial \theta}{\partial n} = 1.883\kappa_{CJ} = \frac{0.2416}{R} \ . \tag{7.33}$$

The streamtube area ratio interpolated from the simulation (of case R1) for the CJ streamline, shown in Figure 7.33(a), is plotted in Figure 7.33(b). The value for A/A_o at the von Neumann point comes from the shock-jump condition, and its slope agrees well with the prediction of the curvature model.

Setting the temperature derivative of (7.32) to zero and rearranging,

$$R_{\mathrm{cr}} = 0.128 S_2 \frac{u}{\dot{\sigma}}\frac{M^2(1-\gamma)}{1-\gamma M_n{}^2}\frac{\eta_n}{\eta}\bigg|_{vN} \ , \tag{7.34}$$

which is to be evaluated at the von Neumann point with the properties shown in Table 7.7. R_{cr} is the predicted critical projectile radius at an overdrive factor $\mathsf{f}=2$. The thermicity
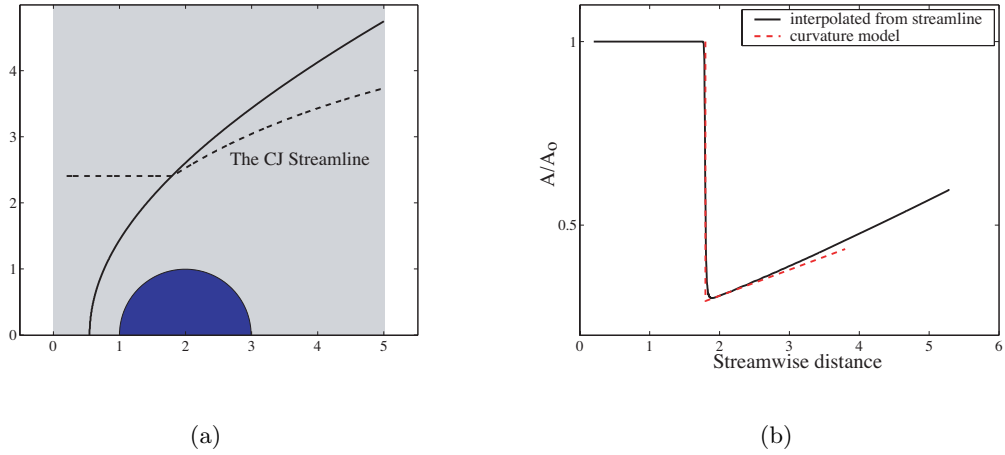
Figure 7.33: The CJ streamline for case R1 is shown in (a). The area ratio A/A_o interpolated along the streamline is plotted in (b). The dashed line represents the linear-approximant computed from the shock-curvature at the von Neumann point.

product $\dot{\sigma}$ for the one-step model is

$$\dot{\sigma}_{vN} = k \frac{q}{c_p T_{vN}} \exp \frac{-E_a}{T_{vN}} \; , \tag{7.35}$$

which evaluates to $\dot{\sigma}_{vN} = 0.440$ for the mixture properties in Table 7.2.

For a given mixture and post-shock condition, the value of k is determined numerically such that the half-reaction zone length is $\Delta_{1/2} = 1$ for a CJ detonation. While the exact functional dependence on k needs to be numerically computed, an asymptotic analysis using the Frank-Kamenetskii's approximation can be used for estimating the "explosion time" τ. For the one-dimensional planar CJ detonation, this is (see eq. (2.24) of Eckett, 2001)

$$\tau = \frac{1}{k} \frac{1 - M_n{}^2}{1 - \gamma M_n{}^2} \frac{T_{vN}}{E_a} \frac{c_p T_{vN}}{q} \exp \frac{E_a}{T_{vN}} \; , \tag{7.36}$$

which is to be evaluated at the von Neumann point. The value of k can be estimated as follows: since the induction zone length

$$\Delta_{1/2} \approx \tau \cdot w = 1 \; , \tag{7.37}$$

where w is the (normal) velocity at the von Neumann point, rearranging (7.36) leads to

$$k \approx w \frac{1 - M_n^2}{1 - \gamma M_n^2} \frac{T_{vN}}{E_a} \frac{c_p T_{vN}}{q} \exp \frac{E_a}{T_{vN}} \; . \tag{7.38}$$

Using the above and the properties in Table 7.2, the value of k for mixture P1 evaluates to $k \approx 13.02$, not too far from the numerically determined value of 16.1. Using (7.38), (7.35) becomes

$$\dot{\sigma}_{vN} \approx w \frac{T_{vN}}{E_a} \frac{1 - M_n^2}{1 - \gamma M_n^2} \; . \tag{7.39}$$

Substituting into (7.34), using $\csc(\beta - \theta) = u/w$ and reverting to dimensional variables, the criticality condition becomes

$$\frac{R_{\mathrm{cr}}}{\Delta_{1/2}} \approx 0.128 S_2 \csc(\beta - \theta) \frac{M^2(1 - \gamma)}{1 - M^2} \frac{E_a}{\mathcal{R} T_{vN}} \; , \tag{7.40}$$

which is to be evaluated at the von Neumann point. The above equation gives a sense of the dependence of the nondimensional critical radius at $\mathsf{f} = 2$ (scaled by $\Delta_{1/2}$) as a function of the nondimensional parameters $M, E_a/\mathcal{R} T_{vN}$ and γ.

The critical radius R_{cr} will now be determined by going back to (7.34). It represents a balance between temperature rise due to chemical reaction and temperature drop due to streamtube divergence. The critical decay-rate model put forth by Kaneshige (1999) proposes that when the projectile radius is larger than this critical radius, detonation initiation will occur. Evaluating (7.34) using mixture P1, the critical radius for the projectile is computed to be

$$\frac{R_{\mathrm{cr}}}{\Delta_{1/2}} = 1.7 \; .$$

When the thermodynamic parameters (i.e., the independent quantities γ, q) are held constant, the CJ speed, inert shock-shape, von Neumann states, and CJ state remain constant. The critical radius in (7.34) can be solved for a range of activation energies E_a, or its nondimensional form $E_a/\mathcal{R} T_{vN}$. This is shown in Figure 7.34.

For the mixture P1 under study $E_a/\mathcal{R} T_{vN} = 3.32$. It has already been observed that a projectile of radius $R_p = 1$ does not lead to detonation initiation (case b11 of Table 7.4), whereas initiation is successful when the projectile's radius is 5 (case b16b of Table 7.4). Three new runs, listed in Table 7.8, are plotted in Figure 7.34. Run b19 corresponds to
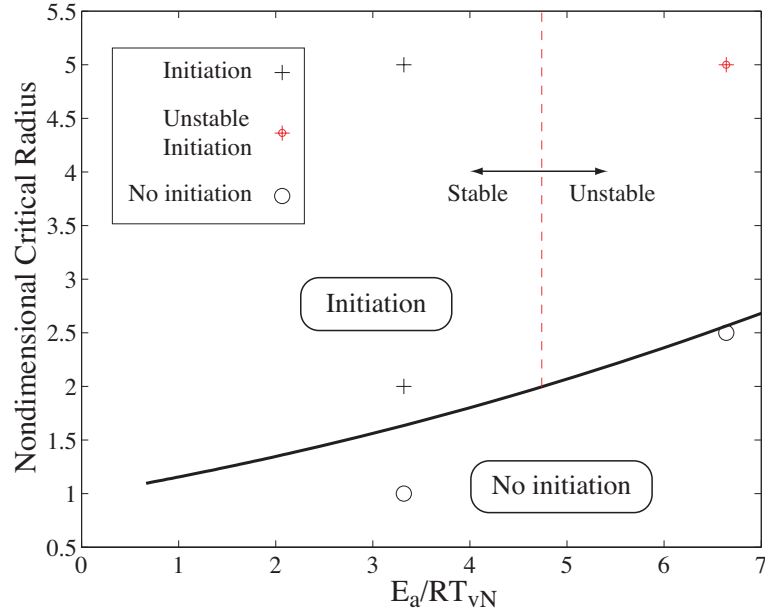
Figure 7.34: Critical radius based on the critical decay rate model as a function of $E_a/\mathcal{R}T_{vN}$.

Run ID:	b19	E2	E3
Projectile Radius	2.0	2.5	5.0
domain (x,y)	(30,30)	(30,45)	(30,42)
grid (nx,ny)	(500,500)	(350,450)	(300,420)
overdrive f	2.0	2.0	2.0
Mixture EOS	P1	P2	P2
Simulated Flight Distance	600	500	900

Table 7.8: Simulation parameters for Figure 7.34

.

the same $E_a/\mathcal{R}T_{vN}$, where the projectile radius $R_p = 2$ is not substantially greater than the predicted critical radius of 1.7. Two new cases, E2 and E3, are simulated with the mixture P2 (see Table 7.2) at a higher value of $E_a/\mathcal{R}T_{vN}$. The neutral stability boundary for one-dimensional planar CJ detonation is also shown in Figure 7.34.

The case b19, indicated in Figure 7.34 as exhibiting initiation, is actually *near critical* in the sense that it is hard to say with confidence whether initiation is successful. The last frame of the simulation, corresponding to a simulated flight distance of 600 units, is shown in Figure 7.35(a). While the behavior shown is closer to initiation (Figure 7.23(b)) than failure (Figure 7.23(a)), the reaction zone seems to be pulling away from the leading shock, albeit much more slowly than in the case of b11 which unequivocally exhibits failure. To

(a) Last frame of b19   (b) Last frame of E2
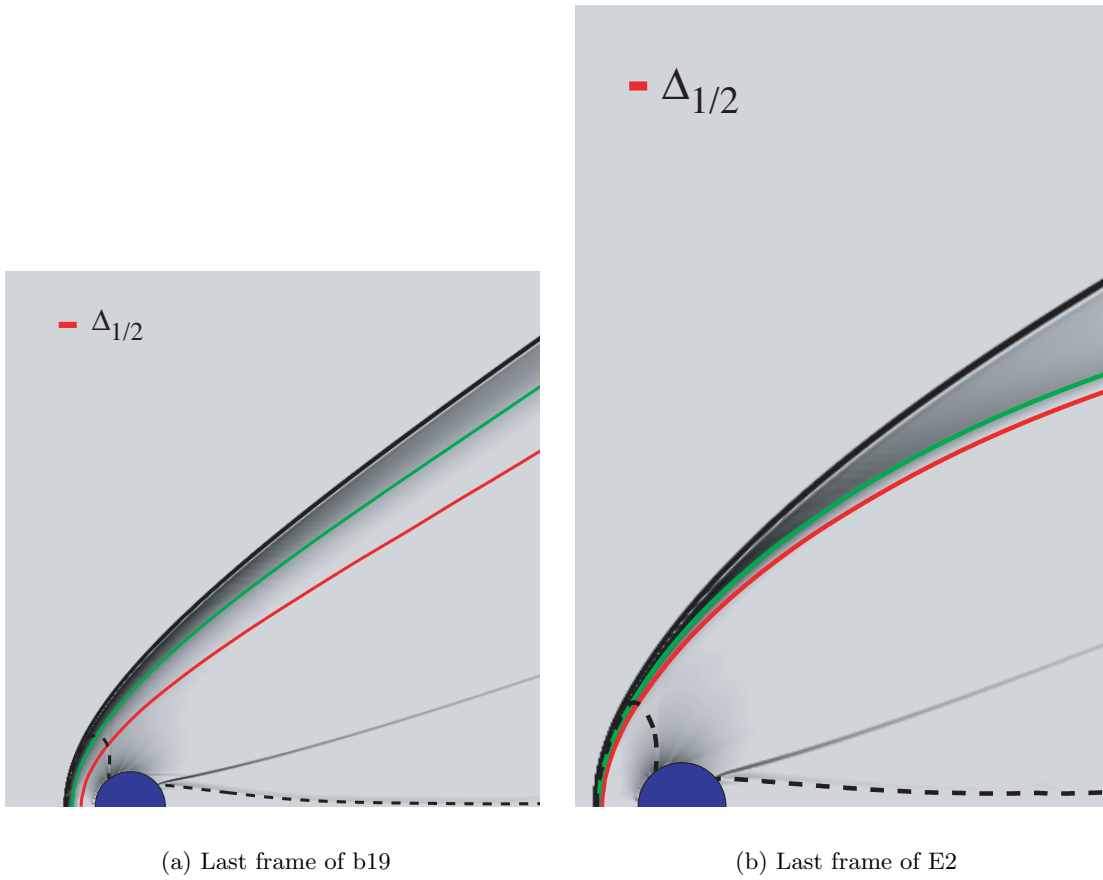
Figure 7.35: Numerical schlieren and reaction contours for cases b19 and E2

better characterize this projectile size $R_p = 2$, a much larger domain needs to be simulated.

For the two cases using the mixture P2, the last frame of case E2 at $R_p = 2.5$ is shown in Figure 7.35(b). An image sequence for E3 is shown in Figure 7.43.

7.8 Conclusions

Numerical simulations of detonations initiated by hypervelocity projectiles were presented. Detailed kinetics simulation of the conditions required for a stabilized detonation is beyond the reach of our current computational facility, and only the supersonic shock-induced combustion regime was realized.

Resorting to a one-step irreversible reaction model, the transition from shock-induced combustion to stabilized oblique detonation was observed. Using the critical decay-rate model of Kaneshige (1999), an analysis of this transition was presented and its prediction

compared against the numerical results. While the prediction of the model reconciled with the numerical observations, it should be noted that these simulations explored only a small part of the parameter space. A detailed investigation of the effect of the overdrive f, heat release q, the effect of reaction order, etc., will be needed in order to thoroughly validate the model.

In the experiments of Kaneshige (1999), the transition from shock-induced combustion to detonation was observed to occur at a $R_p/\lambda_d \approx 2.5$ for a wide range of mixtures and overdrive factors, where λ_d is the detonation cell width, a commonly used factor used for characterizing detonable mixtures. For H_2-O_2-N_2 mixtures, the ratio $\lambda/\Delta_{1/2} \approx 30$ (see Fig 4.8 of Kaneshige, 1999), and varies from 10 to 100 for the mixtures studied. Hence the experimentally observed transition is $R_{cr}/\Delta_{1/2} \approx 30 \sim 100$. Similarly, in the experiments of Kasahara et al. (2002) using Krypton diluted acetylene-oxygen mixtures, the transition to detonation initiation was observed to also occur at $R_p/\lambda_d \approx 2.5$.

On the other hand, the numerical experiments as well as the critical decay-rate model predicted a transition at $R_{cr}/\Delta_{1/2} \approx 2$, some $15 \sim 50$ times smaller than experimentally observed. The main explanation for this discrepancy is that a first-order one-step Arrhenius model used in this work cannot, and did not, capture the true reaction kinetics of real detonable mixtures. The projectiles simulated in this work are cylindrical and not spherical, and the mixture conditions studied in this thesis are chosen to suppress transverse waves so the notion of detonation cell size is not applicable. Numerical simulations using detailed reaction kinetics with sufficient grid-refinement to capture the nuances of three-dimensional detonation instabilities will be extremely challenging and require substantial advances in computational power and algorithms.

7.9 Image sequences

The following image sequences correspond to simulations discussed in the previous section. Please see figure captions and refer to the main text for more details.
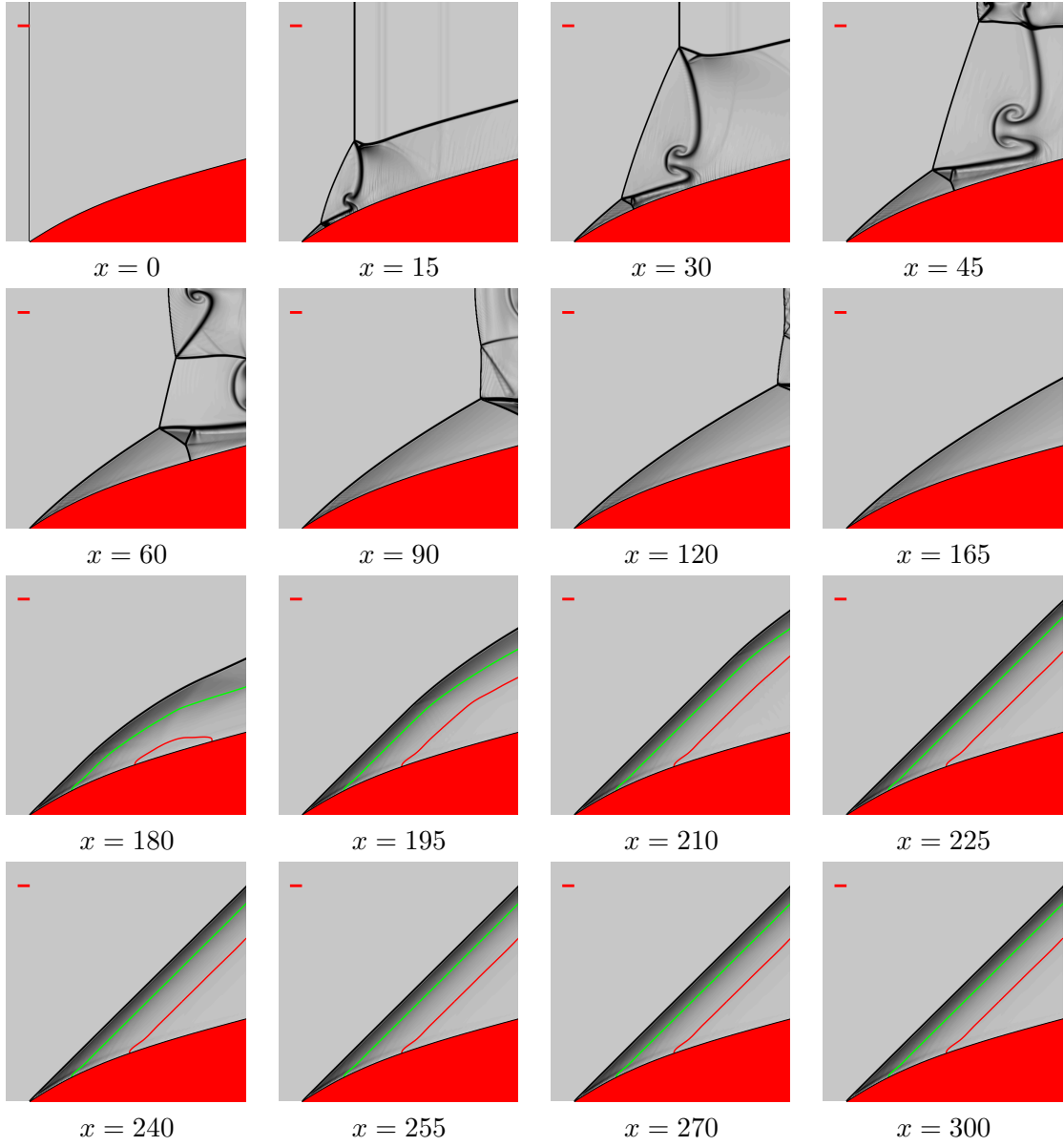
Figure 7.36: Numerical schlieren and reaction contours for flow over a streamline wedge.

$x = 0$ $x = 8$ $x = 16$ $x = 24$ $x = 32$ $x = 40$

$x = 48$ $x = 56$ $x = 64$ $x = 72$ $x = 80$ $x = 88$

$x = 112$ $x = 136$ $x = 160$ $x = 184$ $x = 208$ $x = 232$

$x = 256$ $x = 280$ $x = 304$ $x = 336$ $x = 368$ $x = 400$
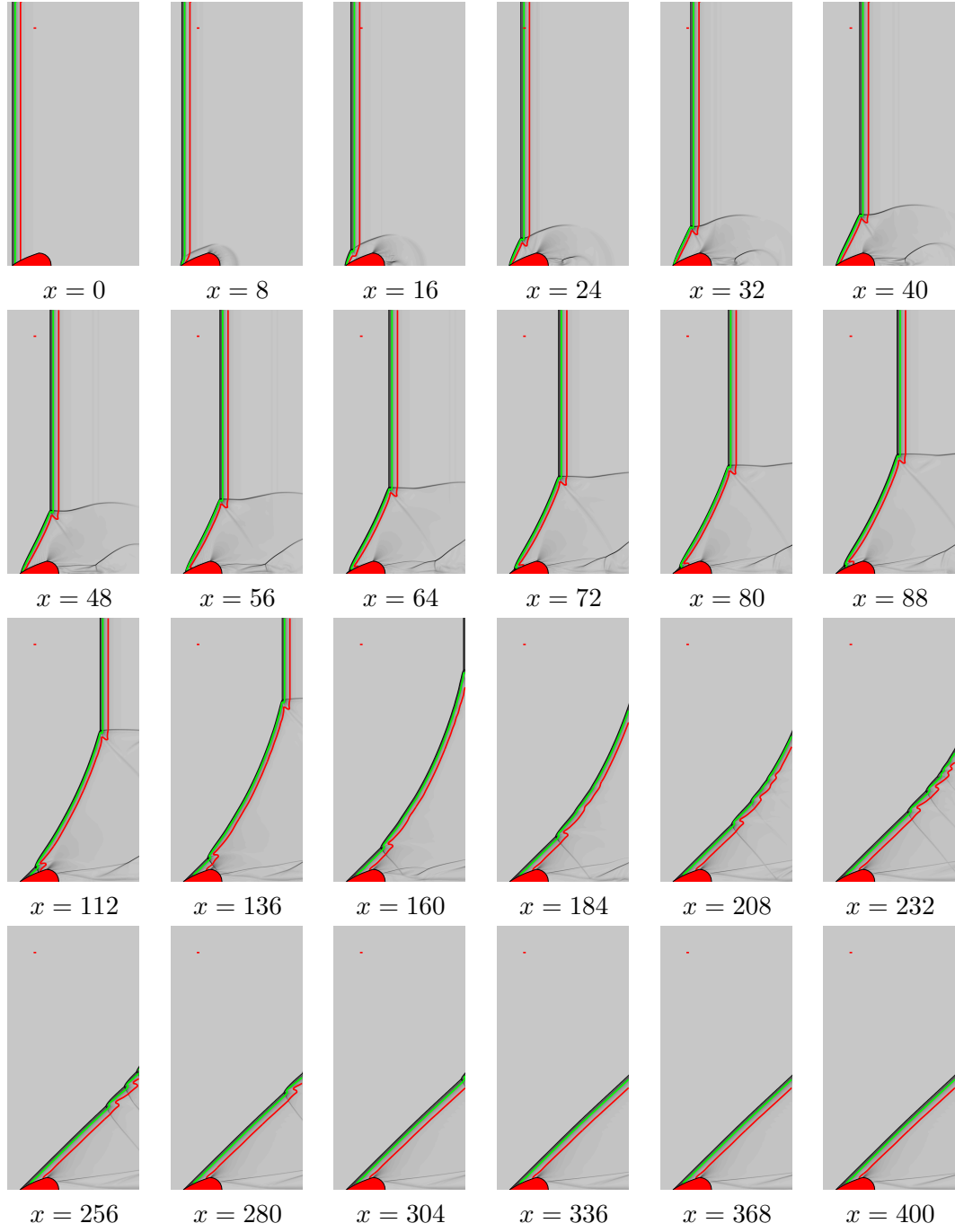
Figure 7.37: Numerical schlieren and reaction contours for case B3 in Table 7.3.

$x = 0$ $x = 20$ $x = 40$ $x = 60$ $x = 80$ $x = 100$

$x = 120$ $x = 140$ $x = 160$ $x = 180$ $x = 200$ $x = 220$

$x = 280$ $x = 340$ $x = 400$ $x = 460$ $x = 520$ $x = 580$

$x = 640$ $x = 700$ $x = 760$ $x = 840$ $x = 920$ $x = 980$
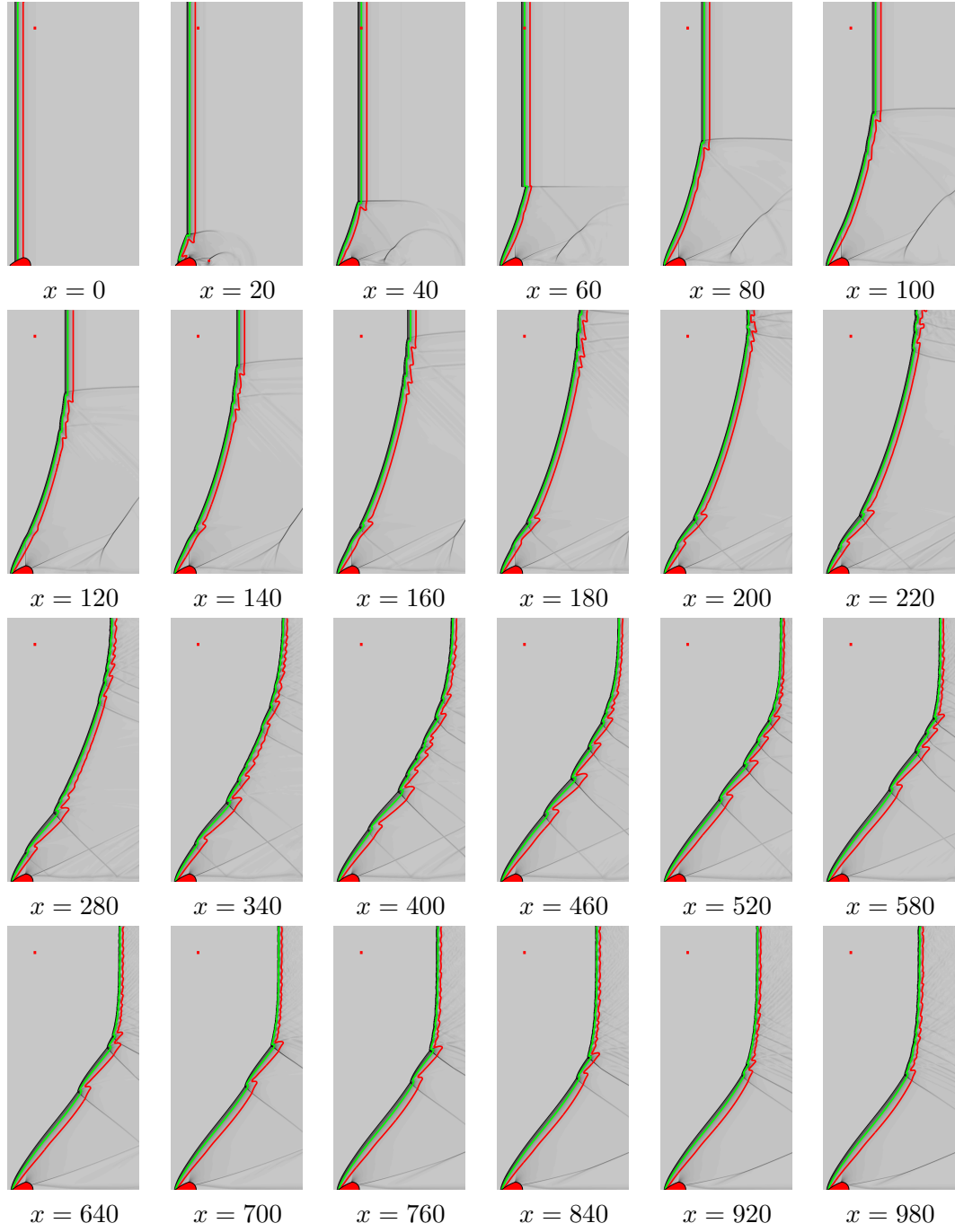
Figure 7.38: Numerical schlieren and reaction contours for case b7d in Table 7.3.

$x = 0$ $x = 20$ $x = 40$ $x = 60$

$x = 80$ $x = 100$ $x = 120$ $x = 140$

$x = 160$ $x = 180$ $x = 200$ $x = 220$

$x = 240$ $x = 400$ $x = 600$ $x = 840$
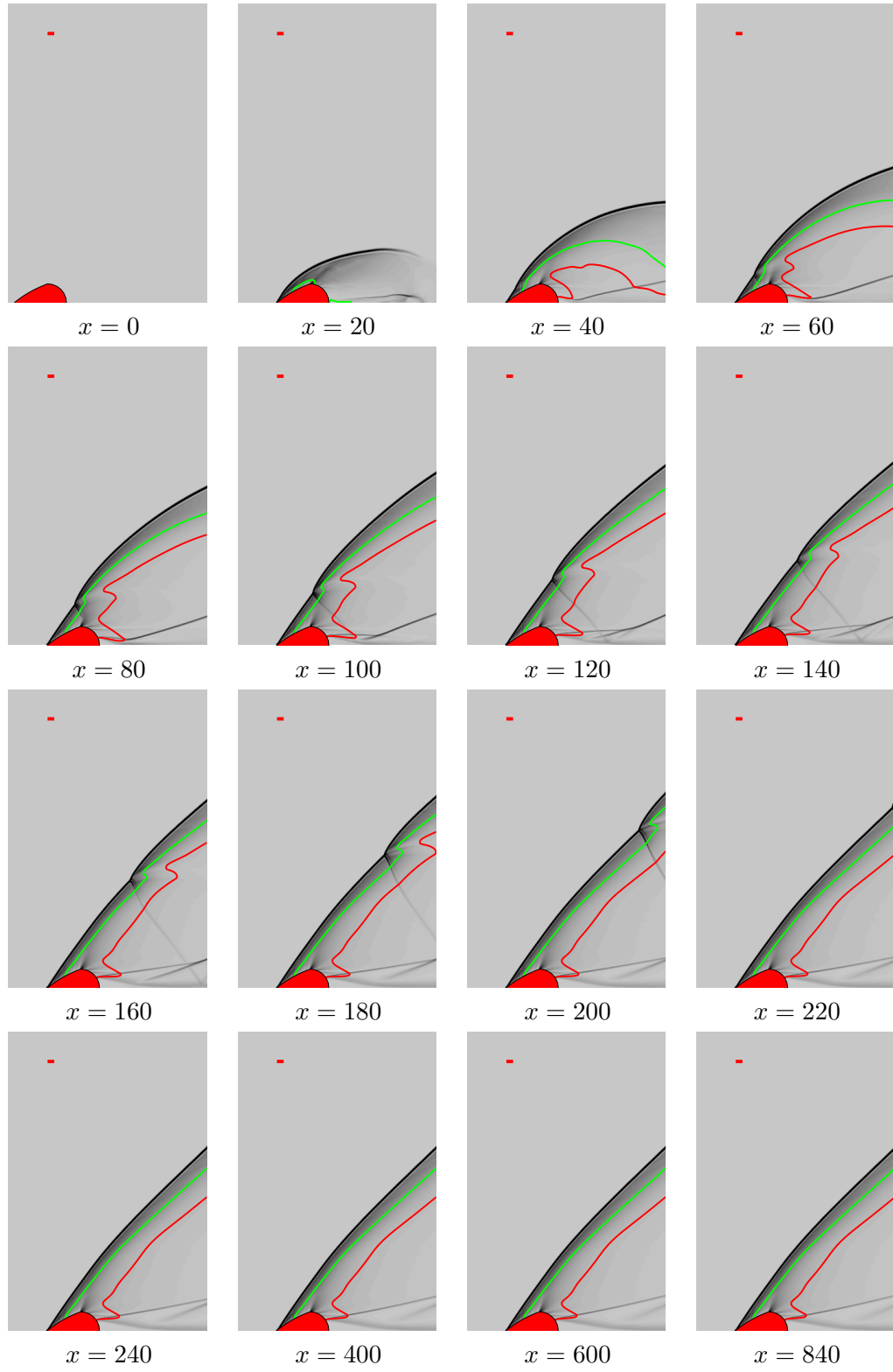
Figure 7.39: Numerical schlieren and reaction contours for case b7dn2 in Table 7.3.
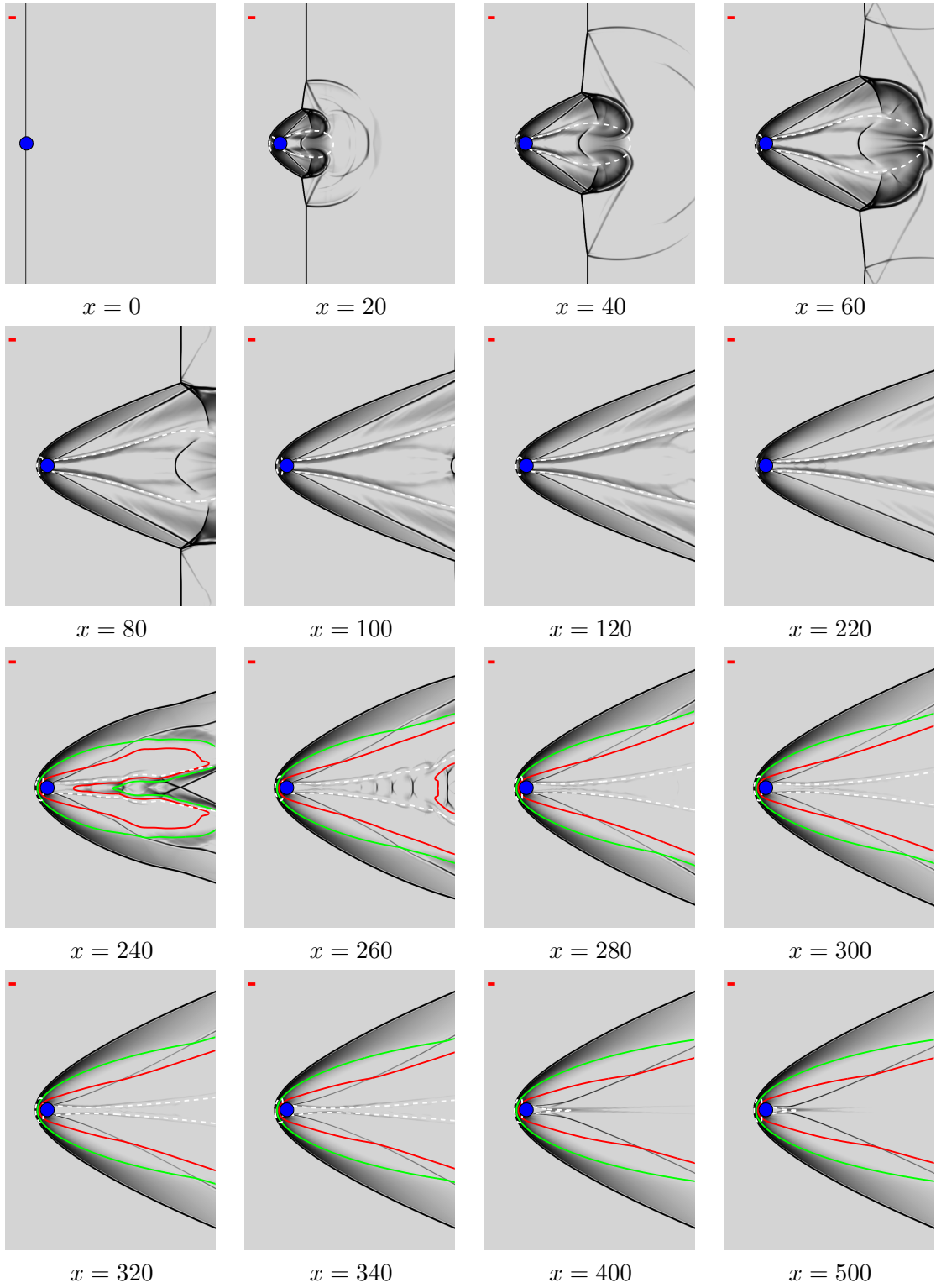
Figure 7.40: Numerical schlieren and reaction contours for case b11 in Table 7.4. The white dashed line is the sonic locus. The computational domain is mirrored in post-processing to show the full channel.

$x = 0$	$x = 10$	$x = 20$	$x = 30$
$x = 40$	$x = 100$	$x = 150$	$x = 190$
$x = 200$	$x = 210$	$x = 220$	$x = 230$
$x = 250$	$x = 300$	$x = 400$	$x = 480$
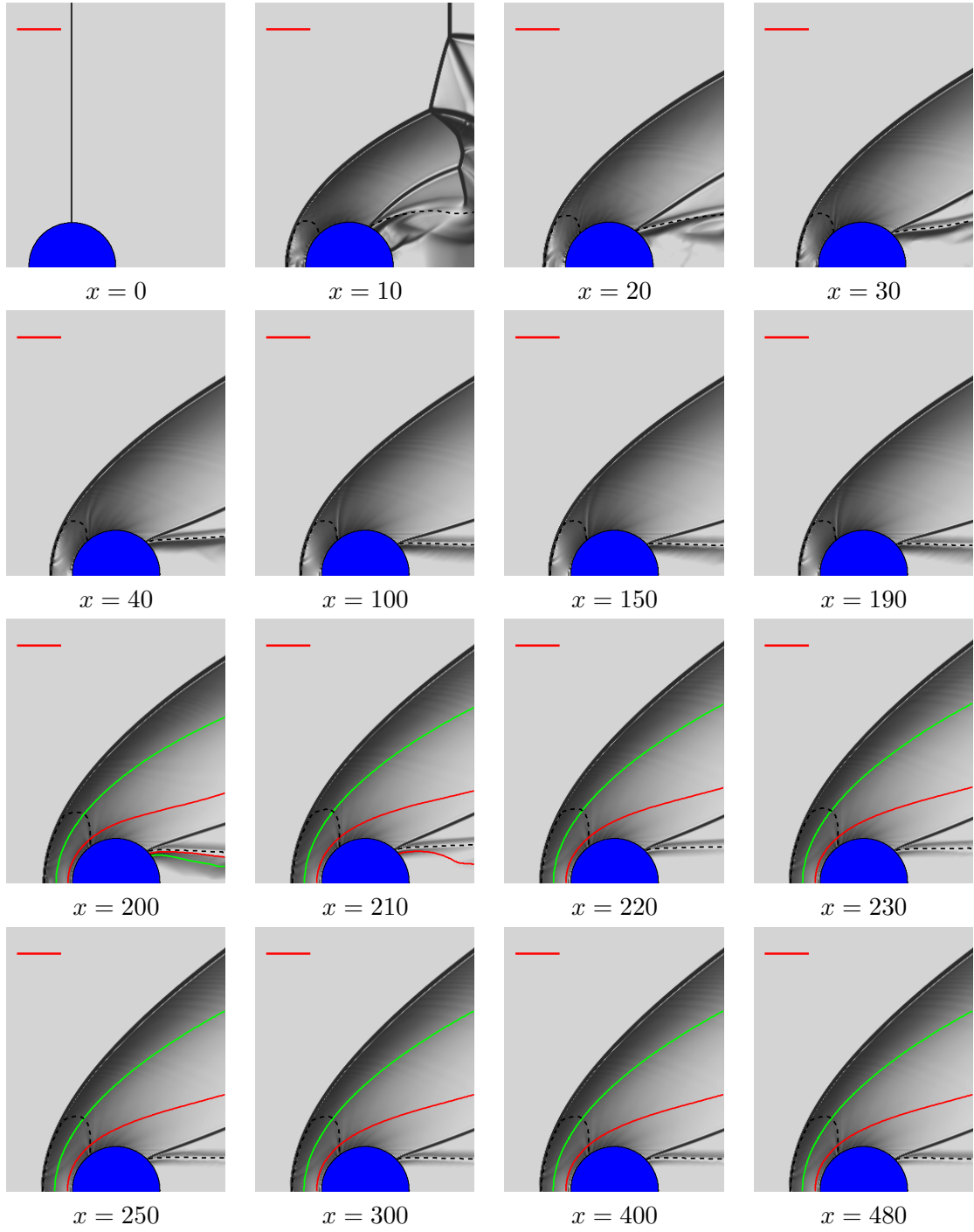
Figure 7.41: Numerical schlieren and reaction contours for case b11sr2, a refined version of case b11 around the projectile, in Table 7.4. The black dashed line is the sonic locus.

$x = 0$　　$x = 20$　　$x = 40$　　$x = 60$

$x = 80$　　$x = 100$　　$x = 200$　　$x = 300$

$x = 320$　　$x = 340$　　$x = 360$　　$x = 380$

$x = 400$　　$x = 600$　　$x = 800$　　$x = 980$
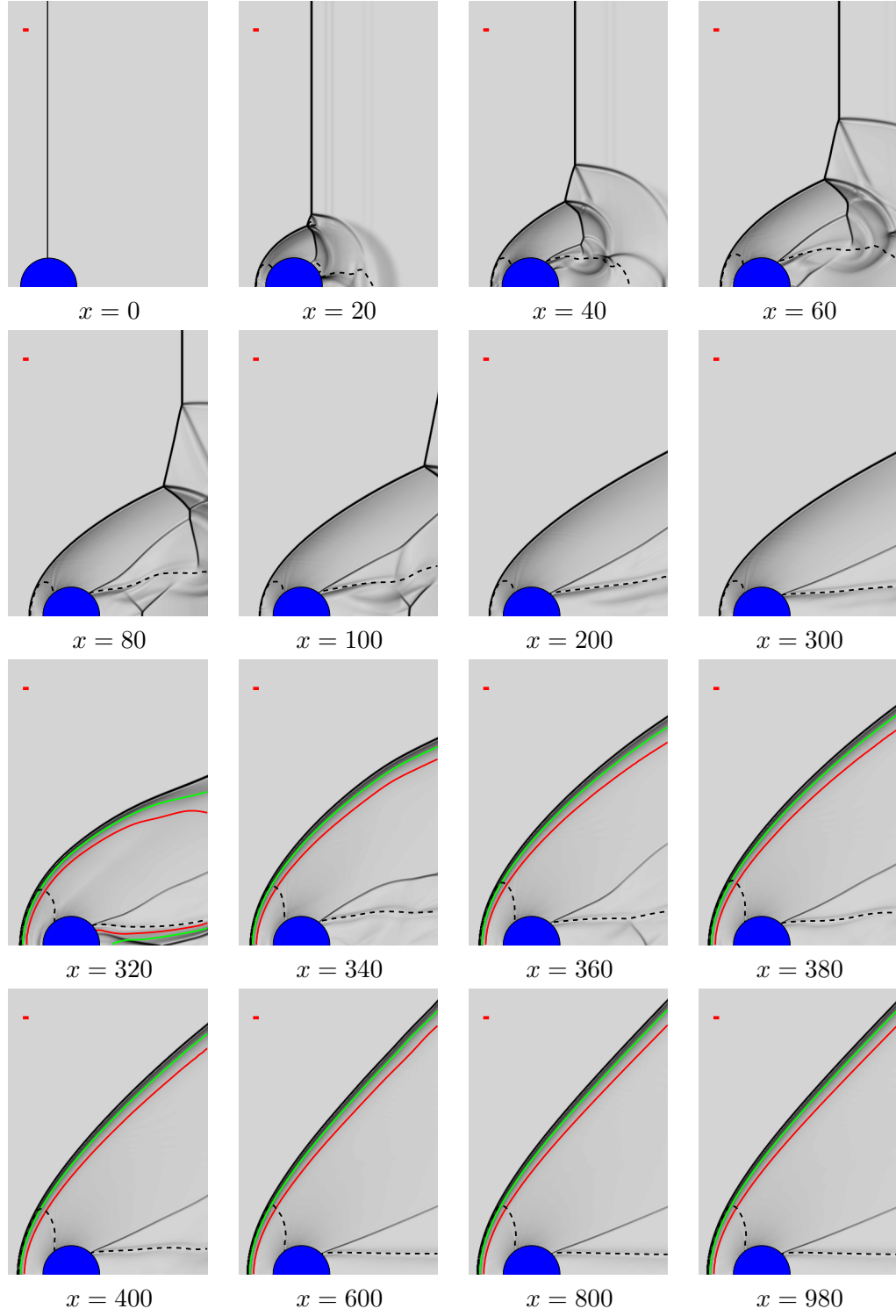
Figure 7.42: Numerical schlieren and reaction contours for case b16 in Table 7.4. The black dashed line is the sonic locus.
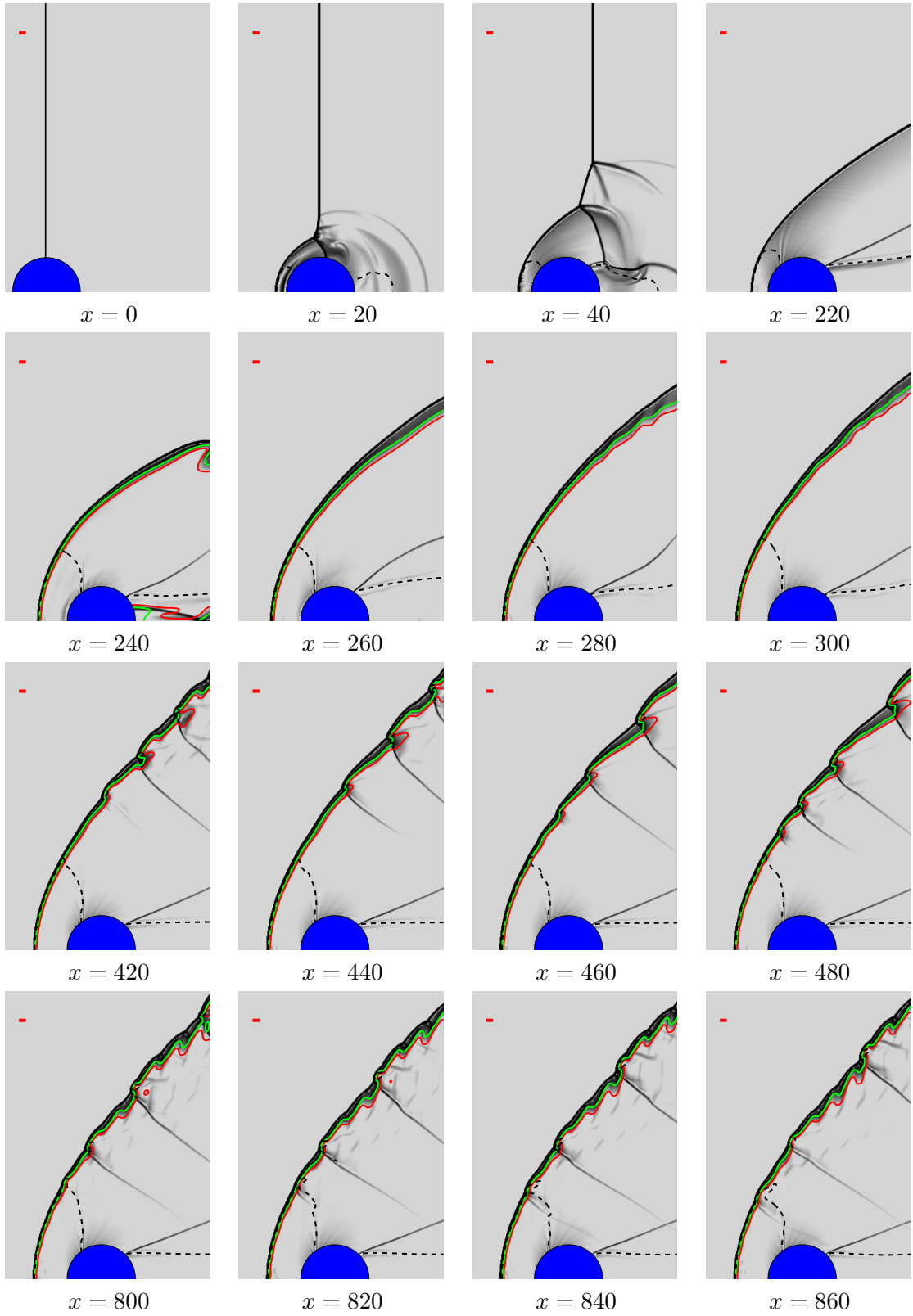
Figure 7.43: Numerical schlieren and reaction contours for case E3 in Table 7.8.

Chapter 8

Conclusion

The new results presented in this thesis are:

- Two new algorithms for computing the dimensionality of ILDMs.

- A description of the consequences of using an ILDM of insufficient dimension for detonation simulations.

- An embarrassingly parallel algorithm for the computation of ILDMs.

- Numerical simulations of projectile-initiated stabilized oblique detonations.

- Verification of the critical decay-rate criterion for projectile-stabilized detonations proposed by Kaneshige (1999), using two-dimensional simulations with one-step irreversible chemistry.

8.1 Summary

Computational Fluid Dynamics simulations of compressible gas dynamical systems are computationally expensive. With the addition of chemistry, such as in the modeling of detonation waves in gaseous explosives, the current state-of-the-art in computational power is still incapable of simulating the reactive Euler equations in three dimensions for even simple (nitrous oxide and air detonation) reaction networks.

In the first part of the thesis, an analysis of the Intrinsic Low Dimensional Manifolds (ILDMs) of Maas and Pope (1992b) for detonation simulations was presented. This technique achieves reduction by algorithmically identifying and decoupling the chemical reactions whose timescales are vastly shorter than the timescales of the fluid mechanics. By

setting these reactions to equilibrium, a low-dimensional submanifold in chemical state-space is obtained, and the computational cost associated with chemistry is reduced by restricting the original chemical kinetics to this submanifold.

One of the major challenges associated with the practical implementation of ILDMs comes from the numerical solution of these submanifolds. An ILDM is defined as a zero-levelset of a composite and highly nonlinear function; conventional numerical procedures for finding zero-levelsets, such as multidimensional continuation schemes, are slow and, more importantly, non-robust. It was shown in this thesis that the ILDM equations can be recast into an embarrassingly parallel algorithm, based on the idea of filling a manifold by trajectories (also called a *congruence*). This solution method is superior for two main reasons: increased speed and increased robustness.

Another important issue is the competition between the demands of computational resources and the demands of the flow physics and reaction chemistry. Practically, the selection of the reduced manifold's dimension is often made because of computational necessity; a high-dimensional (high, in this context, is 3 or above) manifold is hard to compute, even harder to solve, and expensive to interpolate on. On the other hand, no robust techniques previously existed to quantitatively estimate the minimum dimension required.

In this thesis, two new algorithms were presented that allow the issue of the required number of ILDM dimensions to be quantitatively settled. Furthermore, the effect of under-resolving the chemical kinetics (by using an ILDM of insufficient dimension) was elucidated by means of steady-flow solutions and thermodynamic considerations of detonations.

It was concluded that the use of an ILDM in the induction region of a detonation invariably results in a completely unrealistic solution that is unfaithful to the actual ZND structure. A new *Reaction Manifold* technique, similar to the induction manifolds of Eckett (2001), was proposed that systemically reduces a given detailed kinetics mechanism into a progress variable-type model. Unlike the ILDM, this simple reduction is able to (and was designed to) recover the steady-state solution from the full mechanism. Unfortunately, its success also depends on the flow being simple and steady, attributes not enjoyed by many physically interesting flow fields.

In the second part of the thesis, numerical simulations of detonations initiated by hypervelocity projectiles were presented and, through the use of a one-step reaction model, the transition from shock-induced combustion to detonation initiation was observed. The

critical decay-rate model of Kaneshige (1999) was shown to successfully predict this transition.

8.2 Future work

While the prediction of the critical decay-rate model is in agreement with the numerical results, the projectile radius required for the transition to detonation is experimentally observed to be some $15 \sim 50$ times higher than predicted. One of the main explanations for this discrepancy is that a first-order one-step reaction model cannot capture the true reaction kinetics of real detonable mixtures. Furthermore, the projectiles simulated in this work are cylindrical as opposed to spherical, and the effects of transverse waves need to be explored. Numerical simulations using detailed reaction kinetics with sufficient grid-refinement to capture the intricate details of three-dimensional detonation instabilities will be extremely challenging and require substantial advances in computational power and algorithms.

Even limiting the scope to one-step reaction models, much work remains to be done. The simulations presented have explored only a small part of the parameter space. Detailed investigations of the effects of the overdrive f, the heat release q, and the reaction order of the one-step model are needed in order to thoroughly validate the model.

Bibliography

Aivazis, M., B. Goddard, D. Meiron, M. Ortiz, J. C. Pool, and J. Shepherd (2001). ASCI alliance center for simulation of dynamic response in materials FY 2001. Technical report, California Institute of Technology.

Amtec Engineering, Inc. (1998). *Tecplot Version 7.5 User's Manual*. Bellevue, Washington: Amtec Engineering, Inc.

Arienti, M. (2003). *A Numerical and Analytical Study of Detonation Diffraction*. Ph.D. thesis, California Institute of Technology.

Arienti, M., P. Hung, E. Morano, and J. E. Shepherd (2003). A level set approach to Eulerian-Lagrangian coupling. *J. Fluid Mech. 185*, 212–251.

Arienti, M., E. Morano, and J. Shepherd (1999). Nonreactive Euler flows with Mie-Grneisen equation of state for high explosives. Technical Report FM99-8, Graduate Aeronautical Laboratories at California Institute of Technology.

Arnold, V. (1973). *Ordinary Differential Equations*. The MIT Press.

Bell, J. B., N. J. Brown, M. S. Day, M. Frenklach, J. F. Grcar, R. M. Propp, and S. R. Tonse (2000). Scaling and efficiency of prism in adaptive simulations of turbulent premixed flames. In *28th Symp. (Intl) on Combustion*. The Combustion Institute.

Blasenbrey, T., D. Schmidt, and U. Maas (1999). An improved tabulation strategy for reduced chemical kinetics based on ILDM. Unpublished. Paper no. 89 presented at *17th ICDERS*, Heidelberg, Germany.

Callen, H. B. (1985). *Thermodynamics and an introduction to Thermostatistics*. John Wiley & Sons, Inc.

Chakroborty, D., R. Muller, S. Dasgupta, and W. G. III (1999). A detailed model for the decomposition of nitramines: RDX and HMX. Technical Report TR-108, California Institute of Technology.

Chakroborty, D., R. Muller, S. Dasgupta, and W. G. III (2000). The mechanism for unimolecular decomposition of RDX, an ab initio study. *J. Phys. Chem.* A *104*, 2261–2272.

Chakroborty, D., R. Muller, S. Dasgupta, and W. G. III (2001). Mechanism for unimoecular decomposition of HMX (1,3,5,7-tetranitro-1,3,5,7-tetrazocine), an ab initio study. *J. Phys. Chem.* A *105*, 1302–1314.

Cohen, R. E., O. Glseren, and R. J. Hemley (1999). Accuracy of equation-of-state formulations. Technical Report TR-059, California Institute of Technology.

Courant, R. and D. Hilbert (1989). *Methods of Mathematical Physics, Volume I.* John Wiley & Sons, Inc.

Coxeter, H. (1973). *Regular Polytopes.* Dover Publications, Inc.

do Carmo, M. P. (1976). *Differential Geometry of Curves and Surfaces.* Prentice-Hall, Inc.

Eckett, C. (2001). *Numerical and Analytical Studies of the Dynamics of Gaseous Detonations.* Ph.D. thesis, Graduate Aeronautical Laboratories at California Institute of Technology.

Fedkiw, R., T. Aslam, B. Merriman, and S. Osher (1999). A non-oscillatory Eulerian approach to interfaces in multimaterial flows (the ghost fluid method). *J. Comput. Phys. 152*(2), 457–492.

Fickett, W. and W. C. Davis (1979). *Detonation.* University of California Press.

Frankel, T. (1997). *The Geometry of Physics An Introduction.* Cambridge University Press.

Friedman, J. (1991). Multivariate Adaptive Regression Splines. *Annals of Statistics 19(1)*, 1–141.

Golub, G. and C. van Loan (1996). *Matrix Computations.* Johns Hopkins University Press.

Goodwin, D. G. (2003). Cantera user's manual. `http://www.cantera.org/`.

Grismer, M. and J. Powers (1996). Numerical predictions of oblique detonation stability boundaries. *Shock Waves 6*(3), 147–156.

Guillemin, V. and A. Pollack (1974). *Differential Topology.* Prentice-Hall, Inc.

Hairer, E. (1996). *Solving Ordinary Differential Equations II: Stiff and Differential-Algebraic Problems, 2nd Revision Edition.* Springer-Verlag.

Hindmarsh, A. C. (1983). ODEPACK: A systematized collection of ODE solvers. In R. S. Stepleman et al. (Eds.), *Scientific Computing*, pp. 55–64. Amsterdam: North-Holland.

Hirsch, M. W. and S. Smale (1974). *Differential Equations, Dynamical Systems, and Linear Algebra.* Academic Press.

Holmes, M. H. (1995). *Introduction to Perturbation Methods.* Springer-Verlag New York, Inc.

Holmes, P., J. Lumley, and G. Berkooz (1996). *Turbulence, Coherent Structures, Dynamical Systems and Symmetry.* Cambridge University Press.

Horn, R. A. and C. R. Johnson (1985). *Matrix Analysis.* Cambridge University Press.

Ju, Y. and A. Sasoh (1997). Numerical study of detonation initiation by a supersonic sphere. *Transactions of the Japan Society for Aeronautical and space sciences 40*(127), 19–29.

Kaneshige, M. (1999). *Gaseous Detonation Initiation and Stabilization by Hypervelocity Projectiles.* Ph.D. thesis, Graduate Aeronautical Laboratories at California Institute of Technology.

Kaper, H. G. and T. J. Kaper (2002). Asymptotic analysis of two reduction methods for systems of chemical reactions. *Physica D Nonlinear Phenomena 165*, 66–93.

Kasahara, J., T. Arai, S. Chiba, K. Takazawa, Y. Tanahashi, and A. Matsuo (2002). Criticality for stabilized Chapman-Jouguet oblique detonation around sphere bodies in acetylene-oxygen-krypton mixtures. Unpublished. Presented at the *29th International Symposium on Combustion*, Sapporo, Japan, July 21-26.

Kasahara, J., T. Arai, A. Matsuo, and N. Akai (2001). Critical condition for Chapman-Jouguet oblique detonation waves stabilized around hypersonic projectiles. Unpublished.

Presented at the *17th International Colloquim on the Dynamics of Explosions and Reactive Systems*, Seattle, USA. July 29-August 3.

Kasahara, J., T. Fujiwara, T. Endo, and T. Arai (2001). Chapman-Jouguet oblique detonation structure around hypersonic projectiles. *AIAA Journal 39*, 1553–1561.

Kee, R. J., F. M. Rupley, and J. A. Miller (1987). The CHEMKIN thermodynamic data base. Technical Report SAND87-8215, Sandia National Laboratories.

Kee, R. J., F. M. Rupley, and J. A. Miller (1989). CHEMKIN-II: A Fortran chemical kinetics package for the analysis of gas-phase chemical kinetics. Technical Report SAND89-8009, Sandia National Laboratories.

Lam, S. H. (1993). Using CSP to understand complex chemical kinetics. *Combust. Sci. Technol. 89*, 375–404.

Liepmann, H. and A. Roshko (2001). *Elements of Gasdynamics.* Dover Publications, Inc.

Maas, U. (1998). Efficient calculation of intrinsic low-dimensional manifolds for the simplification of chemical kinetics. *Comput. Visual. Sci. 1*, 69–81.

Maas, U. and S. B. Pope (1992a). Implementation of simplified chemical kinetics based on intrinsic low–dimensional manifolds. In *24th Symp. (Intl) on Combustion*, pp. 103–112. The Combustion Institute.

Maas, U. and S. B. Pope (1992b). Simplifying chemical kinetics: Intrinsic low-dimensional manifolds in composition space. *Combust. Flame 88*, 239–264.

Maas, U. and J. Warnatz (1988). Ignition proceses in hydrogen–oxygen mixtures. *Combust. Flame 74*, 53–69.

Mason, S. D., C. A. Kennedy, and J. C. Sutherland (2002). Error control techniques for explicit time integration of the compressible Navier-Stokes equations in the presence of moderately stiff chemistry. Unpublished. Presented at the *9th International Conference on Numerical Combustion*, Sorrento, Italy.

Matsuo, A. and T. Fujiwara (1993). Numerical investigation of standing oblique detonation supported by 2-dimensional blunted wedge. *Transactions of the Japan Society for Aeronautical and space sciences 36*(111), 47–56.

Meiron, D. I. (1999). Proposal to the asci academic strategic alliances program. `http://www.cacr.caltech.edu/ASAP/mission/ASCI.proposal.pdf`.

Miller, J. A. and C. T. Bowman (1989). Mechanism and modeling of nitrogen chemistry in combustion. *Prog. Energy Combust. Sci. 15*, 287–338.

Nafe, J. and U. Maas (2002). A general algorithm for improving ILDMs. *Combust. Theor. Model. 6*, 697–709.

Niemann, H., D. Schmidt, and U. Maas (1997). An efficient storage scheme for reduced chemical kinetics based on orthogonal polynomials. *J. Eng. Math. 31*, 131–142.

Oran, E. S., J. W. Weber, Jr., E. I. Stefaniw, M. H. Lefebvre, and J. D. Anderson, Jr. (1998). A numerical study of a two-dimensional H_2–O_2–Ar detonation using a detailed chemical reaction model. *Combust. Flame 113*, 147–163.

Paolucci, S., J. M. Powers, and S. Singh (2000). Application of intrinsic low dimensional manifolds to nitramine combustion. Unpublished. Presented at *8th Int. Conf. Numer. Combust.*, Amelia Island, Florida.

Papalexandris, M. V. (2000). A numerical study of wedge-induced detonations. *Combust. Flame 120*(4), 526–538.

Pintgen, F., J. Austin, and J. Shepherd (2002). Detonation front structure: Variety and characterization. International Colloquium on Advances in Confined Detonations, Moscow, Russia, July 2-5, 2002.

Pope, S. (1997). Computationally efficient implementation of combustion chemistry using in situ adaptive tabulation. *Combust. Theor. Model. 1*, 41–63.

Pratt, D., J. Humphrey, and D. Glenn (1991). Morphology of standing oblique detonation-waves. *Journal of Propulsion and Power 7*(5), 837–845.

Quirk, J. J. (1994). Godunov-type schemes applied to detonation flows. In J. Buckmaster et al. (Eds.), *Combustion in High-Speed Flows*, pp. 575–596. Kluwer Academic Publishers.

Rastigejev, Y., S. Singh, C. Bowman, S. Paolucci, and J. Powers (2000, January). Novel modelling of hydrogen/oxygen detonation. In *38th AIAA Aerospace Sciences Meeting and Exhibit*, Volume AIAA-2000-0318, Reno, Nevada.

Rhodes, C., M. Morari, and S. Wiggins (1999). Identification of low order manifolds: Validating the algorithm of Maas and Pope. *CHAOS 9*(1), 108–123.

Schultz, E. (2000). *Detonation Diffraction through an abrupt area expansion*. Ph.D. thesis, California Institute of Technology.

Schutz, B. (1980). *Geometrical methods of mathematical physics*. Cambridge University Press.

Sell, G. R. and Y. You (2002). *Dynamics of Evolutionary Equations*. Springer-Verlag New York Inc.

Shampine, L. F. and H. A. Watts (1979). DEPAC – Design of a user oriented package of ODE solvers. Technical Report SAND79-2374, Sandia National Laboratories.

Shepherd, J., F. Pintgen, J. Austin, and C. Eckett (2002). The structure of detonation front in gases. 30th AIAA Aerospace Sciences Meeting and Exhibit, January 14-17, 2002, Reno NV, AIAA 2002-0883.

Shepherd, J. E. (1986). Chemical kinetics of hydrogen–air–diluent detonations. *Prog. Astronaut. Aeronaut. 106*, 263–293.

Shepherd, J. E. (1994). Detonation waves and propulsion. In J. D. Buckmaster, T. L. Jackson, and A. Kumar (Eds.), *Combustion in High-Speed Flows*, pp. 373–420. Dordrecht: Kluwer Academic Publishers.

Singh, S. (2003). *Rational reduction of reactive flow models and efficient computation of their solutions*. Ph.D. thesis, University of Notre Dame.

Singh, S. and J. M. Powers (1999). Modeling gas phase RDX combustion with intrinsic low dimensional manifolds. Unpublished. Paper no. 82 presented at *17th ICDERS*, Heidelberg, Germany.

Singh, S., Y. Rastigejev, S. Paolucci, and J. Powers (2001a). Viscous detonation in H2/O2/Ar using intrinsic low dimensional manifolds and wavelet adaptive multilevel representation. *Combust. Theor. Model. 5*, 163–184.

Singh, S., Y. Rastigejev, S. Paolucci, and J. M. Powers (2001b). Viscous detonation in H_2-O_2-Ar using intrinsic low-dimensional manifolds and wavelet adaptive multilevel representation. *Combust. Theory Modelling 5*, 163–184.

Smith, G. P., D. M. Golden, M. Frenklach, N. W. Moriarty, B. Eiteneer, M. Goldenberg, C. T. Bowman, R. K. Hanson, S. Song, J. Willam C. Gardiner, V. V. Lissianski, and Z. Qin (2003). Gri-mech 3.0. `http://www.me.berkeley.edu/gri_mech/`.

Spivak, M. (1965). *Calculus on Manifolds.* Addison-Wesley.

Strang, G. (1968). On the construction and comparison of difference schemes. *SIAM J. Numer. Anal. 5*, 506–517.

van Oijen, J. and L. de Goey (2000). Modelling of premixed laminar flames using flamelet-generated manifolds. *Comb. Sci. Tech. 161*, 112–137.

Warnatz, J., U. Maas, and R. Dibble (1999). *Combustion. Physical and Chemical Fundamentals, Modeling and Simulation, Experiments, Pollutant Formation, Second Edition.* Springer–Verlag.

Williams, F. A. (1985). *Combustion Theory. The fundamental theory of chemically reactive flow systems. 2nd Edition.* Addison-Wesley Publishing Company.

Index